

## ABSTRACT

FORD, KRISTOPHER AUSTIN. Pulsing Plasmas to Expand the Diagnostic Capabilities of Microwave Probes and Optical Emission Spectroscopy. (Under the direction of Steven Shannon.)

Low temperature plasmas are a highly dynamic system, filled with feedback loops and strongly correlated parameters. In the development of diagnostics to study these systems, the experimentalist is often required to make assumptions about information unavailable to the diagnostic, yet necessary for the analysis of the diagnostic data. In the ongoing development of low temperature plasma processing for the semiconductor industry, the demands on diagnostics have only risen, and researchers are required to re-evaluate the previous assumptions for further improvement. This work leverages the dynamic behavior of pulsed plasmas to address the assumptions contributing to the uncertainty of two diagnostics: microwave hairpin probes which measure electron density and pulse induced fluorescence which measures the surface loss probability of free radicals. Pulsed plasmas allow for the simplified study of plasma parameters, particularly in the afterglow when the complex production of excited species has ceased. This is the fulcrum that underlies pulsed plasmas as diagnostics, or PPDs, for improving diagnostic accuracy.

In the opening chapter, pulsed plasma dynamics are discussed in order to provide the reader with an understanding of the wide range of time scales relevant to pulsed plasmas. For example, the decay constant may be as little as a few ns for spontaneous emission coefficients, or many ms for long lived free radicals. A review of other PPDs is provided as well, followed by an introduction to hairpin probes and pulse induced fluorescence as they are traditionally used. The latter case was already classified as a PPD, but had previously required the assumption of gas temperature to analyze the data. This greatly contributes to the uncertainty of the measured surface loss coefficient. The deficiency is addressed through time-resolved spectroscopy of N<sub>2</sub> rotational temperature, which is carried out in a PPD pulsing scheme in Chapter 3. The uncertainty contributions to rotational temperature are rigorously explained; it defeats the purpose if one were to use a more error prone secondary diagnostic to address the uncertainty of the first. The temperature correction is applied to

the pulse induced fluorescence of atomic oxygen, which provides surface loss probability on a quartz surface facing the plasma. The resulting coefficient was  $0.39 \pm 0.07$ , which is significantly higher than any of the previous literature for similar oxygen/glass combinations. The result is explained with regards to plasma activation of the quartz surface; ion bombardment may lead to increased active site turnover and enhanced oxygen-oxygen recombination. The merits of the improved technique are discussed in Chapter 4.

For the hairpin probe diagnostic, there was concern in the plasma community over the extent of electron density perturbation introduced by the probe itself. The probe can not measure the electron temperature and potential drop from the plasma to the probe surface, both of which contribute to the plasma sheath that reduces measured probe density below an unknown, bulk plasma density. This work demonstrates that by pulsing the plasma, the perturbation around the probe is removed in the immediate afterglow. The sheath collapse leads to a rise in measured electron density on the order of a few  $\mu\text{s}$ , which is significantly faster than the following density decay in the rest of the afterglow. It was concluded that the peak density, termed the hairpin spike, provides a more accurate measurement of the electron density than the steady state diagnostic. It bypasses the need for estimating sheath size from theory, which is an ongoing debate in the plasma research community. However, the results lie well within the bounds predicted by the model underlying the most recent sheath correction factor in the literature.

In the final chapter, a summary of the results points the way to future work. The hairpin spike provides new probe design considerations, and an experimental means of verifying their applicable range. The spike technique developed here was mainly concerned with the overall magnitude of the density peak, but the shape of the afterglow density trace may provide new insights into plasma potential as well. For pulse induced fluorescence, continuing study is recommended to bridge the gap between this low pressure work and the moderate pressures researched by others for atomic oxygen on glass. The gas temperature measurement may be improved through spectrometer considerations. A wider spectral range would permit the removal of trace nitrogen addition in favor of measuring the rotational temperature of molecular oxygen directly.

© Copyright 2020 by Kristopher Austin Ford

All Rights Reserved

Pulsing Plasmas to Expand the Diagnostic Capabilities of Microwave Probes and Optical Emission Spectroscopy

by  
Kristopher Austin Ford

A dissertation submitted to the Graduate Faculty of  
North Carolina State University  
in partial fulfillment of the  
requirements for the Degree of  
Doctor of Philosophy

Nuclear Engineering

Raleigh, North Carolina

2020

APPROVED BY:

---

Katharina Stapelmann

---

Mohamed Bourham

---

Steven Shannon  
Chair of Advisory Committee

## **DEDICATION**

Dedicated to my parents, who encouraged me to pursue my scientific interests from an early age, and didn't get too upset when I abandoned one hobby for another.

## **BIOGRAPHY**

Kris Ford was born in Houston, Texas on May 19, 1991 to Karl and Emma Ford. He attended the University of Arizona for their chemical engineering program, graduating in 2013 and continuing with an accelerated MS in May 2014. He began his studies at North Carolina State University in the fall of 2014. Following graduation, he will begin an analytical chemistry business in Oregon together with his brother, Ricky Ford.

## **ACKNOWLEDGEMENTS**

I want to thank Dustin Roberts for making awesome hairpin probes, and taking boba tea as payment. I also appreciate the help that Ervin Miller was always willing to provide, particularly in the early days when I was setting up my experiment and still didn't know how to solder. I also couldn't have made it this far without the collaboration and camaraderie of Dave Peterson. You're up next man, better late than never. As always. I owe a wealth of gratitude to Steve Shannon, for I've been incredibly lucky to call him my mentor and friend. Few grad students have an advisor who takes an interest in their nontechnical development as he does, and I'll take that attitude forward in my next adventure.

## TABLE OF CONTENTS

<b>LIST OF TABLES . . . . .</b>	<b>vi</b>
<b>LIST OF FIGURES . . . . .</b>	<b>vii</b>
<b>Chapter 1 INTRODUCTION . . . . .</b>	<b>1</b>
1.1 Overview of Pulsed Plasmas . . . . .	1
1.2 Dynamics of Pulsed Plasmas . . . . .	5
1.3 Pulsed Plasmas as Diagnostics . . . . .	13
1.4 Pulse Induced Fluorescence . . . . .	19
1.5 Gas Temperature Measurements . . . . .	26
1.5.1 Survey of Gas Temperature Techniques . . . . .	26
1.5.2 Rotational Spectra Theory . . . . .	29
1.6 Hairpin Probes . . . . .	36
<b>Chapter 2 Hairpin Probe Measurements in Transient Plasma Conditions . . . . .</b>	<b>40</b>
2.1 Hairpin Probe Challenges . . . . .	40
2.2 Hairpin Probe Experiment . . . . .	46
2.3 Results and Discussion . . . . .	51
<b>Chapter 3 Time Resolved Rotational Temperature Measurements . . . . .</b>	<b>57</b>
3.1 Rotational Temperature Simulation . . . . .	58
3.2 Time Resolved Temperature Results . . . . .	62
<b>Chapter 4 Pulse Induced Fluorescence with Simultaneous Gas Temperature Measurements . . . . .</b>	<b>71</b>
4.1 PIF Challenges . . . . .	72
4.2 PIF Experiment . . . . .	76
4.3 PIF Results and Discussion . . . . .	80
<b>Chapter 5 Conclusions and Future Work . . . . .</b>	<b>87</b>
5.1 Work to Date . . . . .	87
5.2 Future Work . . . . .	89
<b>BIBLIOGRAPHY . . . . .</b>	<b>94</b>
<b>APPENDICES . . . . .</b>	<b>101</b>
Appendix A      Rotational Temperature Simulation . . . . .	102
Appendix B      Time Resolved Hairpin Probe Analysis . . . . .	114

## **LIST OF TABLES**

Table 1.1	General Guideline of Time Constants in Pulsed Plasmas. . . . .	13
Table 3.1	Rovibrational constants for the second positive N <sub>2</sub> system. . . . .	60
Table 4.1	Literature Surface Loss Values . . . . .	85

## LIST OF FIGURES

Figure 1.1	a) Fully modulated pulsed power scheme. The square pulses represent 13.56 MHz waveforms. b) Partially modulated pulsing scheme with same frequency, duty conditions. Duty cycle and frequency variations on a) are respectively shown in c) and d) figures. . . . .	3
Figure 1.2	Fully modulated power scheme with a) delivered power mode and b) forward power mode. The matching network is fixed in time, but optimized for minimal reflected power in the end of a pulse. . . . .	4
Figure 1.3	Feature notching in polysilicon. a) $\text{Cl}_2$ electron cyclotron resonance plasma at 10 mTorr and b) Monte Carlo simulation of 20 eV ions. [42] . . . . .	7
Figure 1.4	Simulated etch of $\text{Cl}_2$ plasma over Si wafer. On top, the time-dependent neutral flux in pulsing mode $\Gamma_n$ is compared to CW mode $\Gamma_{nc}$ . On bottom, the ratio of ion flux in pulsing mode $\Gamma_i$ to CW mode $\Gamma_{ic}$ shows modulation in time. Pulse frequency was 10 kHz Reduced from original figure in the text. [63] . . . . .	8
Figure 1.5	Planar LP measurements of $T_e$ and plasma density in 5 mTorr Ar. The stovetop ICP was pulsed at 30% duty cycle for a) 1 kHz and b) 10 kHz [20] . . . . .	9
Figure 1.6	LP measurements of off cycle in coil ICP pulsed at 5 kHz and 50% duty. Conditions were 6 mTorr for Ar, 8 mTorr for $\text{Cl}_2$ [1] . . . . .	10
Figure 1.7	a) Microwave interferometry measurement of line averaged $n_e$ at 1 Torr and 75 V in the GEC Reference Cell [31]. b) Model and experimental measurement of afterglow $n_e$ production in $\text{O}_2$ CCP [51]. . . . .	11
Figure 1.8	Radical and feed gas dynamics measured through mass spectroscopy and VUV absorption spectroscopy, respectively. Chamber was a planar coil ICP operating at 20 mTorr with 800 W pulsed at 15 Hz and 15% duty cycle. The gray is the power on period, and the fit arose from a Cl loss balance [6] . . . . .	12
Figure 1.9	OES data taken from the active $\text{SiF}_4$ discharge (bottom curve), etching of Si wafer from a remote $\text{F}_2$ plasma (middle curve), and downstream emission away from the $\text{SiF}_4$ source (top curve). Intensities are not scaled to each other [21]. . . . .	15
Figure 1.10	Bode plots with pendulum analogs. Pendulum inset for the relevant transfer function model is not original to text. Yellow represents information available to experimentors, blue an unknown. a)Bode plot of single step formation of $\text{CF}_2$ from electron impact on $\text{CF}_4$ . Solid line represents the transfer function model, points represent experimental data. b) Bode plot of modified transfer function, which considers an unknown intermediary reaction. Conditions are a CCP with 95/5% $\text{CF}_4$ /Ar feed gas at 500 mTorr and $0.81 \text{ W/cm}^{-3}$ power density [43]. . . . .	16
Figure 1.11	a) LED absorption setup. Chamber dimensions are $r = 27 \text{ cm}$ , $h = 17 \text{ cm}$ . b) LED absorbance of $\text{BCl}$ in the plasma afterglow. Power was pulsed at 150 Hz and 2% duty cycle in an ICP. Gas composition was varied as overall pressure was held at 5 mTorr [87]. . . . .	18

Figure 1.12	Top (a) and side (b) views of remote beam experiment for determining radical recombination coefficients. The Quadrupole Mass Spectrometer was differentially pumped, and the substrate temperature was fixed by a heating element or cooling channel [46] . . . . .	20
Figure 1.13	Hybrid Plasma Equipment Model simulation of semiconductor processing planar ICP. Plasma was pure O <sub>2</sub> at 500 W and 10 mTorr [26]. . . . .	21
Figure 1.14	a) Idealized representation of atomic oxygen density (red) in the afterglow of the RF pulse (blue) b) Probing pulse scheme to obtain snapshot in decay density. c) Fixed pulse scheme to determine [O] decay. . . . .	22
Figure 1.15	LIF (+) comparison with actinometered PIF (o) of CF <sub>2</sub> for two pressures. The relative concentration is based on signal of the main pulse [35]. . . . .	22
Figure 1.16	a) F/Ar actinometry signal for PIF in CF <sub>4</sub> plasma with 5% Ar. b) Decay curves for PIF of CF <sub>4</sub> /Ar plasma in the presence ( $\Delta$ ) and absence ( $\square$ ) of a Si wafer. CF <sub>4</sub> with 10% O <sub>2</sub> and 5% Ar is plotted in (+) and (o) for the presence and absence of Si, respectively [35]. . . . .	23
Figure 1.17	a) PIF probing pulse configuration with raw oxygen emission of the 844 nm line. b) comparison of resulting decay curves for 844 and 777 nm. [14] . . . . .	24
Figure 1.18	H decay results with (black squares) and without (red circles) Ar actinometry. The inset shows two data points for main pulses lasting 100 ms long (blue triangles) rather than 20 ms [19]. . . . .	25
Figure 1.19	Flowchart for rotational equilibrium with translational temperature for the second positive N <sub>2</sub> system. $\tau(C)_{R-T}$ and $\tau(C)$ represent the inverse of collision frequency and Einstein coefficient, respectively [89] . . . . .	28
Figure 1.20	Rigid rotor configuration. Bond length is fixed at $r_o$ and $m_1 > m_2$ . Molecule is allowed to rotate in two directions. The $\theta$ direction, in and out of the page, is not shown. . . . .	30
Figure 1.21	Rotating molecule with identical nuclei (orange) moving in and out of the page as they precess around the constant resulting vector, $\vec{J}$ . The electron cloud in blue is rotating to give a net angular momentum $\Lambda$ . The bold and dotted vectors on the right represent directions out of and into the page, respectively. . . . .	33
Figure 1.22	a) Molecular motion in Hund's case <i>a</i> , when electron spin couples strongly to the internuclear axis. b) Motion in Hund's case <i>b</i> , when spin is not coupled to the axis. In both cases, the molecule precesses about the total angular momentum vector $\vec{J}$ , which is fixed. . . . .	34
Figure 1.23	Representation of the HP immersed in a plasma. Sheath formation around the tines will alter their antenna response, as the localized volume contains varying two dielectric materials, the vacuum and the plasma. . . . .	37
Figure 2.1	HP within plasma. Inset shows cylindrical sheath between tines with sheath model dimensions. . . . .	41
Figure 2.2	Electric field magnitude in radial plane of HP (V/m). Simulated HP dimensions are $a=0.065$ mm, $w=3$ mm and $l=17$ mm [90]. . . . .	43

Figure 2.3	HP resonant frequency (diamonds) and probe current (triangles) versus DC bias. $f_o=3.115$ GHz and $V_{in}$ represents the 80 MHz drive voltage of the Ar CCP [70]. . . . .	44
Figure 2.4	HP relative uncertainty for a range of $n_e$ . Calculation used HP characteristics $f_o=2.73$ GHz and $w=3.85$ mm. For varying $k$ (red) the temperature was fixed at 4 eV, and for varying $T_e$ (black), $k=2$ . . . . .	45
Figure 2.5	Time resolved HP experiment in an ICP with integrated matching network. Dashed lines represent communications and data signals. The HP antenna was centered both radially and axially. . . . .	47
Figure 2.6	a) HP configuration and b) example vacuum, plasma frequency response. . . . .	48
Figure 2.7	Time resolved HP Configuration. Black arrows represent drive signal, dashed red arrows the reflected measurement signal. Filters were added to reduce stray 13.56MHz noise from the RF generator powering the plasma. . . . .	49
Figure 2.8	Voltage trace in time and HP frequency. Blue reflects $f_r$ . The oscilloscope was triggered off of the forward power, which provided more stability than the external trigger. The surface shown would translate into a $n_e(t)$ trace that is initially flat, then begins to decrease at approximately 110 $\mu$ s. . . . .	50
Figure 2.9	Raw and Lorentz-fitted data for one complete pulsed. Power was delivered in 20 W, 1 kHz pulses at 50% duty cycle in Argon. . . . .	50
Figure 2.10	Hairpin spike of 10W pulsed at 500 Hz, 80% duty cycle. Power shuts off at 10 $\mu$ s. Black data points are for the HP measurement, and the blue projection is an exponential fit of the HS maximum, onward. . . . .	52
Figure 2.11	a) VI probe (blue) and HS trace (black) for 10 W pulsed at 1 kHz and 80% duty cycle in a 20 mTorr Ar discharge. b) Same plasma conditions compared to a He discharge, for which the power was increased to 16 W to sustain a similar steady state $n_e$ [25]. . . . .	53
Figure 2.12	Number of Debye lengths necessary to correct $n_{e,ss}$ up to the HS density for two HP widths. Plasma conditions: 10 mTorr Ar, 3 sccm. Power pulsed at 500 Hz and 80% duty cycle [25]. . . . .	54
Figure 2.13	Plasma potential acquired from LP under constant power conditions in 10 mTorr Ar [25]. . . . .	55
Figure 2.14	Sheath size calculated from $k\lambda_D$ for the HP, and from the Matrix model for the LP data [25]. . . . .	55
Figure 3.1	a) $S_{J',J''}$ values for Hund's intermediate case formulation. b) Relative difference in line strengths between intermediate and Hund's case $a$ simulations. c) Intensity distribution with 'infinite resolution' for line strengths from Hund's intermediate case and example $T_r$ of 450 K. . . . .	61
Figure 3.2	Simulation comparison with experiment for pure nitrogen. Conditions were 100 W and 50 mTorr. Best fit obtained for $T_r=445K \pm 14K$ . . . . .	62
Figure 3.3	Experiment for determining $T_r(t)$ in ICAROS. N <sub>2</sub> was added as 5% of total gas composition for O <sub>2</sub> /N <sub>2</sub> pulsing experiments. Plasma conditions were 50 mTorr and 200 W, with on cycle periods lasting for 1 or 10 ms. . . . .	63

Figure 3.4	Two single pulse acquisitions for a 50 mTorr N <sub>2</sub> /O <sub>2</sub> mixture pulsed at 20 Hz and 200 W. Gain was 3200, and the data represents the [400,600] $\mu$ s window after power on. . . . .	64
Figure 3.5	a) Experimental relative error as a function of wavelength for the spectrum shown in b). Data set was obtained for 10 ms into the on cycle of a 200 W, 50 mTorr pulse with 5% N <sub>2</sub> . . . . .	65
Figure 3.6	Procedure for analyzing Echelle data. Diagram illustrates the analysis of one time point and the quantification of the relative errors (red) at each step. . . . .	66
Figure 3.7	a) $\chi^2$ minimization that converged at two example temperatures. b) Optimal bootstrap temperature results for ten iterations. The colored points correspond to the $\chi^2$ examples shown. Example data taken from the first time point of the 10 ms pulse in a 200 W ICP. . . . .	67
Figure 3.8	a) $T_r$ results with overall error included, taking into account simulation and experimental contributions. b) Example average spectra, with reference subtracted, from three selected timesteps that correspond to the data on the left. . . . .	68
Figure 3.9	a) Probing pulse scheme. Blue shows the voltage trigger, and was set to different levels to activate the spectrometer only while the generator always triggered. b) Rising saturation fit (red) and $T_r(t)$ data for the main pulse. . . . .	69
Figure 3.10	a) Probing pulse $T_r(t)$ data. Error bars not shown for clarity. Legend indicates time between the end of the main pulse and the start of the trigger for the probing pulse. b) Unique projection results for the probing pulse data shown on the left. . . . .	69
Figure 3.11	a) Separate projections for the main pulse (red) and the starting point of each probing pulse (blue). b) Resulting transferred projections for selected probing pulse on-cycles. . . . .	70
Figure 4.1	Radical to ion flux ratio at the wafer surface of a planar ICP. The Hybrid Plasma Equipment Model simulated a 500 W and 10 mTorr O <sub>2</sub> plasma [26]. . . . .	72
Figure 4.2	a) Eley-Rideal reaction of gaseous atom (blue) with chemisorbed atom (orange). b) Langmuir-Hinshelwood reaction of chemisorbed and physisorbed (green) atoms. Red arrows represent atom motion. . . . .	73
Figure 4.3	a) Idealized representation of atomic oxygen density (red) in the afterglow of the RF pulse (blue). b) Probing pulse scheme to obtain snapshot in decay density. c) Fixed pulse scheme to determine [O] decay. . . . .	74
Figure 4.4	PIF results for varied $T_g$ assumptions. Error bars are determined by one standard deviation from the goodness of exponential fit. Conditions were 20 mTorr, 50 W power and pure O <sub>2</sub> plasma. . . . .	75
Figure 4.5	Gas temperature from OES data and spectral fit of N <sub>2</sub> rotational temperature (points). An exponential fit was applied, shown as a solid line. Experiment was 320 W planar ICP with O <sub>2</sub> /Cl <sub>2</sub> gas mixture [56]. . . . .	75

Figure 4.6	PIF diagnostic setup on the ICAROS plasma source. An optical fiber delivers rovibrational spectra into the Echelle spectrometer. External pulse generation, in blue, provides the unique signals to the RF generator and diagnostic equipment (green). Inset graphs show idealized [O] traces in red together with the unique trigger signals in blue. . . . .	77
Figure 4.7	a) Example iCCD output for one pixel. The main pulse begins at 0 ms, and the probing pulse at 10.5 ms for a time off data point of $t = 500\mu\text{s}$ . b) Raw iCCD image at $100\ \mu\text{s}$ into the probing pulse. . . . .	78
Figure 4.8	Flow chart depicting Matlab data analysis algorithm. Probing pulses were also $T_r(t)$ corrected. . . . .	79
Figure 4.9	Example iCCD output for one pixel (black) compared to the temperature corrected result (red) for the main pulse in a) and the probing pulse in b) which has a $500\ \mu\text{s}$ delay following the end of the main pulse. All values have been normalized to their relative maxima. . . . .	80
Figure 4.10	Example iCCD output for one pixel with temperature correction (black). Exponential rise models were fit to accurately determine $I(t = 0)$ , shown in red. b) provides the same figure but zoomed in for clarity. . . . .	81
Figure 4.11	a) Temperature curves for main pulse and probing pulse in the afterglow. b) Exponential fit (green) and final data (black) for the temperature corrected PIF. The outermost annular ring is shown, representing a disk extending 1 cm inwards from the quartz edge. . . . .	82
Figure 4.12	Exponential fit (lines) and final data (black) for the temperature corrected PIF. The outermost annular ring is shown, representing a disk extending 1 cm inwards from the quartz edge. A starting value of 1 was used for the $k_1$ fit, as the original fitting model provides separated coefficients. . . . .	83
Figure 4.13	Surface loss coefficient results from $k_1$ (black) and $k_2$ (green). The $R = 0\ \text{cm}$ point represents the center of the discharge, and $R = 5$ the plasma edge. Error bars were determined from the goodness of fit for $\beta_1$ , and an estimated RSD of 20% for the secondary $\beta_2$ . . . . .	84
Figure 5.1	Number of Debye lengths used to correct $n_{e,ss}$ up to the HS density for two grounded HPs and one floating HP. Plasma conditions: 10 mTorr Ar, 3 sccm. Power pulsed at 500 Hz and 80% duty cycle. . . . .	89
Figure 5.2	a) HS of a 3.35 mm floating probe (red) and 4.05 mm grounded probe (black) at 10 W, 10 mTorr Ar pulsed with 500 Hz and 80% duty cycle. Error limits are shown as dashed ranges. b) 20 mTorr, 1 kHz pulsing plasma conditions compared between an Ar and He discharge. The power was increased from 10 to 16 W to sustain a similar steady state $n_e$ in the latter case [25]. . . . .	90
Figure 5.3	Hybrid plasma equipment model of ICAROS experiment under steady state conditions: 200 W, 50 mTorr of O <sub>2</sub> with 10 sccm. Radius of zero refers to plasma center. . . . .	92

## CHAPTER

# 1

## INTRODUCTION

### 1.1 Overview of Pulsed Plasmas

In plasmas driven by constant power, the common control variables available to the plasma engineer are RF power, RF frequency, gas composition, pressure, and chamber material. These knobs will influence the plasma electron density, temperature, ion energy, ion flux, and reactive chemistry in such a way that a unique steady state balance is met. However, the modulation of power in pulsed plasmas allows for the expansion of this parameter space. For example, an inductively coupled plasma, or ICP, will typically have steady state electron temperatures in the range of 2-5 eV for low pressure Ar [27, 60, 93]. Power pulsing, on the other hand, can generate a temperature overshoot of as much as 50% over the steady state value at the beginning of the on cycle [23, 72]. The overshoot results from the electron loss in the off cycle, or plasma afterglow. When the generator initiates power again, the power coupling is split between fewer electrons. The elevated electron temperature will drive

further ionization and stabilize within tens of microseconds as a growing electron population divides the coupled power. However, during that overshoot there will be conditions that are inaccessible to CW plasmas. Similarly, electron temperatures can be reached in the afterglow (after power shutoff) that are fractions of an eV. The low electron temperature creates a quiescent plasma that can not be reached with steady state power delivery.

It is this widened parameter space that has attracted the interest of the low temperature plasma community in recent years [3, 4, 23]. Power modulation presents many new control variables to manipulate: power ramping, pulse frequency, duty cycle, and modulation extent. In power ramping, a gradual shift is made between forward power levels. Pulse frequency is the number of cycles per second that the power scheme repeats, in units of Hz, and duty cycle is the ratio of time between the on cycle ( $P_{on}$ ) and low power ( $P_{off}$  or  $P_{low}$ ). Figures 1.1a and 1.1b illustrate the comparison between fully and partially modulated power delivery schemes, respectively. The generator used here is able to ramp up to and down from full power within 10  $\mu$ s, therefore the pulse trains are represented as square waves although this particular generator delivers 13.56 MHz.

The possible parameter space is further expanded when two power supplies are used; a common design is the planar coil ICP with cathode bias [3, 4, 85]. This work will restrict itself to the study of a cylindrical coil ICP with a single power supply and full power modulation. Power, duty cycle, and pulsing frequency are the variables that are manipulated to control a fully modulated pulsing scheme. For full modulation, duty cycle is equal to the ratio of  $t_{on}$  to  $t_{off}$ . The increase of duty cycle from Figure 1.1a is shown in Figure 1.1c, while a change in frequency with fixed duty cycle is shown Figure 1.1d.

New challenges are presented by pulsed plasmas. In control considerations, the behavior of the plasma leads to power coupling and reflected power transients [3]. The matching transients can be used as another design parameter. For example, one may operate in delivered power mode, where the generator compensates for reflected power by increasing the nominal power and so achieves the setpoint during the whole pulse. This configuration is shown in Figure 1.2a. The other option is forward power mode, which maintains a fixed forward power setting (Figure 1.2b). The experiments

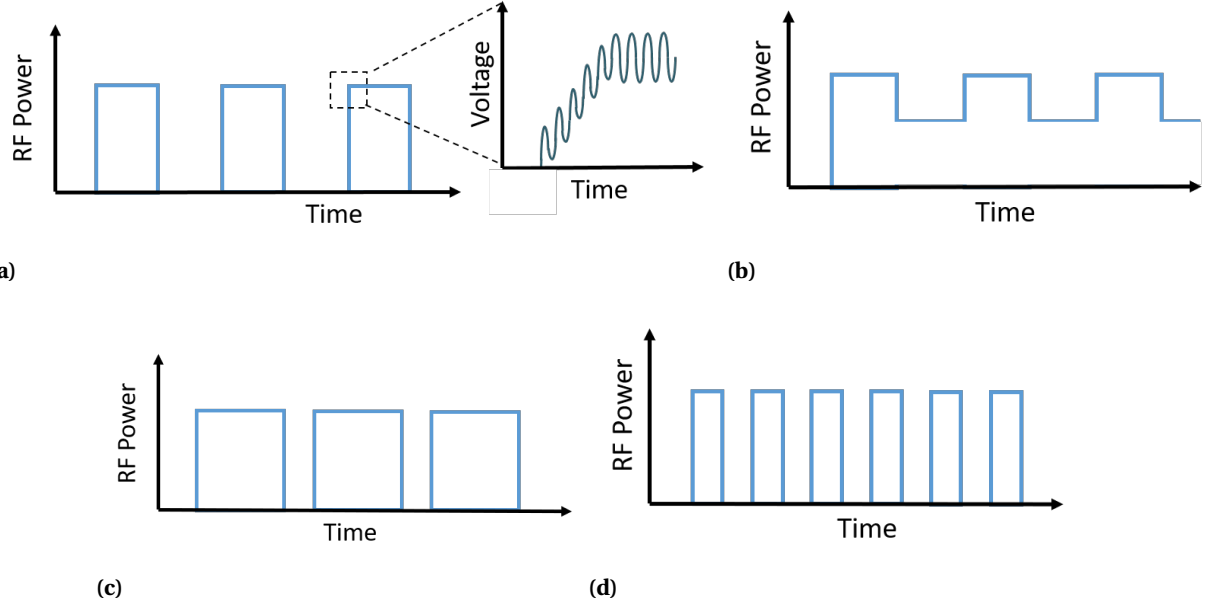


**Figure 1.1** a)Fully modulated pulsed power scheme. The square pulses represent 13.56 MHz waveforms. b) Partially modulated pulsing scheme with same frequency, duty conditions. Duty cycle and frequency variations on a) are respectively shown in c) and d) figures.

here were all performed with forward power mode and set to pseudo-steady state matching behavior. The integrated matching network was tuned so that maximum power was delivered at the end of each pulse.

Diagnostics pose an additional challenge in using pulsed plasmas, as they must operate in a time-resolved mode and each will possess some lower limit in time resolution. Langmuir probes, for instance, are restricted to the  $\mu\text{s}$  range [55]. This limits the conclusions that can be drawn from measurement. Therefore the time resolution of each experiment will be made explicit to the reader. A second difficulty arises from the large dynamic range of parameters that the plasma will oscillate through, particularly in full modulation mode. An ICP, for example, may vary from a density of  $10^{10} \text{ cm}^{-3}$  during the active glow to zero in the afterglow for low duty cycles and low pulse frequencies.

There is an alternate way to use pulsed plasmas. Rather than manipulating power in order to control plasma parameters, the plasma can be pulsed in order to *diagnose* certain plasma charac-

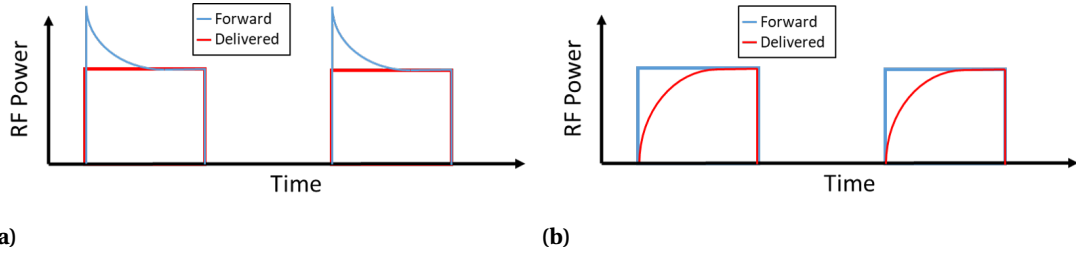


**Figure 1.2** Fully modulated power scheme with a) delivered power mode and b) forward power mode. The matching network is fixed in time, but optimized for minimal reflected power in the end of a pulse.

teristics. To avoid confusion, care will be taken to differentiate between time resolved diagnostics and pulsed plasmas as a diagnostic (PPD). In short, time resolved diagnostics can provide plasma parameters as a function of time, and analysis of those parameters under pulsed conditions can lead to plasma measurements that are otherwise unavailable. In some cases, the PPD technique can provide measurements that are relevant to constant wave (CW) plasmas as well.

An early example of PPD was the study of chemiluminescence in a SiF<sub>4</sub> plasma [21]. Optical emission spectroscopy, or OES, was performed as the time resolved diagnostic. In the emission data, a continuum of light was detected. When pulsing the power, the authors observed that the broadband continuum was largely unaffected by power modulation when measured downstream from the main glow. Due to the known gas flow velocity, they estimated that there was a 7 ms delay between the main discharge and the downstream observation port. That time scale is long after when  $T_e$  has decreased sufficiently to prevent all electron-induced emission, so they concluded that the afterglow emission was coming from chemiluminescence of SiF<sub>x</sub> species that were taking on additional atomic fluorine. Note that the chemiluminescent reaction would occur under both pulsed and steady state conditions, yet without the PPD technique they could not have identified the reaction from the OES measurement alone.

The goal of this work is to expand the diagnostic capability of two techniques: pulse induced fluorescence and hairpin resonance probes. In the former case of PIF, the technique was already classified as a PPD but it will be improved upon with an additional time-resolved OES diagnostic in this work. In the hairpin probe (HP) case, the PPD methodology will provide a novel measurement

of the perturbation surrounding the probe. This will reduce the electron density uncertainty and provide a direct measure of the extent of the perturbation surrounding plasma immersed surfaces during steady state conditions.

The thesis is laid out in the following way. First, a conceptual framework will be developed around the dynamic behaviors of pulsed plasmas. That understanding will allow the reader to understand a fundamental PPD design goal - to isolate a single parameter that varies on an unique timescale even as other parameters are varying in non-interfering ways. Following the summary of plasma dynamics, a review of previous PPD experiments will be presented. The goal in Section 1.3 is to illustrate how the knowledge of plasma dynamics is applied in PPD assumptions. The following sections of Chapter 1 will explain the HP and PIF diagnostics as they are traditionally used. Their disadvantages will be highlighted in order to motivate the improvements developed in later chapters. In both cases their drawbacks revolve around assumptions that necessarily lead to large uncertainties, but these uncertainties will be addressed through PPD experiments.

Section 1.5 provides an introduction to gas temperature measurement, which was developed in order to augment the PIF technique. The rotational temperature measurement is meant to complement the PIF technique by eliminating the need for assuming a gas temperature. The equilibrium conditions between rotational and translational motion will be explained, and a brief primer on the conceptual underpinnings of rotational spectroscopy will be provided as well. The practical formulae to simulate the rotational spectrum and obtain its uncertainty are in Section 3.1. The remaining chapters will present the results of the improved HP and PIF diagnostics. They will quantify the reduction in uncertainty from the new PPD methods in their respective chapters. Conclusions and future work are given in Chapter 5.

## 1.2 Dynamics of Pulsed Plasmas

In a standard semiconductor processing plasma, the planar coil inductively coupled plasma (ICP) with cathode bias, there are multiple options for pulsing. The cathode may be operated in CW mode as the coil is pulsed, or visa versa. With simultaneous biasing, the operator may manipulate the RF

through relative phase between waveforms or pulses, duty cycle, pulse frequency, and high/low power extent. This work has restricted its experimental focus to full power modulation in a low pressure ICP. However, the plasma dynamics in this section will be drawn from multiple plasma source designs, all at low pressure. It is often the case that rate constants in the ignition and afterglow phase are not so dependent on the type of plasma. For example, electron decay in the afterglow is determined by diffusion rather than the type of RF antenna, or how the electrons were created. What follows is a summary of the plasma dynamics most commonly manipulated in full modulation mode. The goal is to provide the reader with a general understanding of the varying time scales for these dynamics, which will inform the use of power pulsing as a diagnostic (PPD) in the rest of this work.

In recent years, pulsed plasmas have garnered interest in the semiconductor processing community. They offer multiple advantages over constant wave, or CW plasmas. For example, pulsed plasmas reduce surface charge generation, particularly when sheath collapse allows for neutralization of the surface [4, 23]. This reduces unwanted feature defects such as notching at the bottom of high aspect ratio features. An example is given by Figure 1.3a [42]. The authors demonstrated that the notching was caused by charge collection at the bottom of the feature. Whereas ion flux is relatively anisotropic, the electron flux to the wafer is largely deposited on the sidewalls and top of the photoresist due to a more isotropic velocity distribution and the retarding field formed by the plasma boundary sheath. The accumulating positive charge at the bottom of the feature eventually deflects the lower energy ions into the outer edges, which creates the notch defect [42]. The defect can be reduced by pulsing the plasma to uniquely 'turn off' a CW characteristic - the plasma sheath. This allows electrons to flow down into the bottom of the feature and neutralize the space charge causing the ion deflection in Figure 1.3b. Others demonstrated the charge neutralization and notch reduction through experiment in an electron cyclotron resonator [77].

The broader goal is to leverage power pulsing in order to further expand the plasma parameters available to operators. The ratio of neutral radical flux to ion flux on the wafer surface is a key design condition in etch and physical vapor deposition applications. The neutral flux is more difficult

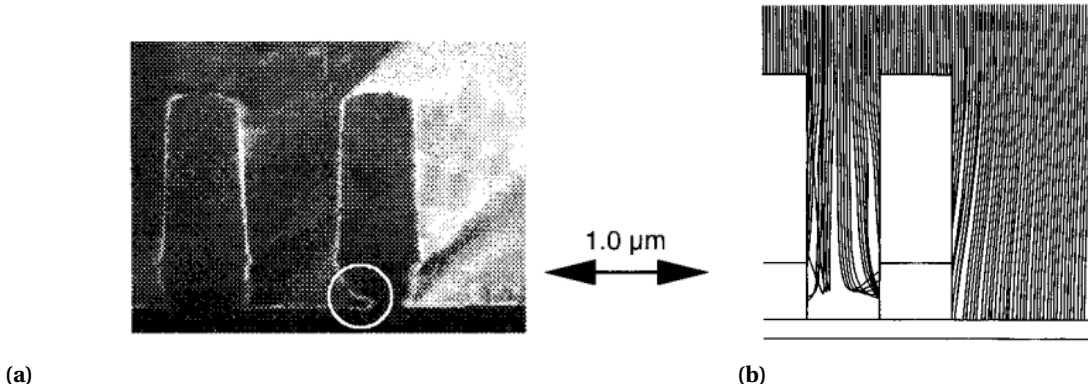


**Figure 1.3** Feature notching in polysilicon. a)  $\text{Cl}_2$  electron cyclotron resonance plasma at 10 mTorr and b) Monte Carlo simulation of 20 eV ions. [42]

to control, but the ion flux can be reduced simply by pulsing the plasma. The ion flux will drop depending on the duty cycle, while at high pulse frequencies the radical density remains constant due to its slower response time. This flux tailoring is demonstrated in Figure 1.4 [63]. Note how the Cl flux in pulsing mode,  $\Gamma_n$ , is equal to the CW flux ( $\Gamma_{nc}$ ) across all pulses in the top of Figure 1.4; the traces overlap completely. However, the ion flux ratio is reduced in the bottom of the figure for the duty cycles of 10% and 50%. The simulation showed that the ion flux tailoring improved the aspect ratio for the etching of a Si wafer [63].

Because electron collisions drive most of the plasma chemistry, electron density and temperature are key parameters of interest in pulsed plasmas. In the on-cycle of a fully modulated plasma, RF power is coupled into a lower  $n_e$ . This leads to a well-known overshoot in  $T_e$ , as shown by simulation [72] and experiment [20, 58]. Planar probe measurements in an ICP showed a  $T_e$  spike of 6 eV when power was pulsed at 1 kHz, as seen in Figure 1.5a. As one would expect, a higher pulse frequency of 10 kHz reduced the spike to being undetectable in Figure 1.5b; sufficient electrons remained from the previous pulse to couple with the RF on cycle. It should be noted that these  $T_e$  in the immediate on cycle are highly non-Maxwellian [58]. For the purposes of predicting the dynamics of the temperature overshoot, however, one can consider that the  $T_e$  spike typically lasts for  $\sim 10 \mu\text{s}$  [72]. The transient will drive a plasma potential ( $V_p$ ) overshoot as well, which will generally stabilize

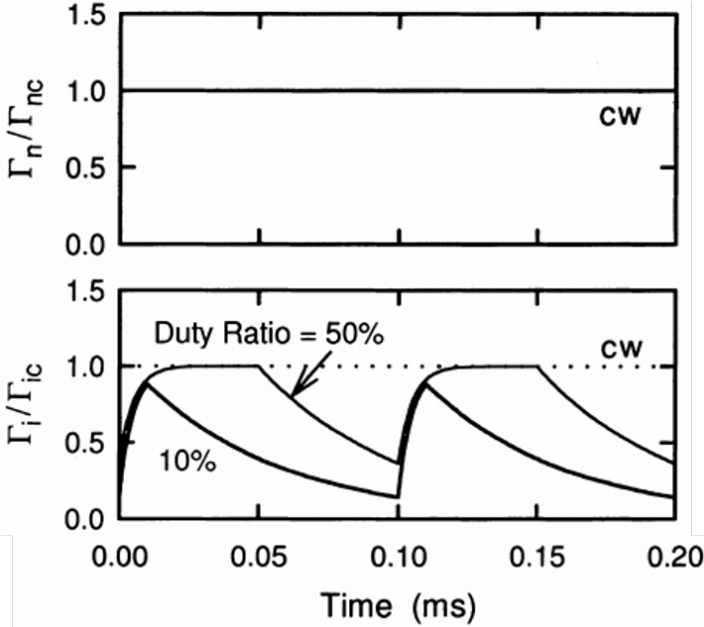


**Figure 1.4** Simulated etch of  $\text{Cl}_2$  plasma over Si wafer. On top, the time-dependent neutral flux in pulsing mode  $\Gamma_n$  is compared to CW mode  $\Gamma_{nc}$ . On bottom, the ratio of ion flux in pulsing mode  $\Gamma_i$  to CW mode  $\Gamma_{ic}$  shows modulation in time. Pulse frequency was 10 kHz Reduced from original figure in the text. [63]

to reach the steady state value within  $100 \mu\text{s}$  [18].

In the off cycle, electron confinement is lost and hot electrons freely diffuse to chamber walls at a faster rate than the low energy electrons or ions. This reduces  $T_e$  significantly, within a  $\mu\text{s}$  timescale as well. Figure 1.6 presents experimental afterglow measurements [1] that were later confirmed by global model [53]. Although the temperature decreases rapidly, the overall density is slower to respond. In the experimental data, the Ar density decreases with a time constant of  $52 \mu\text{s}$ , while the  $\text{Cl}_2 n_e$  decreases with a  $12 \mu\text{s}$  time constant.  $\text{Cl}_2$  has a faster fall rate because of electron attachment to form negative ions, which provides an additional loss mechanism and explains the more rapid  $T_e$  and  $V_p$  depletion as well. In this work, photodetachment was used to confirm the rise of  $\text{Cl}^-$  in the off cycle [1]. The time constants are not intended to be taken as universal across all pulsed plasmas, but rather as general rules of thumb one can expect under pulsed conditions. In the global model of Liberman and Ashida, the expressions for temperature and density decay are proportional to the steady state ionization rate. However, a simple takeaway from their model is that  $n_e(t) \propto t^{-0.5}$  and

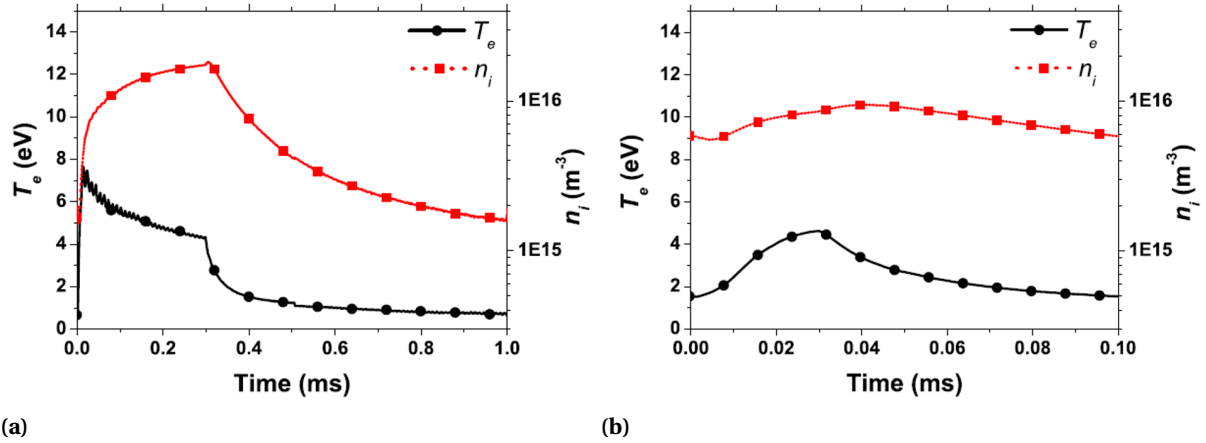


**Figure 1.5** Planar LP measurements of  $T_e$  and plasma density in 5 mTorr Ar. The stovetop ICP was pulsed at 30% duty cycle for a) 1 kHz and b) 10 kHz [20]

$$T_e(t) \propto t^{-2} \text{ [53].}$$

Others have experimentally measured the  $n_e$  dynamics in the on cycle. Greenberg et al found  $\tau_s$  to be 0.13 ms and 1.32 ms for Ar and He 500 mTorr discharges, respectively [31]. Here  $\tau_s$  refers to the time necessary to reach 90% of the steady state density in a pulsed capacitively coupled plasma (CCP), the GEC Reference Cell [62]. It is interesting to note that a post-glow  $n_e$  increase in He was also measured, as shown in Figure 1.7a. This effect is caused by metastable-metastable collisions (also called metastable pooling), where the combined energy of the excited valence electrons provide enough energy for ionization. The effect was observed in Argon as well but was not as pronounced [65]. By taking Langmuir Probe (LP) measurements in the afterglow, Overzet and Kleber were able to see electron energy probability peaks corresponding to the added energy of the metastable levels. Depending upon the gas pressure and discharge power conditions, the maximum of the metastable afterglow peak occurred from 100–300  $\mu$ s after the power is turned off. This acts as an exception to the rule of  $n_e$  decay that was introduced above.

The post-discharge  $n_e$  production can occur in electronegative plasmas as well. Microwave interferometry detected afterglow production from negative ion detachment collisions in an O<sub>2</sub> plasma [51]. Under the low  $T_e$  conditions in the afterglow, dissociative electron attachment reactions

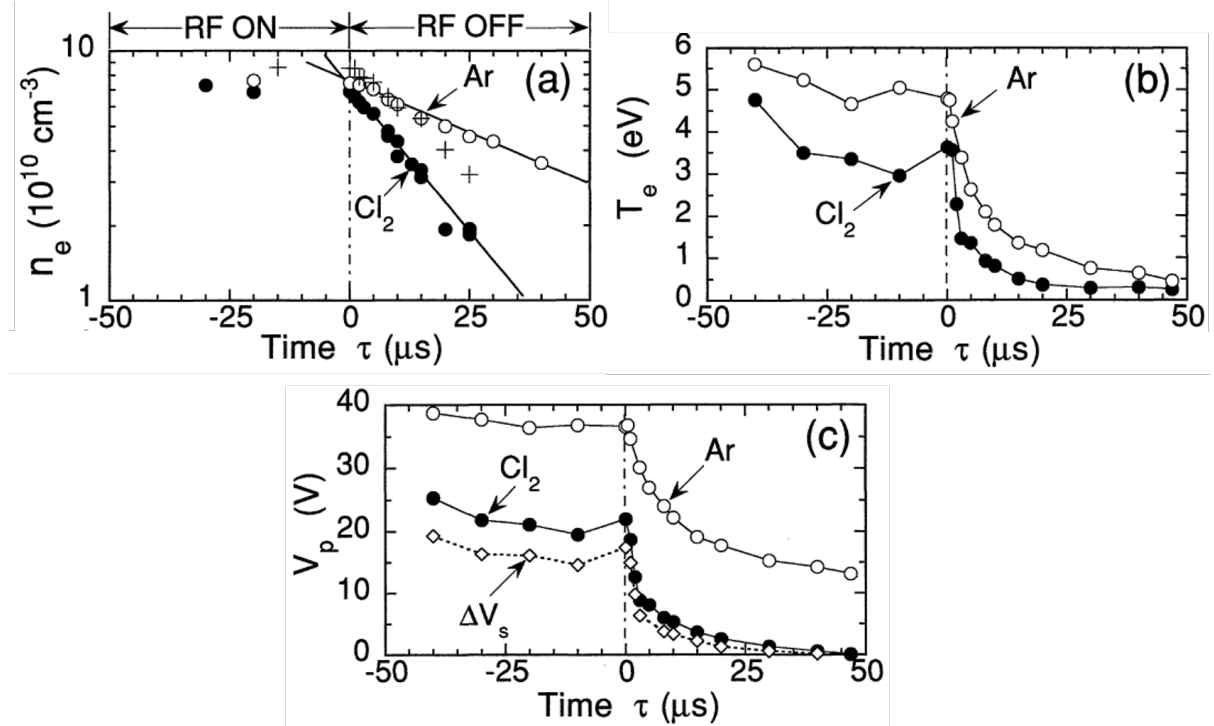


**Figure 1.6** LP measurements of off cycle in coil ICP pulsed at 5 kHz and 50% duty. Conditions were 6 mTorr for Ar, 8 mTorr for Cl<sub>2</sub> [1]

can no longer generate O<sup>-</sup> from O<sub>2</sub>. However, the negative ion collisions with neutrals continue, and these generate electrons in the afterglow while simultaneously depleting the main negative ion. The negative ion and electron densities are shown in Figure 1.7b. The difference between these electrons and the Ar/He metastable production electrons is their low energy. However, the afterglow peak occurs around 100  $\mu$ s in a similar fashion.

Collision frequency is a useful parameter to know for the pulsed plasma researcher. Electron-neutral collision frequency is given by

$$\nu = n_g \langle \sigma_g v \rangle = n_g K_{el} \quad (1.1)$$

where  $n_g$  is the neutral gas density,  $\sigma_g$  is the electron collision cross section, and the brackets signify integration with respect to electron velocity to obtain the rate constant,  $K_{el}$ . Collision frequency

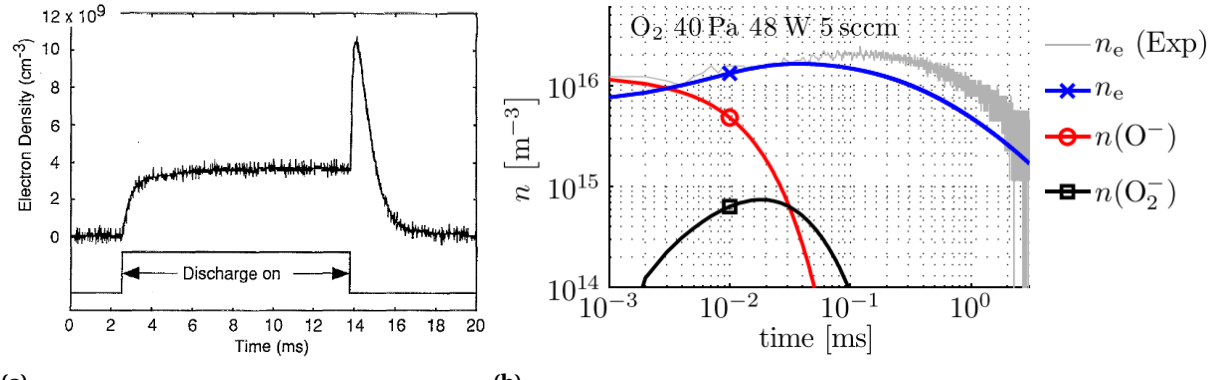


**Figure 1.7** a) Microwave interferometry measurement of line averaged  $n_e$  at 1 Torr and 75 V in the GEC Reference Cell [31]. b) Model and experimental measurement of afterglow  $n_e$  production in  $O_2$  CCP [51].

is highly dependent on gas composition and electron temperature. For an example temperature of 4 eV in 50 mTorr of Ar, the collision frequency is  $\approx 1.6$  GHz. Electron collision frequency is often compared to optical emission coefficients. For example, it may be desirable to know that light from an excited state is only occurring due to natural emission rather than collisionally induced emission. The Einstein coefficient provides the lifetime of the excited emitter to be detected. These can vary by orders of magnitude, making it necessary for the experimenter to carefully select the lines of interest in a dynamic system. For example, Phase Resolved Optical Emission Spectroscopy (PROES) can capture high energy electron beams within a 13.56 MHz RF cycle by measuring the emission from the 585.2 nm line of Ne [79]. This particular line has an expected lifetime of 14 ns, which is preferable to a line like 511.7 nm ( $\tau = 10.6\mu\text{s}$ ) [50].

Neutral-neutral collision frequency plays a considerable role in gas dynamics as pulses create heating/cooling cycles in the plasma. These cycles generate a fluctuating gas density ( $n_g$ ) that can alter other chemistry, since  $n_g$  is the 'feedstock' for desired species like ions and radicals. Neutral-neutral collision frequency can be calculated from the mean free path and thermal velocity. For an  $O_2$  example in 50 mTorr and room temperature, the collision frequency ( $\nu_g$ ) is 0.33 MHz. Typically, it is assumed that  $>5$  elastic collisions between an energetic particle and the background gas will lead to thermalization. Therefore the thermalization time in this example for gas temperature is

approximately  $15 \mu\text{s}$ . The balance between emission lifetimes and collision of the excited states is a key consideration when designing experiments measuring rotational temperature [12], as will be discussed in later chapters.

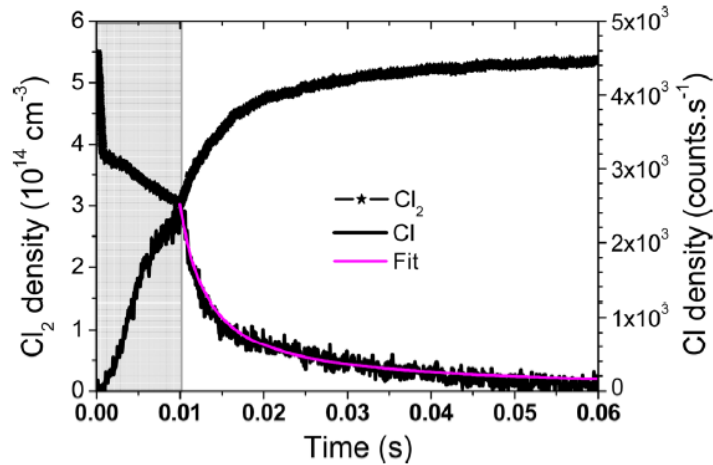


**Figure 1.8** Radical and feed gas dynamics measured through mass spectroscopy and VUV absorption spectroscopy, respectively. Chamber was a planar coil ICP operating at 20 mTorr with 800 W pulsed at 15 Hz and 15% duty cycle. The gray is the power on period, and the fit arose from a Cl loss balance [6]

As mentioned before, free radicals respond to the pulsed power in a far slower manner than that of the electrons, and so probing their dynamics requires slower pulse frequencies. In  $\text{Cl}_2$  plasma, for example, it was found that radical Cl production (and  $\text{Cl}_2$  loss) occurred on a ms time scale at the start of the pulse, then slowed [6]. This was attributed to the initial  $T_e$  spike causing accelerated  $\text{Cl}_2$  dissociation and localized heating, which then expanded the gas beyond the absorption measurement region. Both effects led to the sharp decrease in  $\text{Cl}_2$  concentration in the first moments of the pulse in Figure 1.8.

Another interesting feature in Figure 1.8 is the two-exponential behavior in the off cycle, which is more evident in the kink at .015 s of the  $\text{Cl}_2$  curve. This was attributed to the changing wall conditions, which are a sink for Cl radicals due to wall attachment and recombination. The wall in the afterglow loses active binding sites (becomes less rough), due to the reduction of high energy

ion bombardment and etching shutoff [14, 75].

**Table 1.1** General Guideline of Time Constants in Pulsed Plasmas.

Parameter	On-Cycle Time Constant	Off-Cycle Time Constant	References
$T_e$	5-10 $\mu$ s	5-30 $\mu$ s	[1, 20, 53, 58]
$n_e$	0.1-1 ms	10-100 $\mu$ s	[1, 31, 64]
$n_X$	0.1-1 ms	Same	[6, 19, 63]
$h\nu$	$10^{-8} - 10$ s	Same	[50, 79]
$V_p$	100 $\mu$ s	5-20 $\mu$ s	[1, 18]

A summary of the time constants discussed so far is given in Table 1.1. It is not the intention that the reader take these values to be true for all power modulated plasmas. Rather, they will serve as a guiding rule of thumb when considering the various dynamics going forward. A good exception to the rule for  $n_e$  decay is when afterglow production occurs in metastable pooling or negative ion detachment reactions. It is the burden of the researcher to demonstrate when a particular transient can be considered negligible relative to another.

### 1.3 Pulsed Plasmas as Diagnostics

The time dependent characteristics of pulsed plasmas can be leveraged to develop new diagnostic capability. The key idea is that transient behavior provides insight into parameters that are relevant during steady state operation. That goal, the plasma parameter, is usually obtained by its relationship to the time constants observed experimentally. The relationship between the two is developed through either computational or simplified analytic models.

As discussed in the previous section, pulsed plasmas are typified by sharp transients at the time of power on and power off. These steep transitions in secondary parameters will often occur faster than the time scale of the main parameter of interest. A common example is the time lag between free radical production and electron density. The electron density will reach a steady state within hundreds of  $\mu$ s, yet free radicals will equilibrate on the ms time scale [6, 19, 63]. The previous section

of the thesis discusses these timescales in more detail. It is the careful selection of experimental conditions and valid assumptions that allows experimenters to disregard the other transients for either being too fast, or too slow to effect the measurement of interest.

A review of pulsed plasmas as diagnostics (PPD) is presented here. Although by no means exhaustive, the discussion is meant to provide a framework for understanding these critical assumptions. From this understanding, a path towards diagnostic improvement will be laid out and lead to the following chapters that will detail the diagnostic methods used in this thesis. It should be noted that the perspective of an experimentalist motivates the discussion. It is preferable from that perspective to avoid resorting to complex computational models when making the link between the transient time constant and plasma parameter of interest, and thereby also offer a path toward advancing the computational tools for plasma source design and optimization through model validation.

Pulsing plasmas can be used as a simple, effective means of eliminating confounding factors. For example, silicon-fluorine reactions were observed by optical emission spectroscopy (OES) in a downstream plasma [21]. The focus of the work was to explain the broad continuum in Figure 1.9. The top and middle spectra were measured downstream of an RF discharge, while the bottom was measured in the active region. To eliminate the possibility of scattered light being detected from the active plasma region, the power was pulsed and OES data was acquired in the afterglow. It was found that the continuum had little response to the pulsing, while known SiF and SiF<sub>2</sub> lines were highly modulated. Therefore, the SiF and SiF<sub>2</sub> lines were present due to scattered light, but the continuum was present due to a long lived gas phase reaction. This allowed the researchers to conclude that excited SiF<sub>3</sub> was being formed through a reaction of SiF<sub>2</sub> with F or F<sub>2</sub>, which later luminesced to form the continuum. The reaction had not been deduced before because SiF<sub>2</sub> and SiF<sub>3</sub> are short-lived in F-containing gas mixtures.

An early example of experiment/model coupling is given by Kiss and Sawin [43]. In their experiments, power was pulsed with 10% variation from steady state, and with varying frequencies. Actinometry OES data determined the relative changes in reactive neutral species, and the authors compared these  $I(f_{RF})$  for various reaction networks. The transfer functions in Fourier space allowed

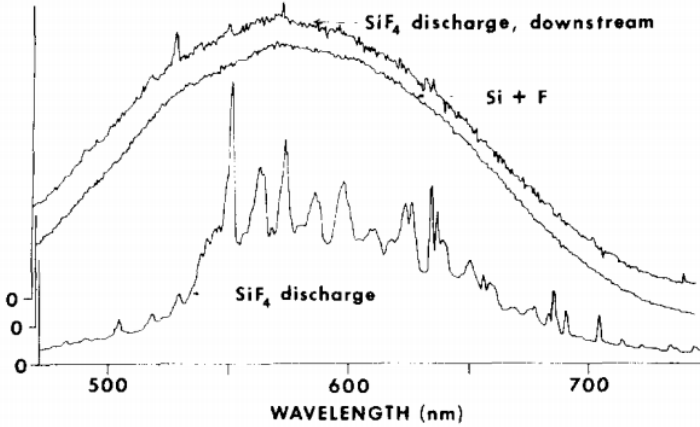


**Figure 1.9** OES data taken from the active  $\text{SiF}_4$  discharge (bottom curve), etching of Si wafer from a remote  $\text{F}_2$  plasma (middle curve), and downstream emission away from the  $\text{SiF}_4$  source (top curve). Intensities are not scaled to each other [21].

for the analysis of the phase angle between the concentration responses to the sinusoidal  $n_e$  created by the input RF power. Conceptually the analysis can be explained thus: the plasma radical will react to oscillatory power only up to a certain frequency, then the power modulation becomes too fast for the radical to respond. By analyzing the phase shift between the power and radical density maxima, conclusions can be drawn about the reaction networks [43, 44].

An analogy can be made to a pendulum in order to explain the technique. If a pendulum with fixed mass and length is pushed/pulled with an identical sinusoidal impulse but varying frequency, then the phase shift between impulse and pendulum response will saturate for high frequencies. Suppose the experiment was adjusted so that the impulse was applied to a secondary pendulum above the first, unbeknownst to an observer who can only measure the impulse and the bottom pendulum. The saturation phase shift would be greater since the observed pendulum is further removed from the impulse. Knowing some theory about pendulums, the observer could conclude that the impulse was being applied to the top pendulum *without observing it directly*. For the  $\text{CF}_4$  plasma case, the power modulation is the impulse, the top pendulum is the unknown, and the secondary pendulum is the measured  $\text{CF}_2$  emission. A Bode plot (of phase shift versus frequency) for the one-step production of  $\text{CF}_2$  is given in Figure 1.10a. From experimental data of  $\text{CF}_2$ ,  $\text{CF}$  and

F emission, the authors concluded that the dominant production mechanism for  $\text{CF}_2$  must consist of two reaction steps from the  $\text{CF}_4$  feed gas. This led to the modified reaction model, with good fit in Figure 1.10b.

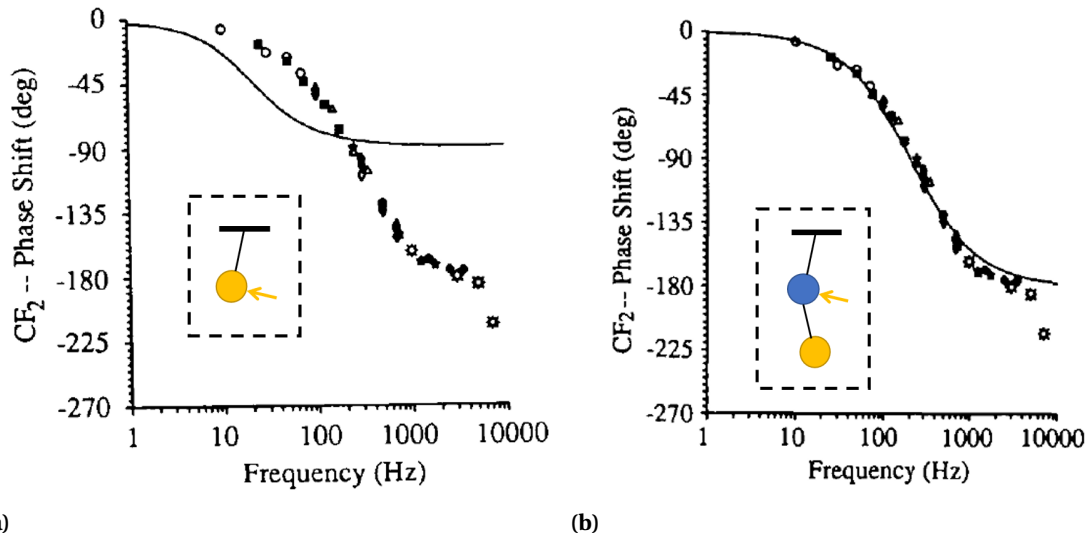


**Figure 1.10** Bode plots with pendulum analogs. Pendulum inset for the relevant transfer function model is not original to text. Yellow represents information available to experimentors, blue an unknown. a)Bode plot of single step formation of  $\text{CF}_2$  from electron impact on  $\text{CF}_4$ . Solid line represents the transfer function model, points represent experimental data. b) Bode plot of modified transfer function, which considers an unknown intermediary reaction. Conditions are a CCP with 95/5%  $\text{CF}_4/\text{Ar}$  feed gas at 500 mTorr and  $0.81 \text{ W/cm}^{-3}$  power density [43].

Implicit in their assumptions was the time response of the electrons. If power is being modulated, then electrons could very well act as a third 'pendulum' between the power impulse and the free radical response. However, the electron response to field variation is characterized by plasma frequency in the GHz range, well outside the Hz/kHz region of the experiment. The other electron dynamic to consider is temperature. This response is on the  $\mu\text{s}$  timescale, as discussed in the preceding section. In actinometry experiments, the Ar actinometer provides a reliable indicator of

the relative radical concentration  $[X]$ . However, actinometry is inherently reliant on the expression

$$\frac{I_X}{I_{Ar}} = \frac{\int n_X \sigma_{ex,X} n_e f(E) \sqrt{2E/m_e} dE}{\int n_{Ar} n_e \sigma_{ex,Ar} f(E) \sqrt{2E/m_e} dE} \quad (1.2)$$

$$\frac{I_X}{I_{Ar}} = \frac{C n_X}{n_{Ar}} \quad (1.3)$$

Where ratio of the electron impact cross sections  $\sigma_{ex}$  for each species determine the correction factor  $C$  [54]. The trace amount of added argon  $n_{Ar}$  is known, so Equation 1.3 can be used to determine the radical ground state density without directly knowing the electron density or EEDF in Equation 1.2. As discussed previously, however, the  $T_e$  response to time can lead to an overshoot in the high power regime [1, 53, 72]. The transient EEDF can lead to dissociative excitation reactions, which become more prevalent at higher  $T_e$ . In that case, Equation 1.2 becomes

$$\frac{I_X}{I_{Ar}} = \frac{\int n_X n_e \sigma_{ex,X} f(E) \sqrt{2E/m_e} dE + \int n_{CF_4} n_e \sigma_{diss,CF_4} f(E) \sqrt{2E/m_e} dE}{\int n_{Ar} n_e \sigma_{ex,Ar} f(E) \sqrt{2E/m_e} dE} \quad (1.4)$$

$$\frac{I_X}{I_{Ar}} = \frac{C_1 n_X}{n_{Ar}} + \frac{C_2 n_{CF_4}}{n_{Ar}} \quad (1.5)$$

The amount of dissociation of  $n_{CF_4}$  is unknown experimentally, however. By restricting the variation in RF power to 10%, the authors avoided the transient  $T_e$  overshoot. The authors also assumed spatial homogeneity. In CCP systems, stochastic heating from the RF potential creates a high energy electron beam, leading to axially dependent emission. Phase Resolved Optical Emission Spectroscopy was developed around this phenomenon [79]. However, the time scale of one RF period, 76 ns, is far shorter than the ms transients of interest. Therefore the intensity contribution from the hot electron beam is averaged out in the OES acquisition.

A relatively simpler technique used laser absorption in a  $BCl_3/Cl_2$  ICP system [87]. The plasma was pulsed with full power modulation, and a 265 nm diode laser probed the  $BCl$  density in the afterglow. The decay was fit to wall and volume losses, and by changing the  $Cl_2$  density, the authors

were able to determine the volumetric loss constant as well as the surface sticking probability.

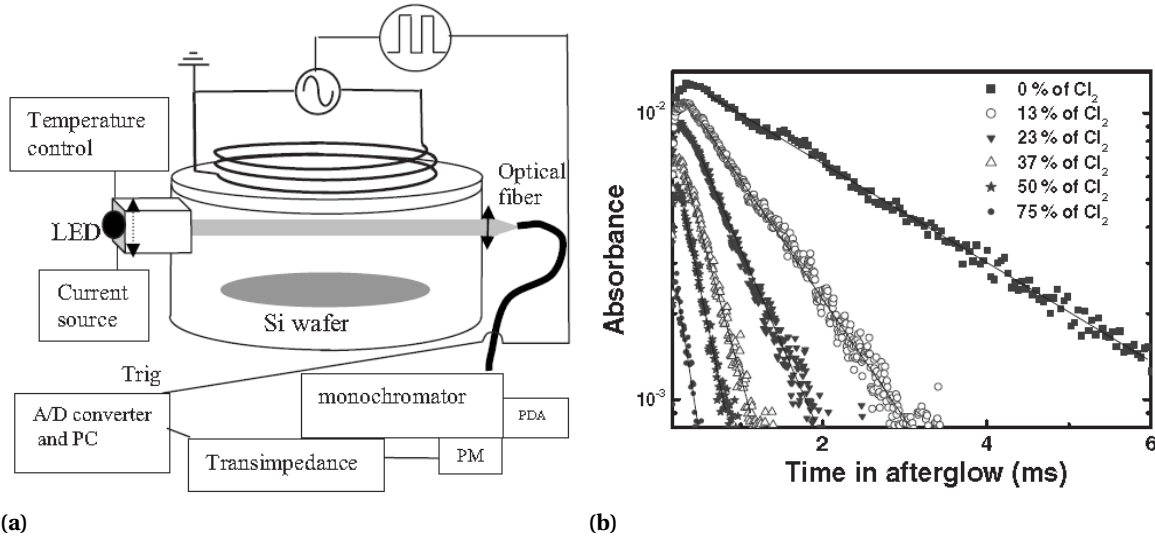


**Figure 1.11** a) LED absorption setup. Chamber dimensions are  $r = 27$  cm,  $h = 17$  cm. b) LED absorbance of BCl in the plasma afterglow. Power was pulsed at 150 Hz and 2% duty cycle in an ICP. Gas composition was varied as overall pressure was held at 5 mTorr [87].

One can see an absorption increase in the immediate afterglow, up to 500  $\mu$ s in the 0% Cl<sub>2</sub> case of Figure 1.11. The authors attributed this to the higher order diffusion modes. In short, the solution to the diffusion equation is given by an infinite series of eigenfunctions. The higher order solutions decay more rapidly in time, and so are often ignored in favor of the fundamental solution. During the initial afterglow they may contribute enough to cause a more rapid decay, as was concluded by others [9]. It is the opinion of the author that this is an unsatisfactory explanation. The absorbance *increases* during the initial afterglow, which is not explained by higher diffusion modes. It is difficult to speculate on other explanations, for two key reasons. The on cycle of 133  $\mu$ s could cause problems. At that short a pulse, the radical and electron densities surely did not reach steady state; this could cause pulse to pulse variation. Also, the chamber itself is comprised of many materials. At a low pressure of 5 mTorr, the mean free path is approximately 2 cm, so strong conclusions cannot be drawn about which specific surface caused the sticking coefficient of 0.3 that the authors reported.

The analysis was strong, however, and could be repeated if the chamber material was made more homogenous in a higher duty cycle pulse.

## 1.4 Pulse Induced Fluorescence

In low pressure plasmas, free radical loss through volumetric reactions is often negligible due to the likelihood of collisions that could lead to loss. For example, it is possible that two radicals could recombine in a gas phase collision to form the parent molecule. However, the event is unlikely because radical concentrations typically remain low compared to the feed gas. This is why one could say that the gas is in thermal equilibrium yet these collisions do not lead to appreciable radical loss. Rather, free radical loss is often determined by surface reactions and pumping out of the chamber. To acquire the loss rate, radical density must be measured in non-steady state conditions. Previous experiments created a decay through geometry; they flowed neutral effluent from an oxygen source plasma into a remote region with the surface of interest [5, 11, 91]. The measurement of geometric decay was determined from the chemiluminescent reaction of atomic oxygen with titrated nitrogen. Together with the known gas flow rate, a decay rate in time was determined.

The flow tube approach is unique to chemiluminescent species. Remote source experiments, on the other hand, are more flexible in their diagnostic capability. These consist of a neutral plasma source and an independent ion beam source being directed onto a substrate [22, 46, 47]. A simple diagram of the setup is shown in Figure 1.12. The ion beam sputter cleans the surface prior to neutral beam treatment. The effluent products coming off of the surface are then measured with mass spectrometry. The drawback (shared with flow tubes) is that additional plasma treatment effects are lost compared to an *in situ* measurement. For example, ion bombardment and etching can create more active sites for radical adsorption through the simple increase in surface area [6, 14, 75]. It is for this reason, and the variety of density measurement methods, that surface loss coefficients have historically been reported with wide ranges over the same compound/surface system. Atomic chlorine loss on stainless steel, for example, varies by as much as  $0.05 < \gamma < 0.81$  in the literature [46, 73]. For the interested reader, a thorough review of surface recombination measurement methods is

provided in [22].

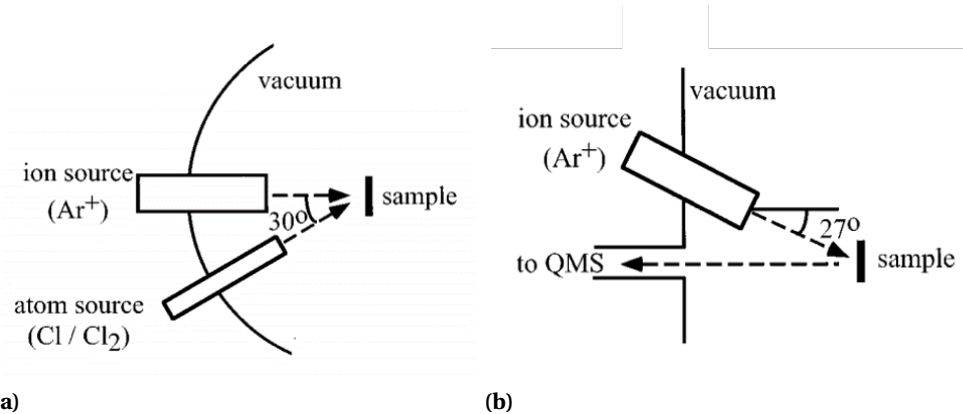


**Figure 1.12** Top (a) and side (b) views of remote beam experiment for determining radical recombination coefficients. The Quadrupole Mass Spectrometer was differentially pumped, and the substrate temperature was fixed by a heating element or cooling channel [46]

Because surface reactions can often be the dominant loss mechanism, this uncertainty presents a large challenge to simulation accuracy and subsequent chamber design. In applications such as semiconductor etch, the radical flux to the etch substrate is a key parameter to control the etch rate. An example simulation for an oxygen plasma in a processing chamber is shown in Figure 1.13 to motivate the discussion [26]. In that work, full reaction networks are considered with power coupling in a 2D model of a planar coil ICP. The authors varied the recombination coefficient for all of the plasma facing materials, and obtained the shown densities at the radial and axial center of the plasma. One can see that the positive ion densities, in particular, vary greatly across the oxygen recombination coefficients considered.

Pulse Induced Fluorescence, or PIF, provides *in situ* surface loss coefficients by pulsing the plasma as a diagnostic. The density measurement in the plasma afterglow is found from the radical optical emission, and the emission as a function of afterglow time is compared to the pseudo steady state emission. The relative emission intensities provide a decay constant without the need to determine absolute radical densities.

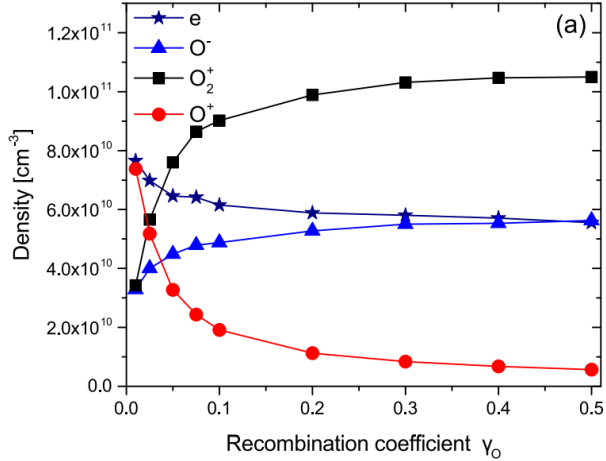


**Figure 1.13** Hybrid Plasma Equipment Model simulation of semiconductor processing planar ICP. Plasma was pure  $O_2$  at 500 W and 10 mTorr [26].

Under normal circumstances the plasma afterglow does not emit;  $T_e$  has dropped sufficiently to prevent the excitation of electronic states. PIF relies on turning the plasma back on in order to capture the radical density at that particular moment. Conceptually, the alternate pulsing schemes are shown in Figure 1.14. The ideal measurement is given in Figure 1.14a, by the green time steps. However, the power must be triggered again to capture the start of the next on cycle. This is the idea behind a fixed pulsing scheme in Figure 1.14c, which has standard lengths of 10 ms with variable gaps in between. The long on period ensures that the plasma reaches steady state at each cycle. The probe pulse scheme has a fixed frequency for the main, 10 ms pulse while varying the probing pulse in between. The probing pulse trigger is drawn higher to illustrate that it will activate the light measurement and the generator. The main pulse does not trigger the OES measurement save for determining the steady state emission value. The advantage for the probing pulse scheme is that the overall power deposition into the plasma is kept constant for each data point. This minimizes variation in wall temperature, which can shift the rates of radical surface reactions [10].

The PIF method was first developed in a  $CF_4$  plasma experiment to measure  $CF_2$  and F radical loss rates [35]. The  $CF_2$  results were validated against LIF measurements, and demonstrate good agreement in Figure 1.15. An Ar actinometer was used to correct for  $n_e$  transients in the early on

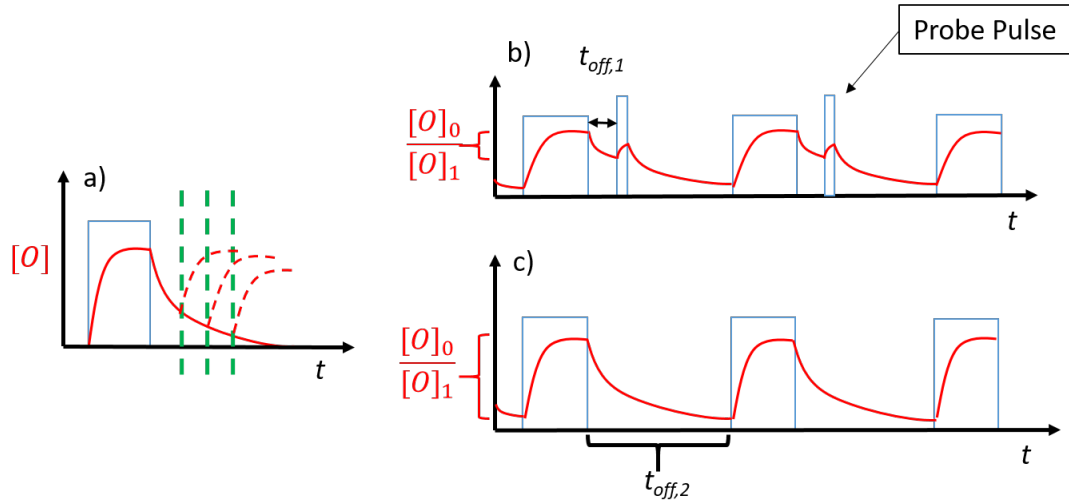


**Figure 1.14** a) Idealized representation of atomic oxygen density (red) in the afterglow of the RF pulse (blue) b) Probing pulse scheme to obtain snapshot in decay density. c) Fixed pulse scheme to determine  $[O]$  decay.

cycle. After validation of the PIF technique, the authors used it to characterize F decay. This had not been possible with LIF as the lowest energy transition of F requires vacuum UV.

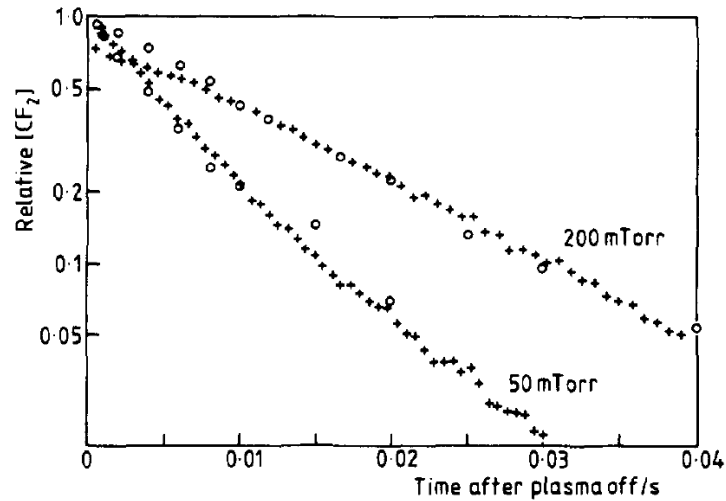


**Figure 1.15** LIF (+) comparison with actinometered PIF (o) of  $CF_2$  for two pressures. The relative concentration is based on signal of the main pulse [35].

The raw, actinometered F signal is shown in Figure 1.16a for various off times. The initial intensity point on each curve can be taken and plotted against the off time to generate Figure 1.16b, a semilogarithmic plot with excellent goodness of fit. Note the sensitivity to the presence of a Si wafer, which increases the loss rate dramatically for both gas compositions.

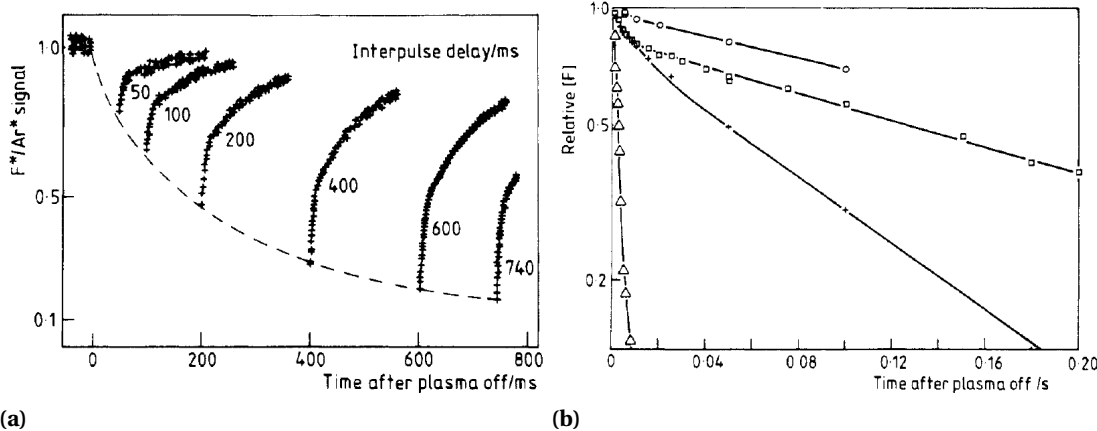


**Figure 1.16** a) F/Ar actinometry signal for PIF in CF<sub>4</sub> plasma with 5% Ar. b) Decay curves for PIF of CF<sub>4</sub>/Ar plasma in the presence ( $\Delta$ ) and absence ( $\square$ ) of a Si wafer. CF<sub>4</sub> with 10% O<sub>2</sub> and 5% Ar is plotted in (+) and (o) for the presence and absence of Si, respectively [35].

Later experiments were more carefully designed so as to obtain loss rates on a single material, rather than a composite of reactor materials. PIF was used to measure surface loss rates of O in a pyrex tube powered by a microwave source [14]. Figure 1.17a shows the raw O emission intensity for various probing pulses in the off cycle. The authors modified the original technique by using probing pulses. They also projected the signal back to  $t = 0$  rather than taking the first intensity point. One can see an overshoot in emission intensity for longer off times. These are caused by the  $T_e$  spike at the beginning of the on cycle, which was introduced in Figure 1.5a. The effect is weaker at short off times because  $n_e$  has not decayed sufficiently and the remaining electrons split the incoming power. The effect on emission is dependent on chemical species, line choice, and power source; an overshoot was not observed in Figure 1.16a, for example.

Cartry *et al* also compared two emission lines in their measurement of O loss coefficient [14].

The authors attributed the difference in Figure 1.17b and the decay constant results to the varying dissociative excitation offset, which was measured by taking the  $t = 0$  projection for a 1000 ms off time. For 844 nm the intensity was nearly zero, but for 777 nm the intensity was 15% relative to the steady state glow [14]. Another feature is the two decay behavior; this is caused by surface morphology changes in the near or late afterglow. When the plasma is active, ion bombardment creates more active surface sites for O atoms to adsorb to. In long off periods, the surface returns to normal pyrex.

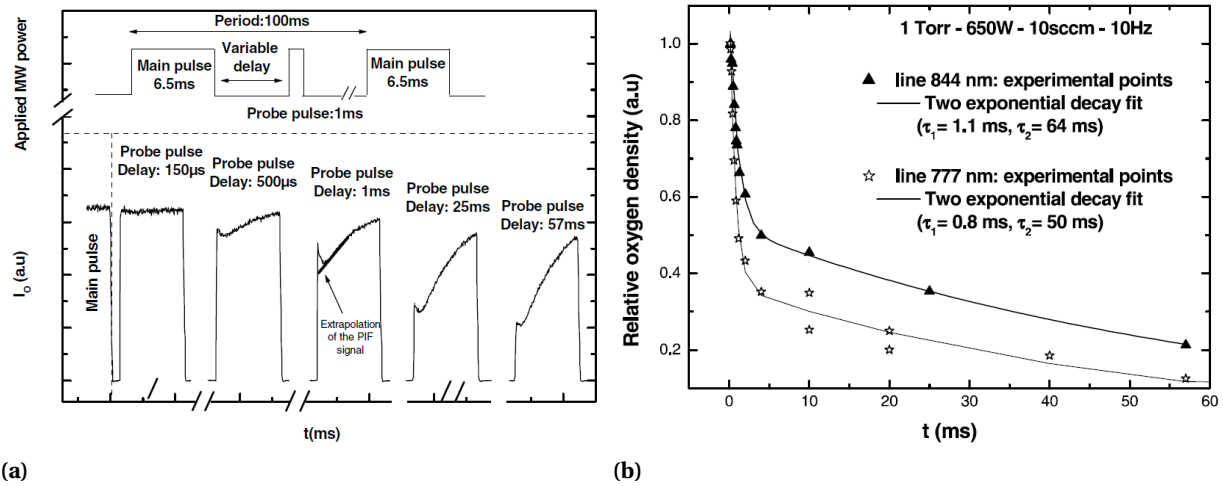


**Figure 1.17** a) PIF probing pulse configuration with raw oxygen emission of the 844 nm line. b) comparison of resulting decay curves for 844 and 777 nm. [14]

H and Cl surface chemistry has been studied as well in an ICP powered by a 13.56 MHz generator [19]. The authors compared the actinometered signal to the raw H intensity decay, and found good agreement. The curves are plotted in Figure 1.18. Actinometry was found to be unnecessary in determining the H surface loss rate on aluminum oxide. A separate comparison was made for a longer main pulse of 100 ms, which is plotted in the inset. The results were similar enough that the authors used 20 ms main pulses for their remaining data acquisitions. This saves time for the experimentalist.

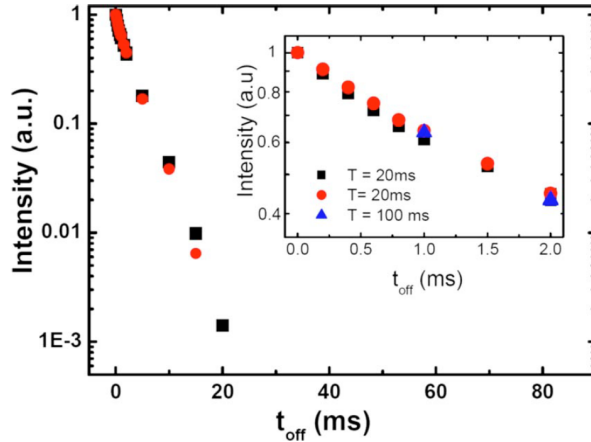
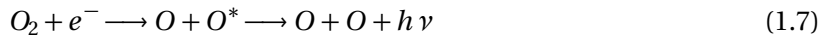


**Figure 1.18** H decay results with (black squares) and without (red circles) Ar actinometry. The inset shows two data points for main pulses lasting 100 ms long (blue triangles) rather than 20 ms [19].

Atomic oxygen loss on quartz will be considered in this thesis. The goal is to create an accurate diagnostic for determining  $\beta$  in other dielectric/radical combinations. Oxygen on quartz is a good start because it is a reaction of concern in processing plasmas, which often have quartz viewports for diagnostic or control purposes.

There are two main pathways through which emissive atomic oxygen is generated. The first is through electron collisions that split molecular oxygen and then excite the ground state radical oxygen. The second is through dissociative excitation, in which electron collision provides enough energy to split the molecule and create an excited radical that later emits. The dissociative excitation reaction is undesirable because the emission does not reflect the concentration of ground state atomic oxygen. The analysis corrects for this effect, which will be explained in more detail later.



In the plasma afterglow, electrons are present but do not possess the energy to facilitate these reactions because the data is taken on the ms time scale, while the  $T_e$  has decreased within  $\mu\text{s}$  [1, 53]. Therefore the balance equation becomes a simple loss formulation.

$$\frac{dO}{dt} = -k_{pump}O - k_{wall}O \quad (1.8)$$

$$\frac{dO}{dt} = -k_T O \quad (1.9)$$

Here, the total loss rate  $k_T$  is determined experimentally. The pump loss rate,  $k_{pump}$ , is known based on flow rate and chamber geometry. The wall loss coefficient is related to  $\beta$  by [17, 19]

$$\frac{1}{k_{wall}} = \frac{\Lambda^2}{D} + \frac{V2(2-\beta)}{Sv_{th}\beta} \quad (1.10)$$

Where  $\Lambda$ ,  $V$ , and  $S$  are the characteristic diffusion length, volume, and chamber surface area, respectively. The diffusion coefficient of O through  $O_2$ ,  $D$ , is found for an assumed temperature in the literature [66]. The thermal velocity ( $v_{th}$ ) is calculated for the same temperature. To summarize the PIF technique, relative intensities are determined from the afterglow decay behavior of atomic oxygen, and with varying off time. These data are fit to a decay constant  $k_T$ , which allows for the determination of  $\beta$  through Equation 4.1.

## 1.5 Gas Temperature Measurements

### 1.5.1 Survey of Gas Temperature Techniques

Gas temperature is a useful parameter for plasma source design. For instance, an atmospheric pressure plasma jet was designed to operate at near-room temperatures so as to be safe for biomedical applications on human tissue [88]. In that work, the spectroscopic data collected from OH emission allowed for determination of  $T_g$  to within 20 K of a thermometer. Thermometers and thermocouples cannot be used in the low pressure plasmas studied here due to heating from ion bombardment,

however.

The OES technique relies upon measuring the rotational distribution of the observed state. In a normal gas, collisions between molecules create a distribution of rotational states in the same way they will create a Boltzmann distribution of translational velocities. At equilibrium, the rotational temperature is equal to the gas temperature because the energy differences between rotational states are sufficiently low to allow for thermally induced motion to mediate energy transfer. This is not the case for electronic temperature, which is orders of magnitude higher in nonequilibrium plasmas.

Besides passive OES, the two most common gas temperature techniques are Two-photon Absorption Laser Induced Fluorescence (TALIF) and Doppler broadening. TALIF has the advantage that it can probe the ground state rather than depend on the UV-vis emission from an electronically excited molecule, as OES does [7]. The downside is that LIF requires more complex instrumentation. Doppler broadening is a good option because it simply requires passive data from a single line. However, the broadening function given by [12]

$$\lambda_{FWHM} = 7.16 \times 10^{-7} \lambda \sqrt{\frac{T_g}{M}} \quad (1.11)$$

necessitates the use of light particles under high temperature conditions.  $M$  is provided in amu and  $T_g$  in units of K. As an example to consider, a He line at 587.6 nm and 500 K would have a broadening of only 5 pm. This is well below the resolution threshold of common low-cost spectrometers, which is why the Doppler broadening technique is most often used in fusion or laser plasmas [39].

For its experimental ease of use, and wide applicability, rotational temperature is the diagnostic of choice for many experimentalists [12, 94, 95]. The validity of  $T_r = T_g$  is dependent on equilibrium between rotational and translational motion. This is not always the case in a plasma. For UV-vis OES, the experimenter is reliant on electron collisions to excite the plasma sufficiently to be observed. An electron lacks the mass to collisionally change the rotational inertia of a molecule. However, collisions with ions and neutrals may change the rotation state. Also, in electron-impact dissociation

there may be energy deposited into rotational states. For instance, the rotational temperature of OH radicals is often inflated due to dissociative excitation of the H<sub>2</sub>O molecule [12].

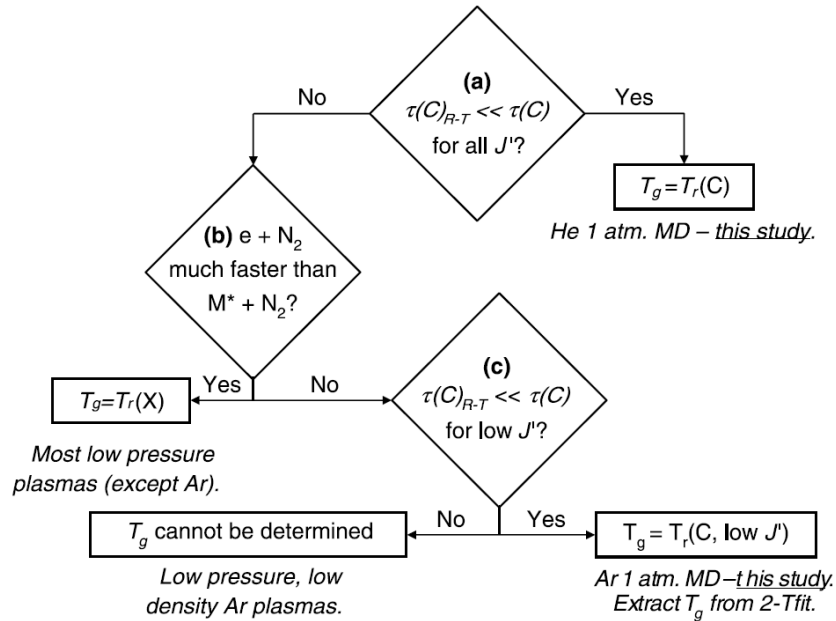


**Figure 1.19** Flowchart for rotational equilibrium with translational temperature for the second positive N<sub>2</sub> system.  $\tau(C)_{R-T}$  and  $\tau(C)$  represent the inverse of collision frequency and Einstein coefficient, respectively [89]

The conditions for rotational-translational equilibrium were succinctly summarized by Wang *et al* in [89]. The validity flowchart is reproduced in Figure 1.19. In the ideal low pressure plasma case, electron collisions provide a 1:1 mapping of the ground state rotational distribution onto the excited electronic state. The emission from the excited electronic state then provides  $T_r$  and thus  $T_g$ . The caveat is that the molecule must not transfer energy well with the electronic excitation states of other gases. For this effort, Ar must not be present in sufficient amounts so as to cause collisions between Ar\* and N<sub>2</sub>. The energy level of Ar\* metastables is similar enough to couple well with N<sub>2</sub> and produce additional  $C^3\Pi_u$  states which have now undergone rotational transitions. In their work, the metastable coupling was restricted to higher  $J'$  states, which allowed for a two-temperature

simulation of the rotational band. The authors then used the lower temperature result as  $T_g$ .

The other condition when  $T_r = T_g$  is commonly found in high pressure plasmas. In this case, the excitation processes may significantly alter the rotational distribution of the ground state molecule. However, the excited state is sufficiently long-lived in order to collide and re-equilibrate with the background gas. Therefore the validity of this assumption is judged by comparing the collision frequency and de-excitation lifetimes.

### 1.5.2 Rotational Spectra Theory

A brief primer on rotational spectroscopy is presented here. For the researcher in search of practical formulas for replication of results, refer to Section 3.1. Plasma OES is concerned with electronic, vibrational, and rotational transitions of the molecules. The Born-Oppenheimer approximation posits that the total energy state can be represented as an independent sum of these components [38, 49].

$$E = E_e + E_v + E_r \quad (1.12)$$

The energy levels are obtained by solving the time-independent Schrödinger equation

$$\hat{H}\Psi = E\Psi \quad (1.13)$$

in which  $\hat{H}$  is the Hamiltonian operator and  $\Psi$  is the wavefunction of the combined electron states. The Born Oppenheimer approximation allows for the full Hamiltonian to be split into separate components. Because this work is concerned with modeling a single rotational band, a simple example will be considered, that of a rigid rotor. The rigid rotor is a model for a diatomic molecule with fixed bond length, and will lead to the rotational quantum number  $J$ . Molecular vibrations will not be considered, and electronic levels arising from solutions to the central potential formulation will be ignored as well. The other 'classic' models are the harmonic oscillator and the hydrogen atom, which respectively introduce the vibrational and electronic energies. These can be found in the standard spectroscopy texts [38, 49]. Figure 1.20 shows the molecular model. The spherical

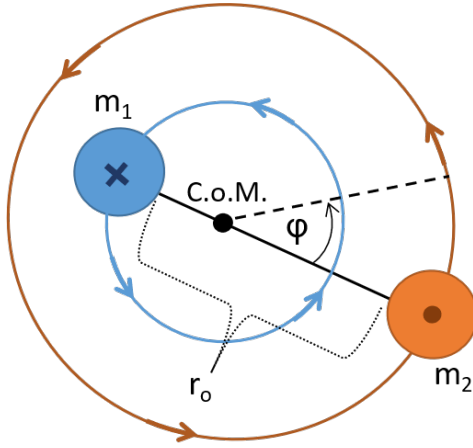


**Figure 1.20** Rigid rotor configuration. Bond length is fixed at  $r_o$  and  $m_1 > m_2$ . Molecule is allowed to rotate in two directions. The  $\theta$  direction, in and out of the page, is not shown.

coordinate Hamiltonian is given by

$$\frac{-\hbar^2}{2\mu r_o^2} \left\{ \frac{1}{\sin\theta} \frac{\partial}{\partial\theta} \sin\theta \frac{\partial}{\partial\theta} + \frac{1}{\sin^2\theta} \frac{\partial^2}{\partial\psi^2} \right\} \Psi = E_r \Psi \quad (1.14)$$

Note that ordinarily the Hamiltonian is the sum of kinetic and potential energy, but here the potential energy is zero. Also, the  $r$  derivatives have been removed from the Hamiltonian as the rigid rotor fixes  $r = r_o$ . First, rotational inertia is substituted into Equation 1.14.

$$I = \frac{m_1 m_2}{m_1 + m_2} r_o^2 \quad (1.15)$$

$$I = \mu r_o^2$$

The reduced mass is given by  $\mu$ . A separation of variables approach is used to solve Schrödinger's equation. This sets  $\Psi(\theta, \psi) = \Theta(\theta)\Phi(\psi)$  to obtain

$$\frac{-\hbar^2}{2I} \left\{ \frac{1}{\sin\theta} \frac{\partial}{\partial\theta} \sin\theta \frac{\partial}{\partial\theta} + \frac{1}{\sin^2\theta} \frac{\partial^2}{\partial\psi^2} \right\} \Theta(\theta)\Phi(\psi) = E_r \Theta(\theta)\Phi(\psi) \quad (1.16)$$

$$\frac{1}{\Theta(\theta)\Phi(\psi)} \left\{ \sin\theta \frac{\partial}{\partial\theta} \sin\theta \frac{\partial}{\partial\theta} + \frac{1}{\sin^2\theta} \frac{\partial^2}{\partial\psi^2} \right\} \Theta(\theta)\Phi(\psi) = \frac{-2IE_r \sin^2\theta}{\hbar^2} \quad (1.17)$$

The constants are grouped on the right hand side into  $\gamma$

$$\gamma = \frac{2IE_r}{\hbar^2} \quad (1.18)$$

and the final separation of variables leads to

$$\frac{1}{\Theta(\theta)} \left\{ \sin\theta \frac{\partial}{\partial\theta} (\sin\theta \frac{\partial\Theta(\theta)}{\partial\theta}) + (\gamma \sin^2\theta) \Theta(\theta) \right\} = \frac{-1}{\Phi(\psi)} \frac{\partial^2\Phi(\psi)}{\partial\psi^2} \quad (1.19)$$

For both sides to be equal, they must both evaluate to some constant  $m^2$  in the nontrivial case. The two differential equations to solve are then

$$\sin\theta \frac{d}{d\theta} (\sin\theta \frac{d\Theta(\theta)}{d\theta}) + (\gamma \sin^2\theta - m^2) \Theta(\theta) = 0 \quad (1.20)$$

$$\frac{d^2\Phi(\psi)}{d\psi^2} + m^2 \Phi(\psi) = 0 \quad (1.21)$$

Equation 1.21 is the well known 2nd order differential equation, which has solutions of the form

$$\Phi(\psi) = C_1 e^{im\psi} + C_2 e^{-im\psi} \quad (1.22)$$

Taking the positive solution, we apply the cyclic boundary condition that  $\Phi(\psi) = \Phi(\psi + \pi)$

$$\begin{aligned} e^{im\psi} &= e^{im(\psi+2\pi)} \\ e^{im\psi} &= e^{im\psi} e^{im2\pi} \end{aligned} \quad (1.23)$$

which can only be true if  $m$  is an integer. The second differential equation can be reformulated into the Legendre differential equation, but first a change of variables must be made. By substituting  $x = \cos(\theta)$  and  $dx = -\sin(\theta)d\theta$ , the problem is rewritten

$$\sin^2\theta \frac{d}{dx} (\sin^2\theta \frac{d\Theta(x)}{dx}) + (\gamma \sin^2\theta - m^2) \Theta(x) = 0 \quad (1.24)$$

Then the substitution of the trigonometry identity  $\sin^2\theta = 1 - \cos^2\theta$  is made.

$$\frac{d}{d\theta}((1-x^2)\frac{d\Theta(x)}{d\theta}) + (\gamma - \frac{m^2}{1-x^2})\Theta(x) = 0 \quad (1.25)$$

By setting  $\gamma = J(J+1)$ , the equation has been recast as the Associated Legendre Differential Equation, which has known solutions for each  $J \geq |m|$ . Therefore the energy levels can be determined from the relationship between the index of the Legendre polynomial solutions,  $J$ , and Equation 1.18.

$$E_r = \frac{\hbar^2 J(J+1)}{2I} \quad (1.26)$$

Besides rotational energy levels, the rigid rotor derivation has also introduced the idea of degeneracy. For example, a  $J = 1$  configuration will have three energy-equivalent solutions for unique  $m = -1, 0, 1$ . Rather than energy levels  $E_r$ , it is standard practice to discuss the term values of the molecular states, which are the wavenumber of the light emitted by such a state in units of  $\text{cm}^{-1}$ .

$$F_r(J) = \frac{E_r}{hc} \\ F_r(J) = BJ(J+1) \quad (1.27)$$

The coefficients in front of the  $J$  expression have been grouped into the molecular rotation constant,  $B = \hbar/4\pi I c$ . If the model is adjusted to allow for stretching of the bond length as the molecule rotates, the energy levels are then more accurately characterized by [38]

$$F_r(J) = BJ(J+1) - DJ^2(J+1)^2 \quad (1.28)$$

The new correction term,  $D$ , is often orders of magnitude smaller than  $B$ . For example, the ground state of the  $C_2$  radical will have  $B$  and  $D$  values of  $1.811$  and  $7 \times 10^{-6} \text{ cm}^{-1}$ , respectively [37]. The history of spectroscopy is the history of refining these models. When it comes to practical application, the level of model detail is chosen based upon the measurement capability of the experiment.

The rotating diatomic will now be further refined while only considering homonuclear molecules.

The full Schrödinger equation will not be solved again; a full mathematical treatment is beyond the scope of this work. The concepts will be introduced, though, so that the reader can understand the model assumptions that give rise to the spectroscopic formulation used later. As before, the goal of the spectroscopist is to obtain the total angular momentum,  $\vec{J}$ , and its associated rotational quantum number.

In the original model, electron motion was completely neglected. If one considers the electrons orbiting the molecule, there will be an additional angular momentum introduced. Although the electrons are comparatively light, their speed makes this component significant. Figure 1.21 shows the effect of the additional vector. The nuclei (in orange) rotate through the plane of the page, leading to the momentum vector  $\vec{R}$ . The individual angular momenta of each electron sum to be  $\vec{L}$ , the total orbital angular momentum. Conceptually, it is easiest to visualize a single electron which represents the sum of collective orbital motion. As this electron rotates about the blue dotted line, the vector component that can couple into the internuclear axis is given by  $\vec{\Lambda}$ . The coupling leads to a shift in molecular motion about the new summation vector,  $\vec{J}$ , which is shown in red. The molecule undergoes precession as it rotates, much like a symmetric, spinning top.

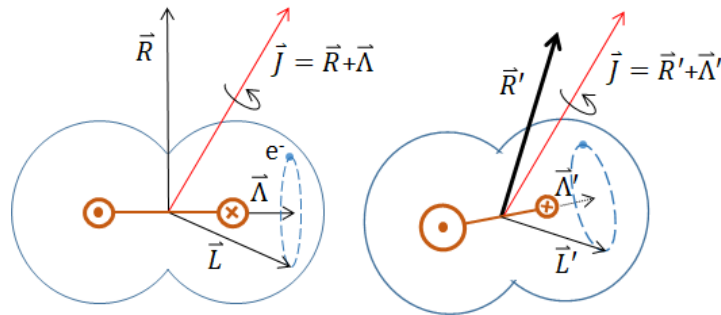


**Figure 1.21** Rotating molecule with identical nuclei (orange) moving in and out of the page as they precess around the constant resulting vector,  $\vec{J}$ . The electron cloud in blue is rotating to give a net angular momentum  $\Lambda$ . The bold and dotted vectors on the right represent directions out of and into the page, respectively.

Finally, electron spin must be considered as well. Spin may couple into the nuclear motion because it is fundamentally a magnetic angular momentum, and the rotating nuclei can generate

their own field as they circulate. The molecular precession becomes more complicated, depending on how the spin couples into the nuclear motion. This was the work of Hund, who reduced the coupling into four limiting cases. The plasma scientist will only encounter cases *a* and *b* the vast majority of the time, and they are relevant to the N<sub>2</sub> band considered here.

The individual electron spins sum to give the vector  $\vec{S}$  shown in Figures 1.22a and 1.22b. In Hund's case *a*, the nuclear rotation is slow relative to the electron orbit and spin. The spin couples strongly to the internuclear axis, and the relevant vector component is given by  $\vec{\Sigma}$ . The orbital angular momentum and spin angular momentum sum together to form  $\vec{\Omega}$ , which adds with nuclear angular momentum again to form  $\vec{J}$ .

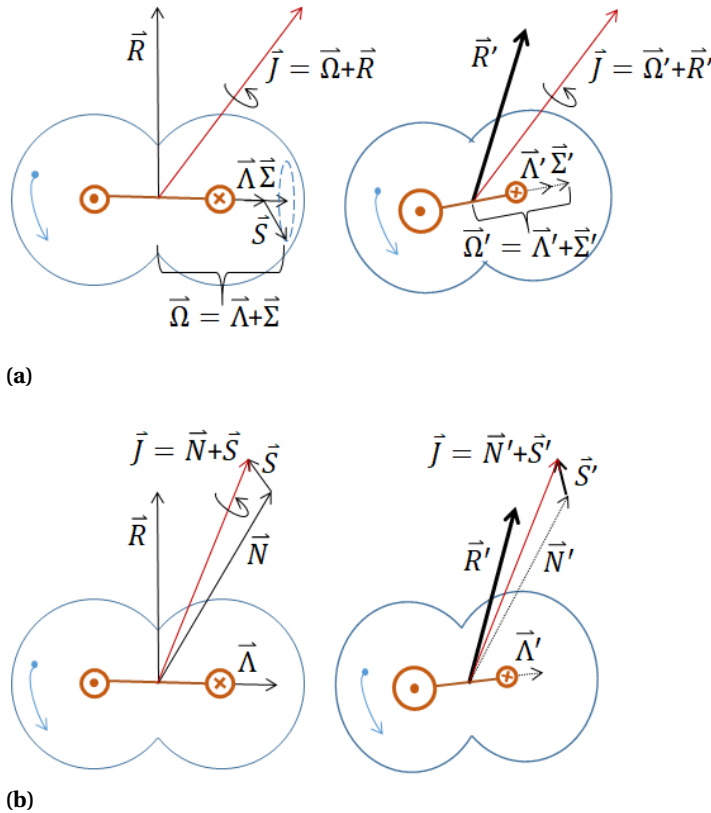


**Figure 1.22** a) Molecular motion in Hund's case *a*, when electron spin couples strongly to the internuclear axis. b) Motion in Hund's case *b*, when spin is not coupled to the axis. In both cases, the molecule precesses about the total angular momentum vector  $\vec{J}$ , which is fixed.

As the molecule rotates more quickly, the spin begins to decouple from the internuclear axis. By analogy, consider the molecule to be a plasma. As the central positive charges spin faster, they generate a magnetic field that will screen out the spin magnetic field. In other words, the electron spin no longer effects the nuclei directly. Rather, the strongly spinning nuclei form a new resultant given by  $\vec{N}$  (or historically,  $\vec{K}$ ). The molecular precession will create a net magnetic field along  $\vec{N}$  which interacts with spin freely, leading to the summation with  $\vec{S}$  rather than its component.

Upon determining the quantum numbers from Schrödinger's equation, the next task is to evaluate the transition probability between the upper and lower states of interest, which will provide an intensity distribution among all the states. The transition moment,  $R$ , is given by

$$R = \int \Psi'^* M \Psi'' d\tau \quad (1.29)$$

The electric dipole moment is represented by  $M$ , for radiation from state  $\Psi'$  to  $\Psi''$ . The asterisk represents the complex conjugate of the wavefunction  $\Psi$ . By again using the Born Oppenheimer approximation, the expression can be split into electronic, vibrational, and rotational components.

$$R = \int \Psi_e'^* \Psi_v'^* \Psi_r' (M_e + M_v + M_r) \Psi_e'' \Psi_v'' \Psi_r'' d\tau \quad (1.30)$$

The integral is separated into components of  $R$ . For example, the vibrational transition moment will provide the Franck-Condon factors ( $q_{v', v''}$ ). The evaluation of Equation 1.30 leads to the selection rules as well; transitions are considered forbidden when the integral evaluates to zero. The line strength term that is of concern for a single rovibrational band is  $S_{J', J''}$ . In practice, the transition between Hund's cases *a* and *b* must be determined cohesively, as an intermediate case. The molecule does not 'snap' from one case to the other at a particular  $J$  number. The rotational line strengths for the intermediate Hund's case were derived by Kovacs [48].

## 1.6 Hairpin Probes

Microwave probes were first presented in 1960 in a transmission configuration [83]. In their experiment, resonant current was measured as a function of swept RF frequency passing through a planar disk antenna. The resonant frequency was shown to correlate to the drive current of the plasma, and linearity with Langmuir probe density was demonstrated as well. A specific microwave probe configuration, the hairpin probe (HP), was later developed by Stenzel [81]. The innovation was motivated by a desire to obtain spatially-resolved electron density measurements in a magnetized plasma. The analysis of Langmuir probe data in the presence of a magnetic field is complicated by the motion of electrons within magnetic field lines; this changes the localized current collection region that is otherwise well characterized [45].

A quarter wavelength transmission line which is shorted at one end and open at the other has a resonant frequency,  $f_r$ , given by

$$f_r = \frac{c}{4l\kappa^{1/2}} \quad (1.31)$$

where  $c$  is the speed of light,  $l$  is the length of the HP tines, and  $\kappa$  is the dielectric constant of the medium containing the probe. In vacuum, the resonant frequency is then  $f_o = c/4l$ . In the presence of a plasma, the dielectric constant is given by [54]

$$\kappa_p = 1 - \frac{f_p^2}{f^2} \quad (1.32)$$

Here,  $f_p$  is the electron plasma frequency. At resonance, the drive frequency  $f$  of the antenna is  $f_r$ . Substituting the plasma dielectric constant into Equation 1.31, we obtain

$$f_r^2 = f_o^2 + f_p^2 \quad (1.33)$$

One can substitute the plasma frequency formulation

$$f_p^2 = \frac{n_e e^2}{2\pi m \epsilon_0} \quad (1.34)$$

and upon rearranging, the following practical formula is derived for the electron density. The frequency terms are in units of GHz.

$$n_e = \frac{f_r^2 - f_o^2}{0.81} [=] 10^{10} \text{ cm}^{-3} \quad (1.35)$$

Much like Orbital Motion Limit theory was developed to improve the accuracy of LP density measurements, the HP formulation was further refined from its original formulation [68, 78]. The goal was to correct for the sheath formation on the surface of the probe, which decreases the local electron density. The HP response to  $n_e$  is spatially dependent in both  $r$  and  $z$  [90]. However, for a conceptual understanding the reader may consider that the HP is measuring the width-averaged density between tines. In that case,  $n_{e,\text{measured}} < n_e$  due to the void of the sheath. A diagram is provided in Figure 1.23. The sheath thickness is given by  $s$ , and is shown in the inset of the figure.

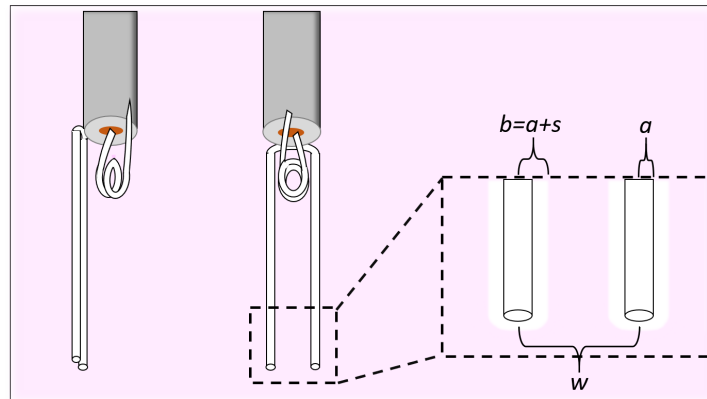


**Figure 1.23** Representation of the HP immersed in a plasma. Sheath formation around the tines will alter their antenna response, as the localized volume contains varying two dielectric materials, the vacuum and the plasma.

A sheath correction factor was proposed for Equation 1.10 [68, 78].

$$f_r^2 = f_o^2 + \xi f_p^2 \quad (1.36)$$

The correction factor,  $\xi$ , was derived by determining the tine capacitance at the end of the transmission line. In other words, the experimental permittivity was assumed to be a combination of vacuum permittivity (the sheath), and unperturbed plasma permittivity. The derivation begins with the capacitance of concentric cylinders from HP tine to the sheath edge.

$$C_{sheath} = \frac{1}{\ln(\frac{b}{a})} \quad (1.37)$$

where  $a$  is the tine radius and  $b$  is the radius of the sheath-plasma boundary. For the next capacitance, a 'wire' of radius  $b$  is treated with a plane midway between the width ( $w$ ) of the HP tines. The capacitance between an infinite wire and a plane is [84]

$$C_{plasma} = \frac{\kappa_p}{\ln(\frac{w}{2b}(1 + \sqrt{1 - \frac{b^2}{w^2/4}}))} \quad (1.38)$$

In practice, the HP is designed so that  $w/2 > b$ , otherwise a depletion region would form within the tines and a true  $n_e$  does not exist within the HP volume. This simplifies Equation 1.13 to

$$C_{plasma} = \frac{\kappa_p}{\ln(\frac{w}{b})} \quad (1.39)$$

The total adjusted capacitance is then the sum of the two capacitances in series.

$$C_T = \frac{\kappa_p}{\kappa_p \ln(\frac{b}{a}) + \ln(\frac{w}{b})} \quad (1.40)$$

The HP measures an effective combined permittivity, which from Equation 1.4 is given by  $\kappa_{eff} = f_o^2/f_r^2$ . Combining this expression with the combined tine/plane capacitance, we acquire

$$C_T = \frac{\kappa_{eff}}{\ln(\frac{w}{a})} \quad (1.41)$$

Equations 1.15 and 1.16 are set equal to each other and the plasma permittivity is solved for. By substituting the permittivity expression in Equation 1.5, the final correction factor is obtained.

$$\xi = 1 - \frac{f_o^2 \ln(b/a)}{f_r^2 \ln(w/a)} \quad (1.42)$$

The formulation was refined by others for the large sheath case, which dropped the simplification to obtain Equation 1.12. It should be noted that it was assumed that the sheath consisted of a single Debye length, so that  $b = \lambda_D + a$  [69]. The expression applicable to the low pressure, collisionless regimes investigated here is [78]

$$\xi = 1 - \frac{f_o^2 [\ln(\frac{w-a}{w-b}) + \ln(\frac{b}{a})]}{f_r^2 \ln(\frac{w-a}{a})} \quad (1.43)$$

Because the Debye length is dependent on  $n_e$ , the corrected electron density must be iteratively solved for.

A critical parameter for this derivation was the sheath thickness. One Debye length is an estimate that is unlikely to apply for all plasma conditions. The issue is addressed in Chapter 2 through the novel use of pulsed plasmas as a diagnostic. The technique allows for a more accurate determination of  $n_e$  without the need for deciding upon a sheath model. However, the sheath correction factor in Equation 1.43 will be used to verify that the results are within the expected bounds of sheath formation on the HP tines. This is not meant to settle the ongoing debate [16, 74] within the plasma community over the size of the plasma sheath, but rather to verify the validity of the experiment.

CHAPTER

2

## HAIRPIN PROBE MEASUREMENTS IN TRANSIENT PLASMA CONDITIONS

Chapter 1 introduced the concept of leveraging transient conditions in a plasma discharge for unique parameter studies. In this chapter, a microwave hairpin probe (HP) is introduced as a density diagnostic that, when combined with designed plasma transients, provides insight into probe analysis and plasma conditions that are not possible in steady state conditions.

### 2.1 Hairpin Probe Challenges

As any perturbing diagnostic probe will, the hairpin probe (HP) creates a localized disturbance in the plasma due to sheath formation. This raises the question, "is the probe measuring the true  $n_e$  or perhaps a reduced sheath density?" Others have developed a correction factor to account for the

sheath depletion region [69, 78]. The formulation for the sheath correction factor is reproduced here from Chapter 1.6. Figure 2.1 illustrates the sheath formed around the probe surface.

$$\xi_s = 1 - \frac{f_o^2}{f_r^2} \frac{[\ln(\frac{w-a}{w-b}) + \ln(\frac{b}{a})]}{\ln(\frac{w-a}{a})} \quad (2.1)$$

The vacuum resonant frequency is  $f_o$  and the plasma resonance is  $f_r$ . The HP tine radius is  $a$ , the width is  $w$ , and the sheath size is given by  $b$ . The tines may be electrically isolated from ground with a dielectric collar, to make a floating HP. The work presented in this chapter is with a grounded probe, which will typically have stronger resonance but at the expense of being more perturbative. The potential between the plasma and the tines is given by the plasma potential ( $V_p$ ) for the grounded case, and the difference between it and the floating potential ( $V_f$ ) in the floating HP case. To create a floating probe, a dielectric collar creates a capacitance between the tines and ground [67].

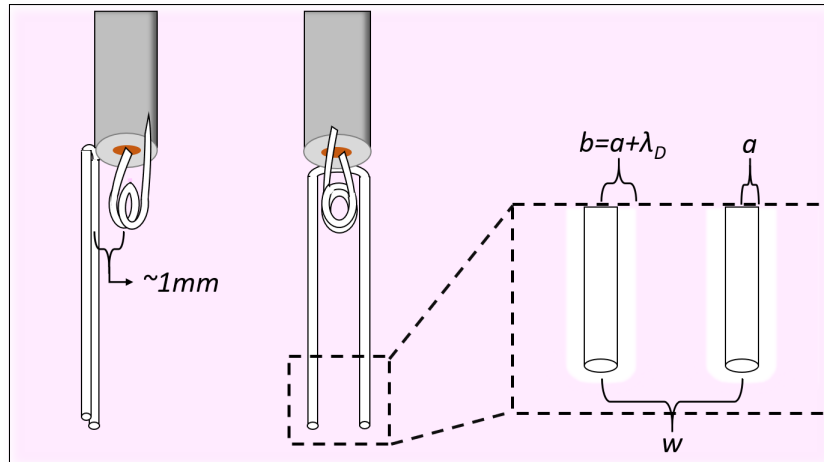


**Figure 2.1** HP within plasma. Inset shows cylindrical sheath between tines with sheath model dimensions.

In a critical work, it was shown that there is still unacceptable uncertainty in HP density measurements [30]. The critique focused on floating probes, but are relevant in the grounded case as well. The key critiques of HPs stem from the uncertainty in the size of the sheath that surrounds the probe. Typically, a Child-Langmuir or Matrix sheath model is used to estimate the sheath size.

The size for each is proportional to the sheath voltage as  $V_s^{3/4}$  and  $V_s^{1/2}$ , respectively. However, both models are valid only in the high voltage regime, when  $V_s \gg T_e$  [54]. This is not always the case in plasma experiments which are typically measuring the bulk plasma, away from the driven high voltage surfaces that these models were developed for. Although  $V_p$  can begin to greatly exceed  $T_e$  under some conditions (namely some capacitive coupled RF configurations), most low temperature plasma conditions will only have a  $V_p$  that is 2 to 10 times  $T_e$ , and thus will not meet the criteria for either of these sheath models. There is an ongoing debate in the plasma community over what defines the sheath edge [16, 54, 74]. Furthermore, even if the high voltage models were applicable, the HP has no way of measuring  $V_s$  or  $T_e$  as a Langmuir probe does. Conceptually, if this were the case then Equation 2.1 could be modified so that  $b = f(V_s, T_e)$ . Then the solution to the corrected  $n_e$  may be iteratively solved for with more accuracy.

Further complications arise from the unknown electron energy distribution function, or EEDF [30]. Both the Matrix and Child-Langmuir models assume a Maxwellian EEDF, which is usually not the case in practical low temperature plasma experiments [28, 29]. The size of the sheath is most sensitive to the high energy electrons, which often depart the most from the Maxwellian distribution of the bulk electrons. Physically, the high energy electrons have a disproportionate effect on sheath size because they are the ones that are able to escape the potential well of the plasma, thereby determining the electron flux that equilibrates with the ion flux. A voltage expression for the floating sheath has been developed to account for this effect [30].

$$V_s = \frac{T_{eh}}{2} \ln\left(\frac{M T_{eh}}{2\pi m_e T_{es}}\right) \quad (2.2)$$

Here  $m_e$  is the electron mass,  $M$  is the ion mass, and  $T_{eh}$  and  $T_{es}$  represent the hot and slow electrons, respectively. The ratio of these temperatures can reach as high as 10 in CCP systems due to stochastic electron heating [28]. For an example of 2 and 20 eV electron populations, the corrected  $V_s$  would be over 250% larger.

The sheath uncertainty is compounded by the spatial sensitivity of the HP antenna. Unlike

Langmuir probes which draw current from a volume larger than the size of the probe/sheath region, the HP has the highest sensitivity in the volume closest to the HP tines [30]. Figure 2.2 illustrates this effect, which was determined from an electromagnetic simulation [90]. In reviewing the literature, this spatial dependence has not been verified either experimentally or by corroborating models. It may be considered another source of uncertainty, then.

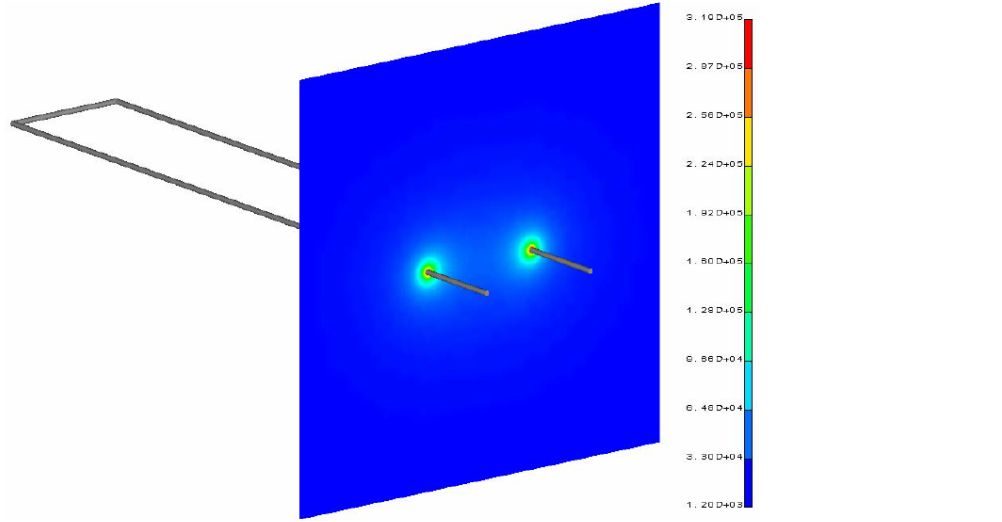


**Figure 2.2** Electric field magnitude in radial plane of HP (V/m). Simulated HP dimensions are  $a=0.065$  mm,  $w=3$  mm and  $l=17$  mm [90].

To summarize the HP challenges thus far, unknown  $V_s$ ,  $T_{eh}$ ,  $T_{es}$ , EEDF, and spatial antenna response all add to the HP uncertainty through sheath contributions. Some have developed a biasing method to address the sheath uncertainty [34, 70]. The idea is that negative bias of the probe with respect to the plasma potential will repel electrons, expanding the sheath and reducing  $f_r$  until it approaches the vacuum frequency. For positive bias, the sheath can be reduced as lower energy electrons are drawn closer to the probe. The resonant frequency in Figure 2.3 clearly exhibits this behavior [70]. The I-V trace plotted on the right axis was used in the standard LP analysis to estimate  $V_p$ . Under the Ar CCP conditions for this example,  $V_p$  was calculated to be 21.3 V. This

is approximately equal to the peak in  $f_r$  at a DC bias of 24.9 V. The authors attributed the offset to the RF component of the sheath. They went on to explain the drop in frequency as the result of increased plasma perturbation when biasing above the plasma potential. Much like a LP, this electron saturation regime will become more perturbative the higher the bias becomes.

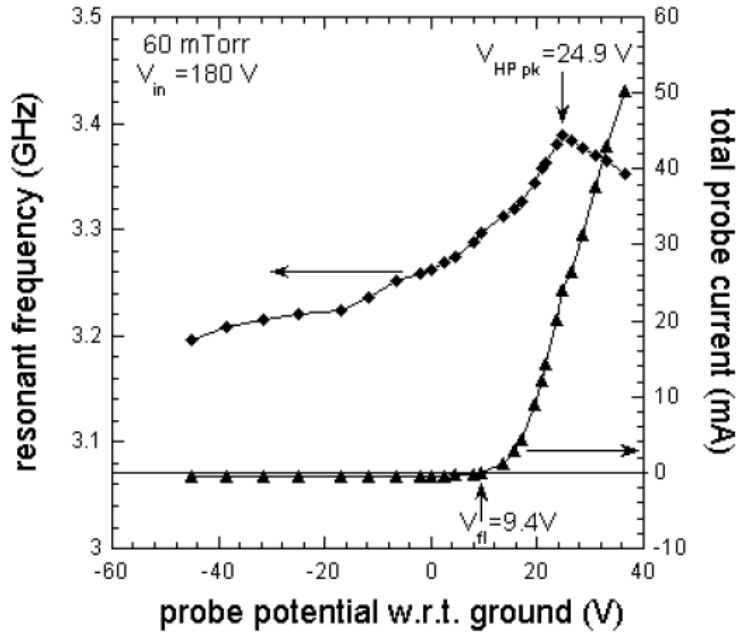


**Figure 2.3** HP resonant frequency (diamonds) and probe current (triangles) versus DC bias.  $f_o=3.115$  GHz and  $V_{in}$  represents the 80 MHz drive voltage of the Ar CCP [70].

The authors went on to compare the DC biased probe to a floating HP that was designed to follow the RF component of the sheath voltage. The same sheath correction factor as Equation 2.1 was used on the floating probe, which uses a Matrix sheath model. The authors claimed excellent agreement between the two values to validate the sheath model on floating probes [70]. These comparisons were made at densities above  $2 \times 10^{10} \text{ cm}^{-3}$ , however. For high density plasmas, the sheath correction will necessarily be small. Regardless of the sheath model one chooses, a more dense plasma will better screen the perturbation of the probe. Furthermore, the authors did not

quantify the errors on their results. In practice, loading the HP circuit with DC biasing reduces  $Q$ , which will increase the relative error.

The effort in this chapter addresses the sheath correction factor that attempts to remedy these uncertainties. The sheath thickness  $s$  was assumed to be one Debye length thick to derive Equation 2.1, yet others have estimated that the floating sheath size may be as much as  $5 k$ , the number of  $\lambda_D$  [15]. Figure 2.4 presents the +/- uncertainty contributions from the  $k$  and  $T_e$  assumptions over several decades of  $n_e$ . Note that this calculation does not include the experimental uncertainty arising from  $Q$ , the resolution in  $f_r$ . The trend is downwards, as expected for the decrease in sheath size with increasing  $n_e$ . An unusual feature is the break in trend at  $1.5 \times 10^9 \text{ cm}^{-3}$  for the  $k$  data. This is because Equation 2.1 begins to provide complex correction factors rather than real solutions. The result could be interpreted as sheath depletion; at lower density the HP is too small to contain the modeled sheaths, or  $2k\lambda_D > w$ . The derivation of the correction factor stemmed from a coaxial capacitor model (see Section 1.6). When this model fails for geometric reasons, so does the circuit model and resulting correction.

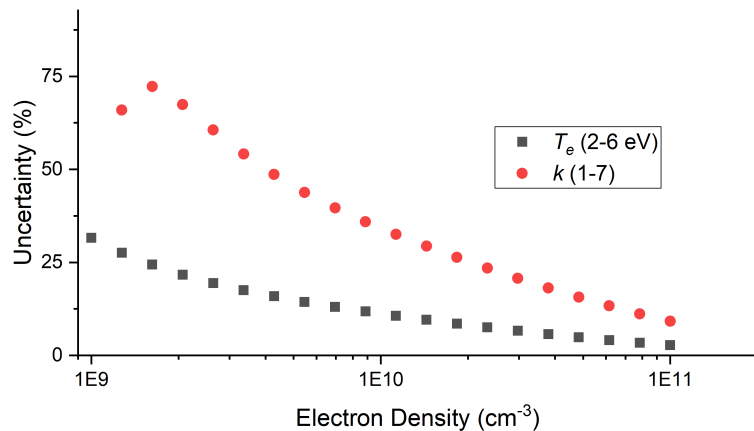


**Figure 2.4** HP relative uncertainty for a range of  $n_e$ . Calculation used HP characteristics  $f_o=2.73$  GHz and  $w=3.85$  mm. For varying  $k$  (red) the temperature was fixed at 4 eV, and for varying  $T_e$  (black),  $k=2$ .

The  $k$  assumption contributes the most to the uncertainty of the HP density correction. In the

experiments discussed here, the probe is grounded and therefore the sheath voltage is  $V_p$ . The plasma potential varies greatly by gas, pressure, and flow conditions for a given plasma source. For the ICP used here,  $V_p$  was as little as 15 V in Ar and as much as 55 V in O<sub>2</sub>. What is needed, then, is a way to experimentally remove the effects contributing to the sheath perturbation. Pulsed plasmas present a solution. In the plasma afterglow, the RF fields on the boundary are lost, and so  $V_p$  drops rapidly as the plasma adjusts to the changing boundary potential. Simultaneously, hot electrons freely diffuse to the boundaries, which reduces  $T_e$  rapidly. Both effects happen within a few  $\mu\text{s}$  [1, 20, 53]. The  $V_p$  drop is equivalent to a  $V_s$  decrease for the case of the grounded HP, and the sheath is then at its smallest size. The plasma afterglow is therefore the minimally perturbed condition for a HP measurement. The key is to demonstrate the link between the pulsed data and the steady state  $n_e$  measurement.

## 2.2 Hairpin Probe Experiment

The plasma experiment is diagrammed in Figure 2.5. A KF25 fitting with SubMiniature A (SMA) electrical feed-through connections provides the HP port into the top of the chamber. The probe is centered both radially and axially within the ICP. The plasma is well confined to the quartz volume due to mesh shielding at the bottom, and measures 5 cm in radius by 15.3 cm in length. The experiment is powered by a 13.56 MHz pulse capable generator (ENI GHW-50). The matching network is a  $\pi$ -type circuit with manual variable capacitors. In each pulsing experiment, power was most matched at the pseudo steady state, or end of the pulse. The data acquisition of the oscilloscope was triggered by the forward power signal from the directional coupler, as this was more stable than the external trigger. Each HP trace of voltage versus time was saved to the PC for automated processing through an in-house Python script (Appendix B), which also controlled the microwave signal generator. The pressure was controlled through a 50 mTorr capacitance manometer that was connected to a throttle valve. The base pressure of the experiment was 6  $\mu\text{Torr}$ , and a leak up rate of 1.5 mTorr/minute ensured clean plasma conditions. Alicat mass flow controllers (MC-100SCCM-D-PCA13) provided inlet gas flow. Industrial grade Ar, He, and O<sub>2</sub> were used.

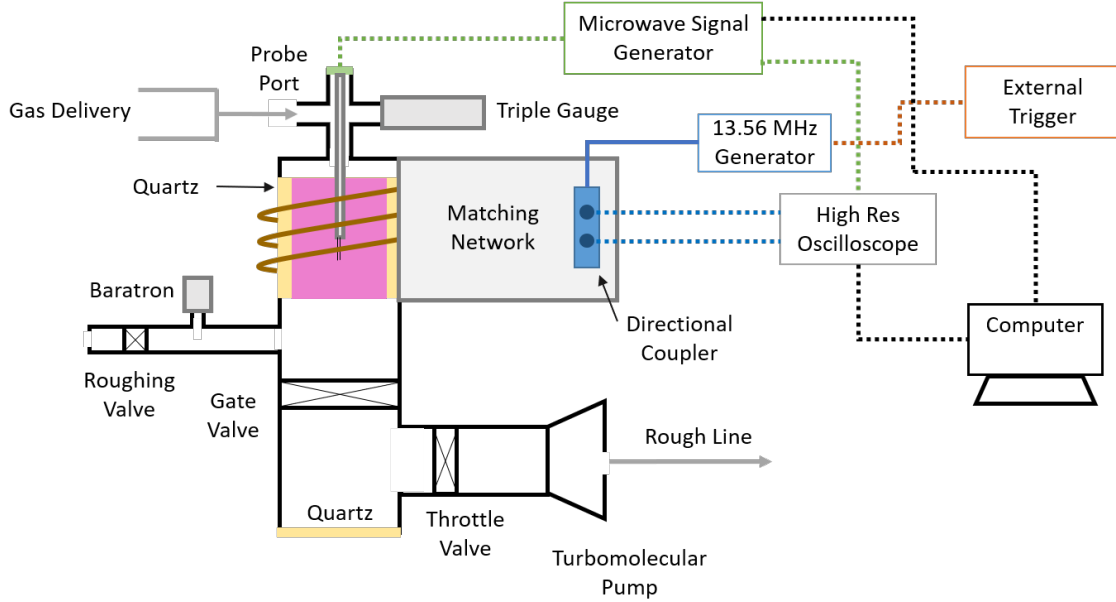


**Figure 2.5** Time resolved HP experiment in an ICP with integrated matching network. Dashed lines represent communications and data signals. The HP antenna was centered both radially and axially.

A diagram of the HP is given in Fig 2.6a. The antenna is made from 22 gauge sterling silver for its high conductivity of GHz frequencies and minimal surface area, which reduces plasma perturbation. The antenna is laser welded to rigid Inconel SMA coaxial cable. In constant wave (CW) plasmas, the HP coaxial cable is connected to a network analyzer, which provides a single port frequency response. The resulting resonance plot is exemplified in Figure 2.6b, where  $f_r$  is found from the  $x$  coordinate of the local minimum.

The performance of the HP is characterized by the Q factor, which is given by the ratio of  $f_r$  to the full width half max (FWHM). A higher Q leads to a reduced uncertainty, which is determined from the expression for the minimum quantifiable frequency shift [81].

$$\Delta f_r = \sqrt{\frac{2f_o^2}{Q}} \quad (2.3)$$

As before,  $f_o$  is the vacuum frequency. The fabrication of the tines determines Q, and the best practices assure that the plane of the tines are parallel to the plane of the coil, as shown in Figure

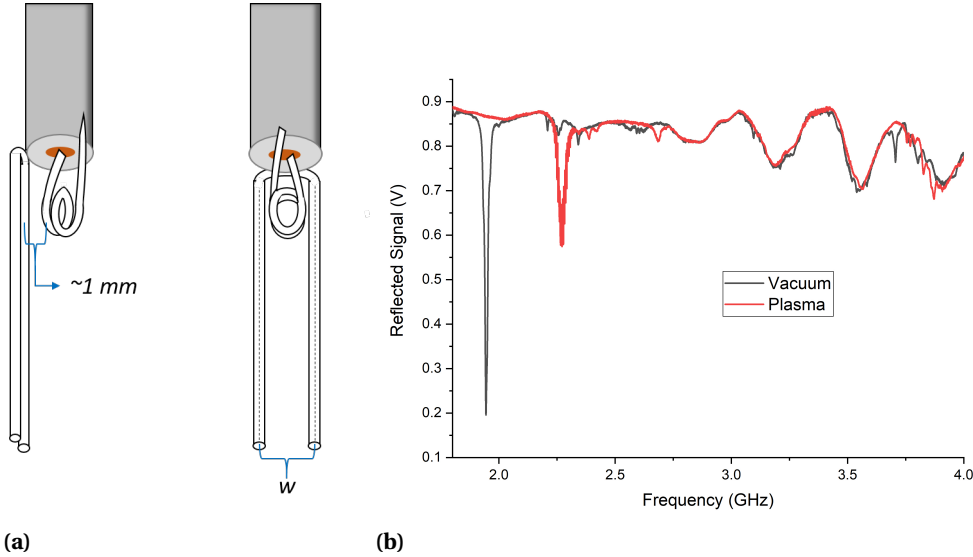


**Figure 2.6** a) HP configuration and b) example vacuum, plasma frequency response.

2.6a. A separation of approximately 1 mm from the coil inductor led to the highest Q at vacuum. The length of the HP tines and the width separating them also effects Q, with tradeoffs between each. For example, a narrower tine width would more strongly couple with the coil antenna. This would raise Q but at the expense of reducing the accurate  $n_e$  measurement range; the sheaths deplete the tine region at low densities that a wider HP could measure. Typically, the fabrication process led to a Q of  $>200$  in vacuum thanks to the craftsmanship of our collaborators [25].

In the measurement of  $n_e$  as a function of time, a boxcar method must be used [41]. Rather than scanning in frequency space, a microwave signal generator (TNI-1002A) sends a fixed frequency into the HP. The reflected signal is directed through a Pasternack circulator (PE8401) and into a Pasternack rectifier, or Schottky diode (PE8016). After being rectified, the DC signal is recorded in an oscilloscope trace, which provides the reflected voltage as a function of time. The signal pathway in Figure 2.7 demonstrates the voltage traces for a fixed frequency. When the resonance in time is recorded as  $f_{r1}(t_1)$ , the next discrete frequency is set as the synthesizer output to provide  $f_{r2}(t_2)$ . Altogether the electronics provide a theoretical time resolution on the order of 5 ns. This limit is not tested here, but 100 ns is more than adequate. Others have experimentally resolved  $n_e$  oscillations

within the RF sinusoid using a similar HP configuration [41].

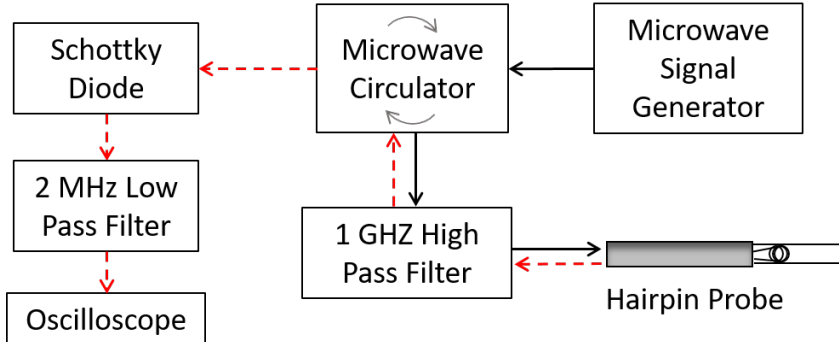
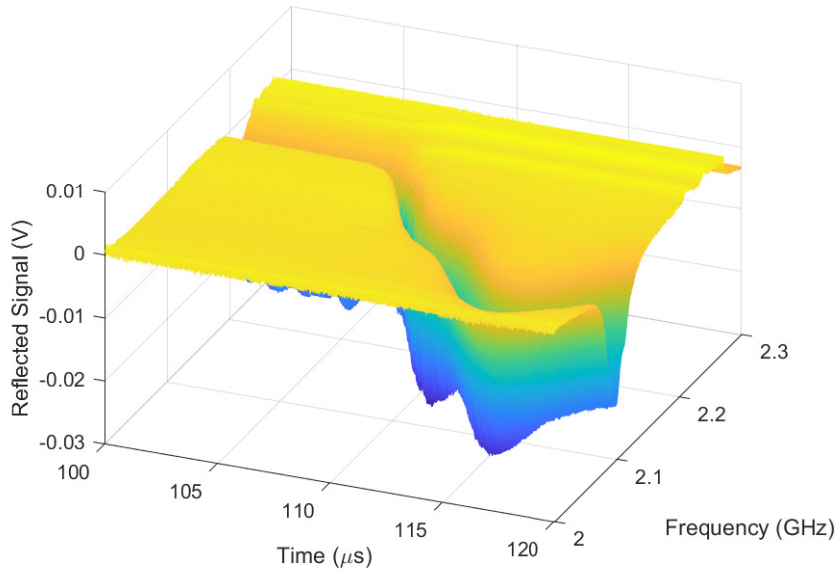


**Figure 2.7** Time resolved HP Configuration. Black arrows represent drive signal, dashed red arrows the reflected measurement signal. Filters were added to reduce stray 13.56MHz noise from the RF generator powering the plasma.

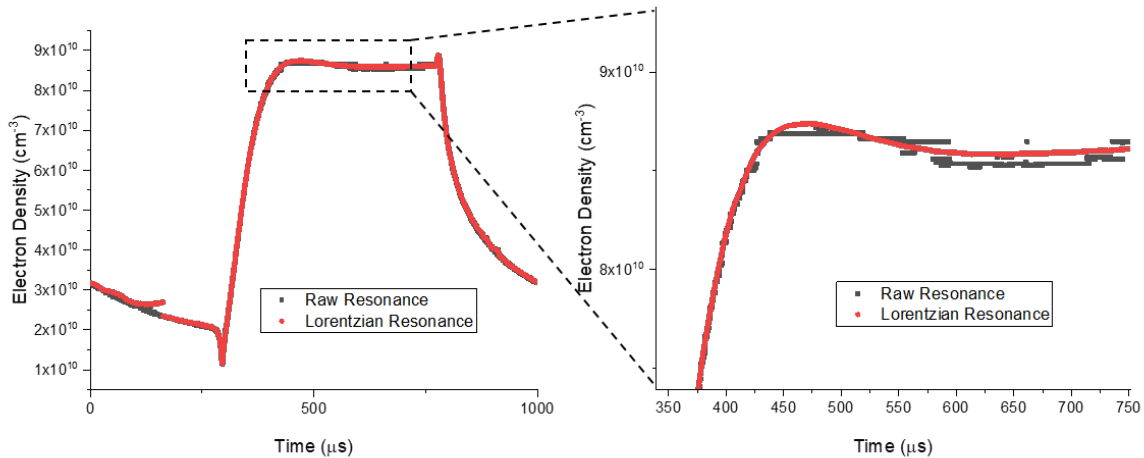
By stepping through in  $f$  and recording the oscilloscope voltage, a three dimensional surface plot is generated for  $V(f, t)$ . Steps of 0.1 MHz were taken, often leading to more than  $10^8$  data points. An example of the three dimensional data is shown in Figure 2.8. An in-house algorithm was written into Python to collect and analyze these data, and it is provided in Appendix B. For a given discrete oscilloscope time  $t_i$ , the minimum  $V(f)$  provides the 'raw'  $f_r$  and subsequent  $n_e$ . Further analysis is performed by fitting the voltage trace at each time with a Lorentz curve, so that  $n_e(t_i)$  is obtained along with the FWHM. As mentioned previously, the FWHM provides the uncertainty in density.

Figure 2.9 shows both the raw time-dependent data and the Lorentzian-fitted density trace within one complete pulse. Both data sets occasionally suffer from discontinuities, as seen at approximately  $200 \mu\text{s}$ . These are caused by discontinuities in the synthesizer  $V(f)$  output, and those frequency regions were avoided in further data sets. For the remainder of this work, only the fitted data will be presented, as it was more continuous.

The signal acquisition is calibrated against background as well. When recalling Figure 2.6b, one can see undesirable resonances, or transmission line effects in  $V(f)$  for  $f \neq f_r$ . These are attributed to the antenna coupling to chamber features, and must be subtracted out in order to be confident



**Figure 2.8** Voltage trace in time and HP frequency. Blue reflects  $f_r$ . The oscilloscope was triggered off of the forward power, which provided more stability than the external trigger. The surface shown would translate into a  $n_e(t)$  trace that is initially flat, then begins to decrease at approximately  $110 \mu\text{s}$ .



**Figure 2.9** Raw and Lorentz-fitted data for one complete pulsed. Power was delivered in 20 W, 1 kHz pulses at 50% duty cycle in Argon.

of the true  $f_r$ . This is done by first recording a reference curve,  $V_{ref}(f)$ , in vacuum. The reference voltage is then subtracted from the  $V(f, t)$  plasma data prior to Lorentzian fitting. It should be noted

that  $V_{ref}(f)$  is unique to each HP and even to a single HP/chamber system. Orientation of the HP within the plasma experiment matters as well. Therefore, a reference signal was acquired each time a HP was placed within the chamber.

## 2.3 Results and Discussion

The pulsed plasma  $n_e(t)$  result is given in Figure 2.10, which provides a demonstrative example of the hairpin spike, or HS. The data acquisition window has been zoomed in to the time domain containing the HS. The  $n_e$  trace is initially flat, which shows that a pseudo steady state has been reached. When the plasma is turned off at  $10 \mu s$ , the sheath collapses and the HP measures a sharp increase resonant frequency, consistent with the trends observed for increasing electron density. For a conceptual approximation, one may consider that the HP is measuring a line-averaged  $n_e$  between the tines. As the plasma turns off and fills the void formally occupied by the electron depleted sheath,  $n_e$  will increase provided that the collapse is faster than the loss of bulk electrons to the walls. A typical  $n_e$  decay is then seen following the sheath collapse. Error bars are obtained for every individual data point through Equation 2.3, but selected errors at  $1 \mu s$  and the peak of the HS are provided for visual clarity. These represent 5.7% and 3.2% relative errors, respectively.

The validity of the HS as an unperturbed  $n_e$  measurement hinges on the relative rates of sheath collapse and bulk electron loss. Conceptually, if the electron density decays much faster than the removal of the sheath, then the pulsed plasma experiment has removed the sheath perturbation at the expense of altering the density too significantly. In that case the diagnostic has simply traded one unknown perturbation for another. To evaluate the validity, a single exponential decay is fit to the data following the HS, and then the after glow density is projected back in time to when  $P_{RF} = 0$ . The resulting curve is shown as the blue line in Figure 2.10. One can see that the ratio of the projected density and spike density is 1.09. If the density decay were significantly faster than the sheath collapse, a HS would not be evident, or the projection would lead to a much larger offset than 1.09. Therefore, assuming that the HS shape is determined solely by the balance between the sheath collapse and bulk density drop, the rate of decay for perturbation effects is faster than the

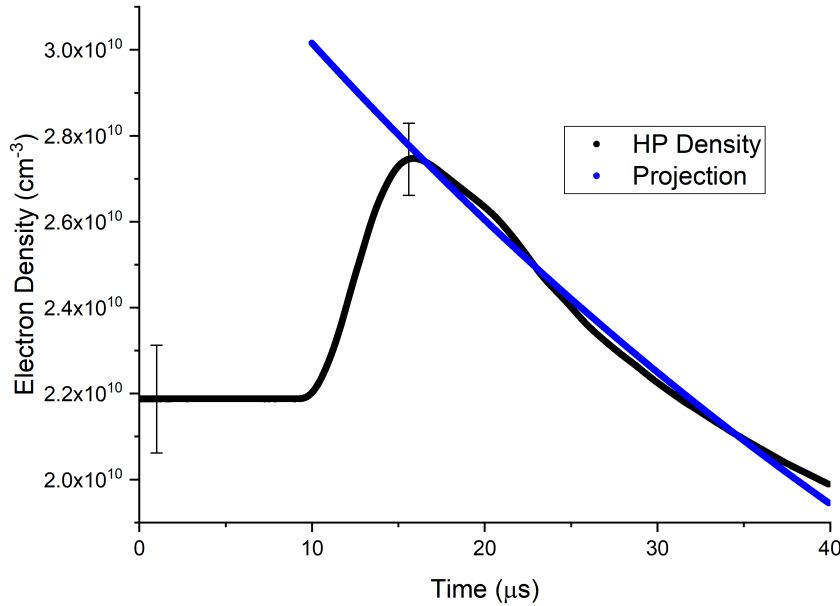


**Figure 2.10** Hairpin spike of 10W pulsed at 500 Hz, 80% duty cycle. Power shuts off at  $10 \mu\text{s}$ . Black data points are for the HP measurement, and the blue projection is an exponential fit of the HS maximum, onward.

rate of electron density decay.

$$k_{per} > k_{density} \quad (2.4)$$

For the example data given above,  $k_{density}=0.0142 \mu\text{s}^{-1}$  and  $k_{per}=0.053 \mu\text{s}^{-1}$ . The perturbation rate constant was determined from a separate exponential fit to the rise in the HS (not shown).

Before proceeding, there are alternative explanations for the HS that should be addressed. In Ar, metastable-metastable collisions are known to generate electrons in the plasma afterglow [64]. Also, it is possible that  $V_{RF}$  is unstable in the shutoff; a generator overvoltage could cause a bulk density increase. Figures 2.11a and 2.11b address both of these concerns [25]. A VI probe was placed at the ends of the ICP coil, which provided the blue voltage trace. For this scale, the 13.56 MHz waveform appears as a solid block. The forward power drops to zero within  $5 \mu\text{s}$  of the generator shutoff at  $10 \mu\text{s}$ , yet the  $n_e$  continues to rise. This eliminates generator instabilities as a possible HS explanation.

For the He comparison, the power was increased to obtain equivalent steady state  $n_e$  as the

Ar trace. A HS of similar magnitude was detected prior to the large metastable pooling peak at 80  $\mu$ s. There are missing data points during the rise, which are the result of Lorentz fits that failed to converge. The shape and timing of the secondary peak is similar to the results for He afterglow production peaks in the literature [65]. Generally, metastable production in the afterglow will reach a maximum in the 50 to 200  $\mu$ s range, not the 10  $\mu$ s scale of the HS. Taken together, it is readily apparent that generator and metastable effects are not contributing to the HS.

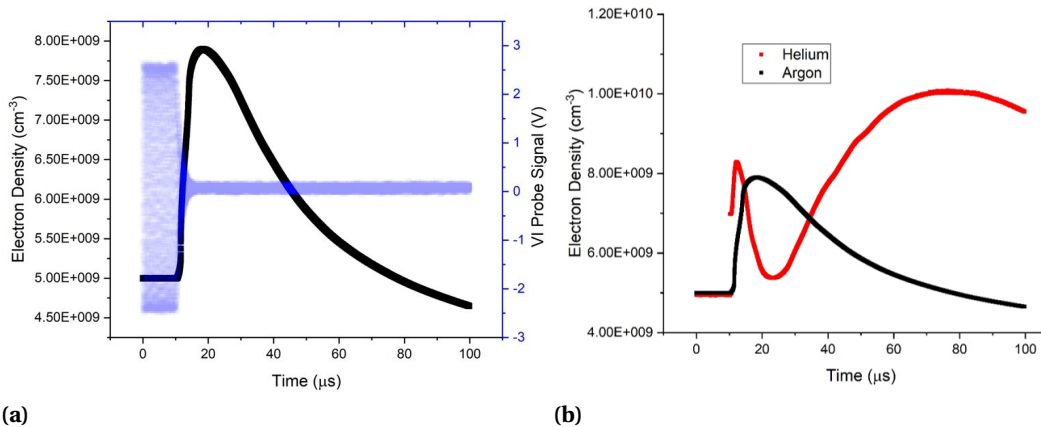


**Figure 2.11** a) VI probe (blue) and HS trace (black) for 10 W pulsed at 1 kHz and 80% duty cycle in a 20 mTorr Ar discharge. b) Same plasma conditions compared to a He discharge, for which the power was increased to 16 W to sustain a similar steady state  $n_e$  [25].

With a perturbation diagnostic in hand, the sheath correction factor can be reconsidered. The HS density is compared to the pseudo steady state density  $n_{e,ss}$ .

$$n_{e,HS} = \xi_m n_{e,ss} \quad (2.5)$$

where  $\xi_m$  is the modified sheath correction factor. Rather than assuming a single  $\lambda_D$  is the sheath thickness, the number of Debye lengths,  $k$ , is determined by varying the parameter until the equivalence in Equation 2.5 is true.

The results for  $k$  across a variety of powers in an Ar ICP are given in Figure 2.12. The error in  $k$  is

calculated from the corresponding Q and uncertainties for both  $n_{e,ss}$  and  $n_{e,HS}$ . The calculation is performed for the high limits of the HS and steady state densities together, then the low error limits of  $n_{e,ss}$  and  $n_{e,HS}$ . This approach avoids the possible crossing of the high/low errors of  $n_{e,ss}$  and  $n_{e,HS}$ , which leads to unrealistic error limits such as imaginary  $k$ .

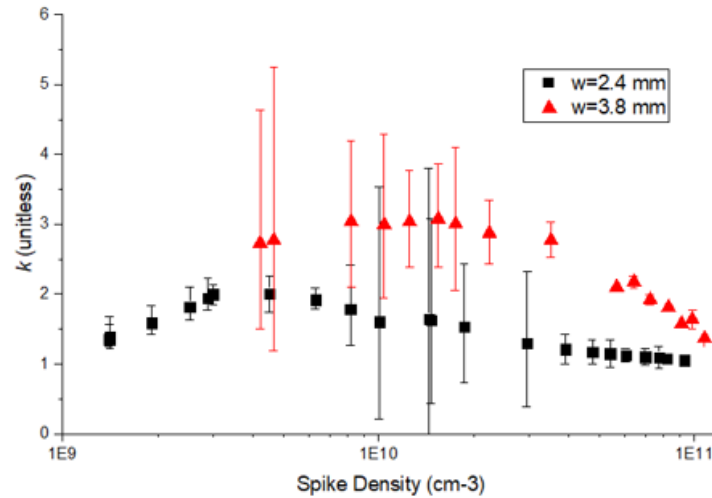


**Figure 2.12** Number of Debye lengths necessary to correct  $n_{e,ss}$  up to the HS density for two HP widths. Plasma conditions: 10 mTorr Ar, 3 sccm. Power pulsed at 500 Hz and 80% duty cycle [25].

The value for  $k$  departs significantly from  $k = 1$  in the low density regime, which is expected considering that the ICP is driven more strongly in capacitive coupling mode at low power settings. This raises  $V_p$ , which has been confirmed by the LP measurements shown in Figure 2.13. The LP data was taken under the same conditions but in CW mode. Although in principal the LP should measure a density spike as well, the time resolution of the available LP is too low to resolve the sheath collapse. The E-H transition in the ICP can be estimated to be at 8 W under these conditions, which corresponds to the peak in  $V_p$ . The data was used to calculate the Matrix Sheath size in Figure 2.14.

It is apparent that the HS provides a new consideration for HP design. It was acknowledged before that the sheath contribution to the HP width should be minimized [82], but the HS provides

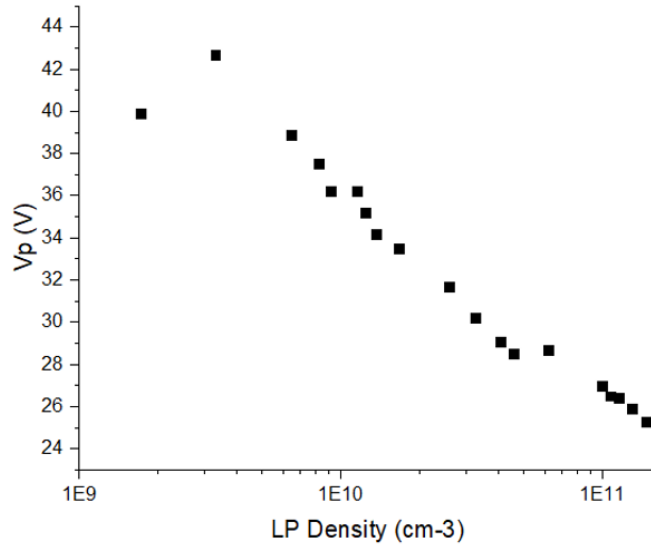


**Figure 2.13** Plasma potential acquired from LP under constant power conditions in 10 mTorr Ar [25].

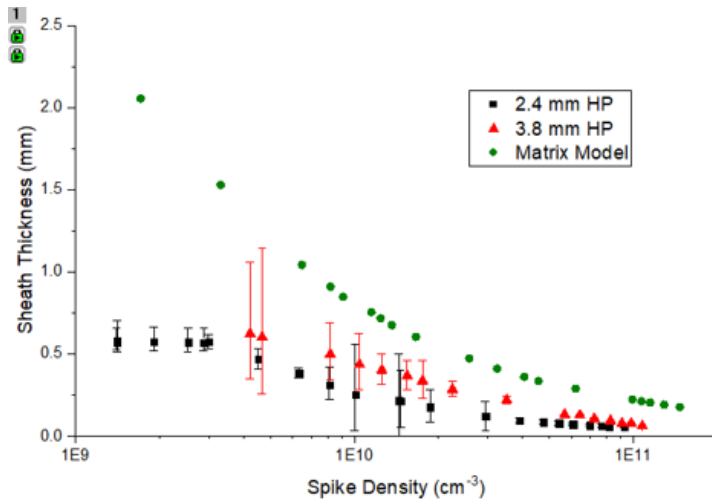


**Figure 2.14** Sheath size calculated from  $k\lambda_D$  for the HP, and from the Matrix model for the LP data [25].

a way of quantifying whether a particular HP geometry is suitable for a particular plasma regime.

In this chapter it was shown that a hairpin resonator probe with sufficient time resolution can measure the dynamics of sheath collapse around the immersed probe in the afterglow of a pulsed RF discharge. This allows for direct perturbation correction for the hairpin probe to account for the surrounding sheath, and removes the requirement that a sheath model be employed for a sheath

correction factor. In the next chapter, a time resolved gas temperature diagnostic will be presented.

## CHAPTER

# 3

# TIME RESOLVED ROTATIONAL TEMPERATURE MEASUREMENTS

This chapter provides the simulation approach and experimental results for determining  $T_r(t)$  from the spectra of the  $C^3\Pi_u$  to  $B^3\Pi_g$  transition of N<sub>2</sub>. The greatest challenge for developing the diagnostic lies in the spectral simulation. Due to the difficulty in compiling these formula from partial explanations in the literature, the first section provides a comprehensive guide to the practical formulas needed. Selected computations are provided as well for those interested in reproducing the diagnostic for this particular rotational band. The next section provides experimental results and a discussion of how best to utilize  $T_r(t)$  data for pulsed plasmas. An explanation is included for the experimental approach to minimizing uncertainty in these low signal to noise situations.

### 3.1 Rotational Temperature Simulation

The practical formulae for modeling the (0-0) vibrational band of the second positive N<sub>2</sub> system are given here. For the reader interested in an introduction to the theory underlying these expressions, refer to Chapter 1.5. One begins by determining the term values ( $F$ ) of the C<sup>3</sup> $\Pi_u$  and B<sup>3</sup> $\Pi_g$  states. Many use the formulation given by Dunham's coefficients [2, 32, 94]. However, this formulation is inadequate for the resolution provided by the Echelle 4000+ spectrometer used in the experiments that follow. The resolution is typically 30 pm, which necessitates more detail in the energy levels of the upper and lower states, both of which are triplets. The formulas developed by Budo [13] are reproduced in English in [36] and [38] for such a case.

$$\begin{aligned} F_1(J) &= B_\nu[J(J+1) - \sqrt{Z_1} - 2\sqrt{Z_2}] - D_\nu(J - \frac{1}{2})^4 \\ F_2(J) &= B_\nu[J(J+1) + 4Z_2] - D_\nu(J + \frac{1}{2})^4 \\ F_3(J) &= B_\nu[J(J+1) + \sqrt{Z_1} - 2\sqrt{Z_2}] - D_\nu(J + \frac{3}{2})^4 \end{aligned} \quad (3.1)$$

where  $Z_1$  and  $Z_2$  are defined by

$$\begin{aligned} Z_1 &= \Lambda^2 Y(Y-4) + \frac{4}{3} + 4J(J+1) \\ Z_2 &= \frac{1}{3Z_1} [\Lambda^2 Y(Y-1) - \frac{4}{9} - 2J(J+1)] \end{aligned} \quad (3.2)$$

and  $Y$  is given by the ratio of molecular constants  $A/B_\nu$ . This characterizes the amount of coupling between the electron spin and the angular momentum of the internuclear axis. The  $Y$  parameter determines whether the upper and lower states are well-represented by Hund's case *a* or *b*, *individually*. Therefore it is possible to have (*a-a*) or (*a-b*) transitions. Most accurately, the (C<sup>3</sup> $\Pi_u$ -B<sup>3</sup> $\Pi_g$ ) system transitions between case *a* and *b* as  $J$  increases, at approximately  $J = 4-6$  [94, 95].

The term formulas in Equation 3.1 are used to calculate the rotational component,  $\nu_r$ , of the total measured electronic and rovibrational transition. Each triplet can transition to the same-numbered

lower triplet in the following main branches.

$$\begin{aligned}
 {}^3\Pi_o - {}^3\Pi_o : & \left\{ \begin{array}{l} P_1 : \nu_r(J) = F'_1(J-1) - F''_1(J) \\ R_1 : \nu_r(J) = F'_1(J+1) - F''_1(J) \end{array} \right. \\
 {}^3\Pi_1 - {}^3\Pi_1 : & \left\{ \begin{array}{l} P_2 : \nu_r(J) = F'_2(J-1) - F''_2(J) \\ Q_2 : \nu_r(J) = F'_2(J) - F''_2(J) \\ R_2 : \nu_r(J) = F'_2(J+1) - F''_2(J) \end{array} \right. \\
 {}^3\Pi_2 - {}^3\Pi_2 : & \left\{ \begin{array}{l} P_3 : \nu_r(J) = F'_3(J-1) - F''_3(J) \\ Q_3 : \nu_r(J) = F'_3(J) - F''_3(J) \\ R_3 : \nu_r(J) = F'_3(J+1) - F''_3(J) \end{array} \right. 
 \end{aligned} \tag{3.3}$$

Note that the  $J$  limits will be restricted in each case, depending on the way the researcher chooses to implement their code. Here,  $J$  up to 40 was simulated in MATLAB (Appendix A). It was found that higher  $J$  values were important for the spectral region between the  $P$  and  $R$  branches. The simplest way to represent the whole transition is

$$\begin{aligned}
 \nu(J', J'') &= \nu_e + \nu_v + \nu_r(J', J'') \\
 \nu(J', J'') &= \nu_o + \nu_r(J', J'')
 \end{aligned} \tag{3.4}$$

Colloquially, the *band origin* is  $\nu_o$  while the *system origin* is given by  $\nu_e$  [61]. The system origin is relative to all the possible  $(\nu' - \nu'')$  and  $(J' - J'')$  transitions while the band origin gives the bandhead for the specific (0-0) rotational spectrum discussed here. The  $N_2$  constants are provided in Table 3.1.

Upon calculating the wavenumber, the intensity distribution was next calculated.

$$I_{J', J''} = \frac{G q_{0,0} S_{J', J''} e^{-F_{J'} h c / k_b T_r}}{\lambda_{J', J''}^4} \tag{3.5}$$

The constants  $h, c, k_b$  represent Planck's constant, the speed of light, and Boltzmann's constant, respectively. The Franck-Condon factor  $q_{0,0}$  is provided in Table 3.1, and  $G$  represents an arbitrary scaling factor to match the intensity of the experiment. Line strength factors  $S_{J', J''}$  were obtained

**Table 3.1** Rovibrational constants for the second positive N<sub>2</sub> system.

Parameter [units]	C <sup>3</sup> Π <sub>u</sub>	B <sup>3</sup> Π <sub>g</sub>	Reference
B <sub>v</sub> [cm <sup>-1</sup> ]	1.8153	1.62872	[76]
A [cm <sup>-1</sup> ]	39.134	42.234	[76]
D <sub>v</sub> [cm <sup>-1</sup> ]	5.95x10 <sup>-5</sup>	5.81x10 <sup>-5</sup>	[76]
q <sub>0,0</sub> [unitless]	0.4515	N/A	[52]
v <sub>o</sub> [cm <sup>-1</sup> ]	29670.942	N/A	[76]

from p. 132 of [49], or more easily reproduced for the  $\Lambda = 1$  case in [48]. They are too lengthy to present here, but the reader is advised to refer to [61] in order to understand the notation provided by Kovacs. For example,  $P_1$  refers to a  $\Delta J = -1$  transition between the 1st triplets of the  $C$  and  $B$  states, when  $\Omega = 0$ . As mentioned before, the (0-0) rovibrational band transitions between Hund's cases. Therefore the intermediate case,  ${}^3\Pi(int) - {}^3\Pi(int)$ , was simulated.

The intermediate case line strengths are plotted in Figure 3.1a. To illustrate the variation between the Kovacs formulation and simply assuming Hund's case a, the relative difference between line strengths is plotted in Figure 3.1b. The stem plot in Figure 3.1c shows the results of Equation 3.5, before line broadening has been taken into account. The purpose is to show that the P and R branches are the main determinants of the fitting procedure. It is clear that Kovacs' intermediate formulation will lead to a significantly altered simulation result. When the lines are broadened to simulate the experiment, the simpler case a will have more discrepancy against the experimental data.

To broaden the lines, a Gaussian function was fit to each  $I(J', J'')$  in Figure 3.1c. Then for a particular wavelength all of the resulting Gaussians were summed. Arithmetically, it is represented by

$$I_m = \sum_{n=1}^N \frac{I_n e^{\frac{-E_n}{T_r}} e^{-\frac{(x_m - \lambda_n)^2}{2\sigma^2}}}{\sqrt{2\pi\sigma^2}} \quad (3.6)$$

The FWHM from the measurement of a reference lamp is used to determine the standard deviation of the broadening function. The indices  $N$  and  $M$  represent the total number of lines in

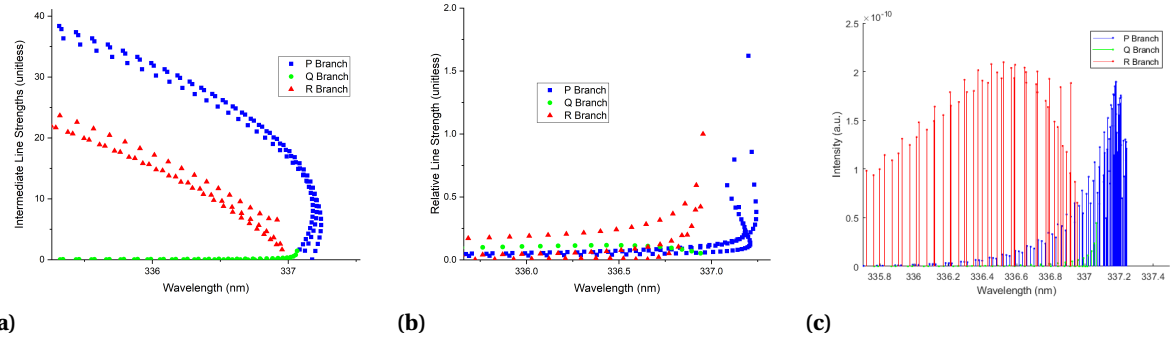


**Figure 3.1** a)  $S_{J',J''}$  values for Hund's intermediate case formulation. b) Relative difference in line strengths between intermediate and Hund's case  $a$  simulations. c) Intensity distribution with 'infinite resolution' for line strengths from Hund's intermediate case and example  $T_r$  of 450 K.

Equation 3.6 and the total number of data points in the experiment, respectively. In practice,  $I_n$  does not differ from  $I_{J',J''}$  in Equation 3.5, the former is simply a vector containing all 8 rotational branches. For a more highly sampled simulation, the value for  $M$  was made ten times larger than the experimental data set. Then interpolation allowed for determining the difference between the simulation and experimental intensities at each discrete wavelength. The best fit was found by minimizing the chi-squared test when stepping through in a range of  $T_r$ .

$$\chi^2 = \sum_{i=1}^{M_{ex}} \frac{(I_m - I_{ex,m})^2}{\sigma_{ex,m}^2} \quad (3.7)$$

The subscript  $ex$  indicates the experimental values, and the experimental standard deviation of each data point was determined by taking four acquisitions. The  $\chi^2$ -squared test is more accurate than least squares (also known as Pearson's test) because it weighs each difference according to the confidence of the corresponding experimental data point. An optimal fit is presented in Figure 3.2. Certain features are important to note. The alignment was obtained by shifting the maximum of the simulated intensity to coincide with the experimental maximum, and both the simulated and experimental intensities have been normalized to their respective maxima. The line doubling in the shorter wavelengths was only possible to simulate with the term formulas in Equation 3.1 and the intermediate line strengths provided by Kovacs [48].

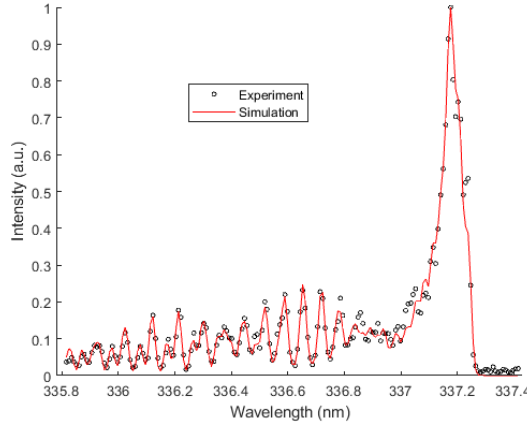


**Figure 3.2** Simulation comparison with experiment for pure nitrogen. Conditions were 100 W and 50 mTorr. Best fit obtained for  $T_r=445\text{K}\pm14\text{K}$ .

The uncertainty in the temperature measurement arises from two sources: experimental and simulation error. These are added in quadrature to give the overall uncertainty. The simulation error is determined from the Monte Carlo bootstrap method [71]. Put simply, the best fit of the simulation is found for multiple experimental data sets and the standard deviation is acquired from those results. It is a brute force method that has high computational demand, but it is easy to understand and implement. The  $\chi^2$  statistic, though useful for residual error minimization, is inaccurate for determining the simulation standard deviation in nonlinear cases such as this [71]. The experimental error is found from the average standard deviations of the individual  $I_M$ , which necessitated experimental replicates.

### 3.2 Time Resolved Temperature Results

The experimental setup for time resolved acquisitions is shown in Figure 3.3. An Echelle 4000+ spectrometer was gated by an external trigger that also controlled the 13.56 MHz source, an Advanced Energy Cesar generator. The signal was increased by approximately 10% when light from the ICP was focused with a lens into the optical fiber.

The steady state simulation in Figure 3.2 had a small relative error of 3%. However, the time

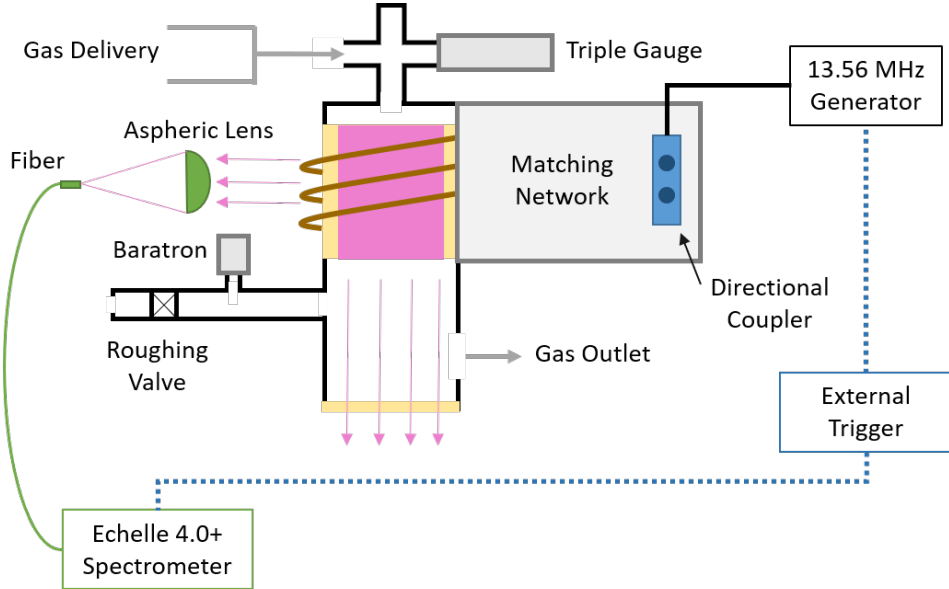


**Figure 3.3** Experiment for determining  $T_r(t)$  in ICAROS. N<sub>2</sub> was added as 5% of total gas composition for O<sub>2</sub>/N<sub>2</sub> pulsing experiments. Plasma conditions were 50 mTorr and 200 W, with on cycle periods lasting for 1 or 10 ms.

resolved case led to significantly more uncertainty. This  $T_r(t)$  diagnostic was developed for small N<sub>2</sub> admixtures for an O<sub>2</sub> plasma in PIF experiments (Chapter 4), and so the signal to noise ratio is greatly reduced. The  $T_r(t)$  effort was made to improve the uncertainty in the PIF diagnostic, and so experimental and simulation error were rigorously quantified. The need for short gate windows led to single acquisition spectra like those shown in Figure 3.4. Two unique data sets are shown, both of which were reference-subtracted. One can see that approximately six individual rotational transitions are detected for the first acquisition, and the 150th acquisition observed 11 transitions. Furthermore, the reference signal that had been subtracted was 2950 counts, with some variation. This highlights the inherently noisy challenge posed by  $T_r(t)$  measurements. A tradeoff between acquisition time, signal to noise ratio, and experimental uncertainty led to a gain of 3000x being used with 200  $\mu$ s gate widths accumulated across 100 pulses. Those data acquisitions were repeated 100 times and averaged in sets of 25 in order to obtain a relatively stable signal.

To determine the experimental error, standard deviations were determined for the averaged signals as well as the averaged references. These were added in quadrature to obtain a wavelength

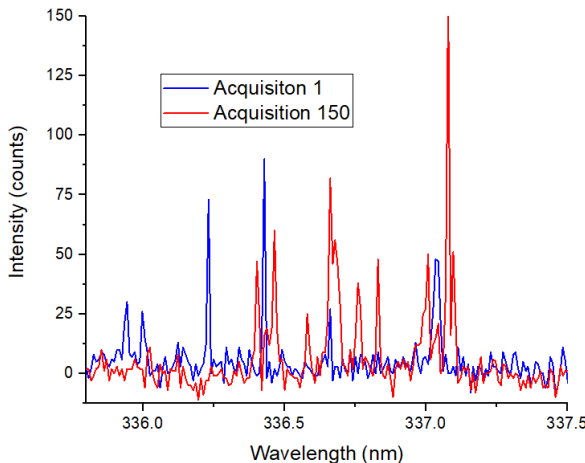


**Figure 3.4** Two single pulse acquisitions for a 50 mTorr  $\text{N}_2/\text{O}_2$  mixture pulsed at 20 Hz and 200 W. Gain was 3200, and the data represents the [400,600]  $\mu\text{s}$  window after power on.

dependent error plot shown in Figure 3.5a. One can see that there is a steady decrease in experimental uncertainty towards the 337.1 nm region. This is where the peak of the rotational bandhead is in Figure 3.5b; it represents the most P branch lines stacked upon each other as in Figure 3.1c. That is why it has reduced uncertainty compared to the sole triplets in the lower wavelengths. Fewer emission events will inherently be more stochastic.

To obtain the simulation error, the Monte Carlo bootstrap method was applied. Procedurally, the four signals and four references were subtracted from each other randomly to form ten experimental spectra. These bootstrapped spectra were then simulated to obtain ten  $T_r$  results. The overall analysis process is shown graphically in Figure 3.6. Note that repeated bootstrap spectra are acceptable. From statistical theory, bootstrapping will lead to the true population variance as large numbers of synthetic populations are developed [71]. In the case here, insignificant decreases in simulation error were found beyond ten results.

An example of the unique  $T_r$  results across the ten synthetic spectra is shown in Figure 3.7b. A sufficiently small step size for  $\Delta T_r$  must be used. Here, 2 K was a fine enough step size for the  $T_r$  fit trials of Equation 3.6. One can see that a larger step size of 50 K may lead to all the simulations converging at 350 K. This would clearly underestimate the simulation standard deviation. An example

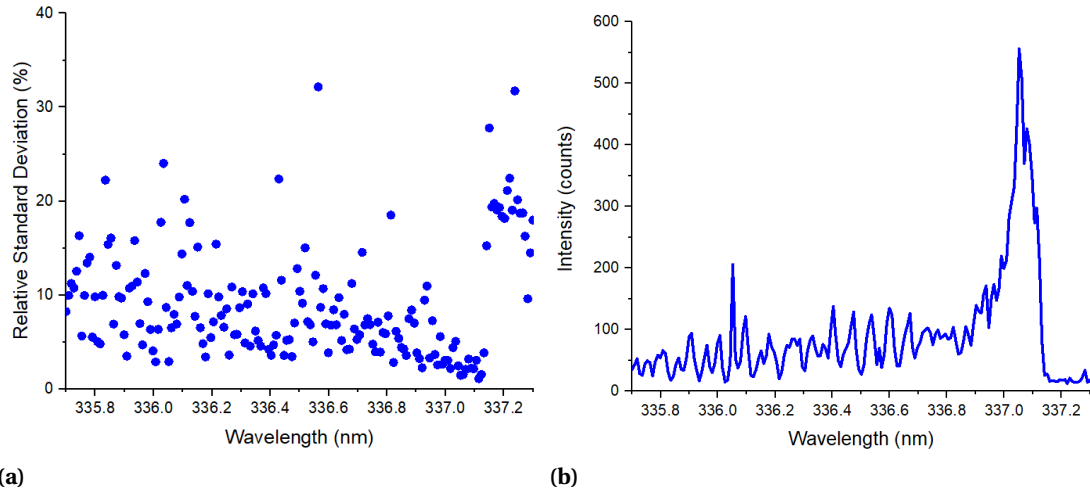


**Figure 3.5** a) Experimental relative error as a function of wavelength for the spectrum shown in b). Data set was obtained for 10 ms into the on cycle of a 200 W, 50 mTorr pulse with 5% N<sub>2</sub>.

least squares minimization is shown in Figure 3.7a. The simulation error was obtained from the standard deviation of the ten bootstrap  $T_r$  results, and the overall error was calculated from the quadratic sum of the simulation and experimental error. In most cases, the experimental error dominated.

An example  $T_r(t)$  is shown in Figure 3.8a. One can see an increase in temperature as the on cycle continues from  $t = 0$ , as expected. The relative errors grew somewhat as the temperature increased, from 6% to 9%. This was likely the result of gas expansion; heating led to fewer targets for the electron excitation of the ground state N<sub>2</sub> into the upper C<sup>3</sup>Π<sub>u</sub> state. Figure 3.8b validates this conclusion. The raw signal was greater at the start of the pulse than at the end. One should also consider the minor differences found between the 0.5 and 10 ms spectra. It is difficult to visually judge a change in overall shape of the spectra, even though the  $T_r$  difference is 168 K. This highlights one drawback to  $T_r$  measurements; the user is entirely dependent on the goodness of the simulation, without the aid of visual inspection.

The  $T_r(t)$  results were compiled in two ways: unique curves and projected traces. The goal of the time resolved temperature was to obtain accurate on *and off cycle* behavior. It was necessary to fit a projection to the curves, as a 10  $\mu$ s time resolution was required for the PIF experiment in Chapter 4.

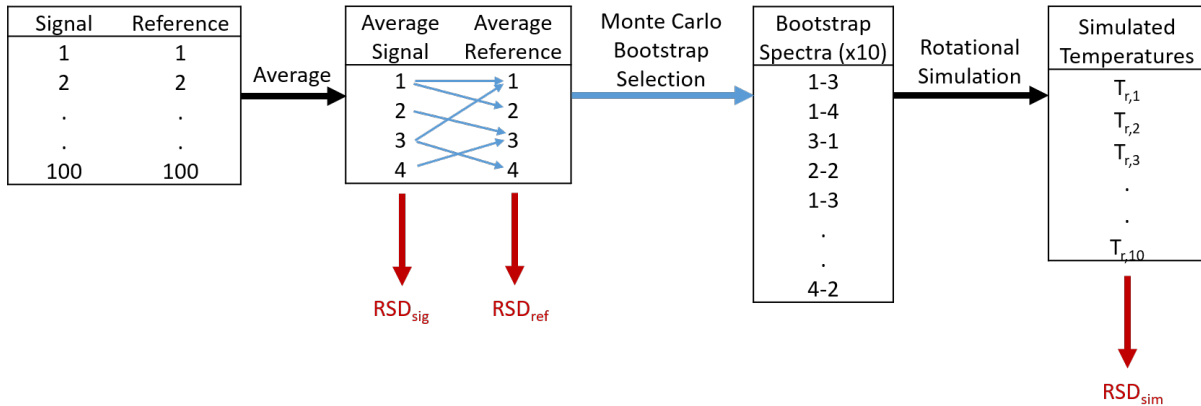


**Figure 3.6** Procedure for analyzing Echelle data. Diagram illustrates the analysis of one time point and the quantification of the relative errors (red) at each step.

The heating trend can be obtained from the main pulse data, but probing pulse data must be used to determine the cooling behavior. The pulsing scheme is shown with idealized temperature traces in red in Figure 3.9a. The  $t_{off}$  between the main pulse and the 1 ms pulse was varied in order to probe the cooling behavior of the plasma. A rising saturation curve was fit to the main pulse, as 10 ms was not long enough for the temperature of the chamber walls and plasma to reach steady state. Such a steady condition would require tens of minutes between pulses, making the experiment impractical. The two term exponential is shown in red in Figure 3.9b.

The probing pulses required a different approach. Originally, six data points were obtained for each 1 ms pulse and unique curves were fit to each, as was done for the main pulse. Selected results are shown in Figures 3.10a and 3.10b. One can see that there is some crossover between pulses. This is not physically plausible, as the gas should monotonically cool in the afterglow of the plasma. During this time the electron temperature has decreased sufficiently that there cannot be further heating reactions like Franck Condon dissociation.

As an alternative to unique projections for each probing pulse, only two projections were developed, one for the main pulse, and one from the starting point of all the off cycle probe pulses. This led to the curves shown in Figure 3.11a. Note how well the end of the main pulse and start of the off cycles agree. The main fit and probing fits are 576 K and 557 K there, respectively, which is

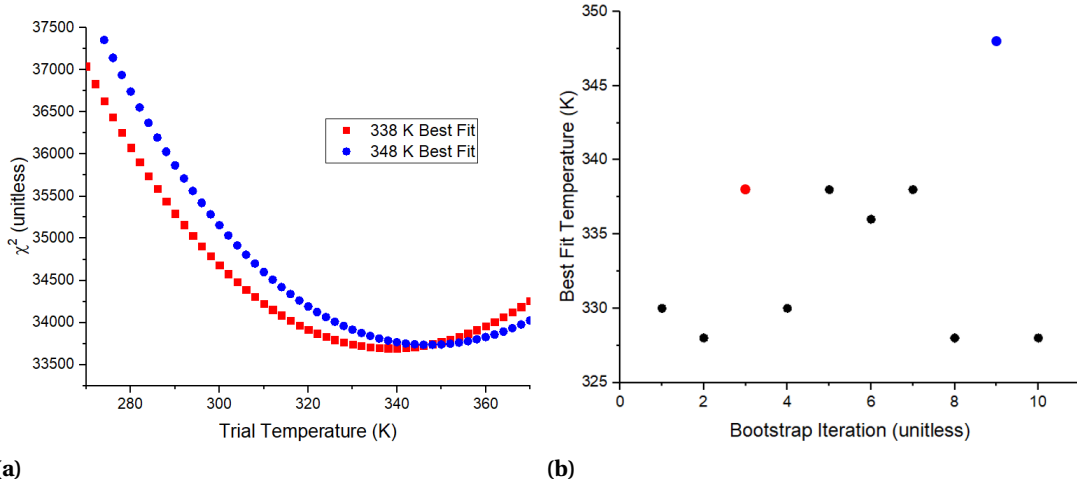


**Figure 3.7** a)  $\chi^2$  minimization that converged at two example temperatures. b) Optimal bootstrap temperature results for ten iterations. The colored points correspond to the  $\chi^2$  examples shown. Example data taken from the first time point of the 10 ms pulse in a 200 W ICP.

remarkably good agreement. The curves also meet at the end of the pulse period,  $t = 80$  ms. There the values are 293 K and 322 K. At 10% relative difference, this is good agreement as well. This serves to validate the projection approach.

Another interesting comparison is between the exponential values. The main and probing fits had coefficients of  $-1.75$  and  $-1.46 \text{ ms}^{-1}$ , and  $0.0065$  and  $-0.0025 \text{ ms}^{-1}$  for the secondary. This is a somewhat surprising result, particularly for the initial heating/cooling coefficients. One would expect that the heating coefficient would be substantially faster than the cooling coefficient; active plasma has extra heating modes such as electron impact dissociation and ion motion through sheath potentials. These species are present in the near afterglow as well but  $T_e$  and  $V_p$  decrease far faster [1, 23], removing the energy that facilitates these gas heating mechanisms. It remains a topic for further exploration.

To summarize, the main pulse captures the heating behavior well enough that the relevant sections of the main pulse projection were 'transferred' to each probing pulse in order to make rising, non-intersecting saturation curves like those shown in Figure 3.11b. The approach ensured that there were no nonphysical, crossing temperature traces. The resulting curves were applied to

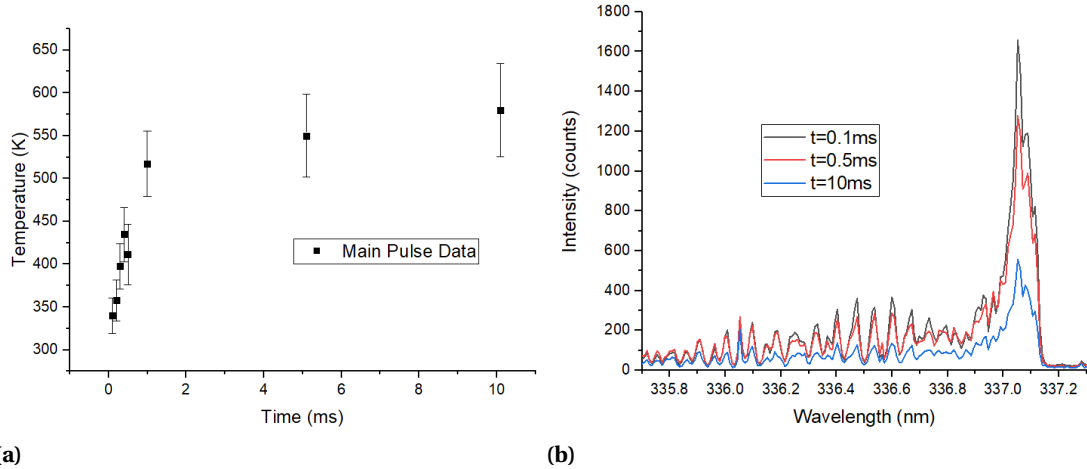


**Figure 3.8** a)  $T_r$  results with overall error included, taking into account simulation and experimental contributions. b) Example average spectra, with reference subtracted, from three selected timesteps that correspond to the data on the left.

the probing pulse of the PIF technique in order to improve that separate diagnostic's accuracy. The outcome is presented in the following chapter.

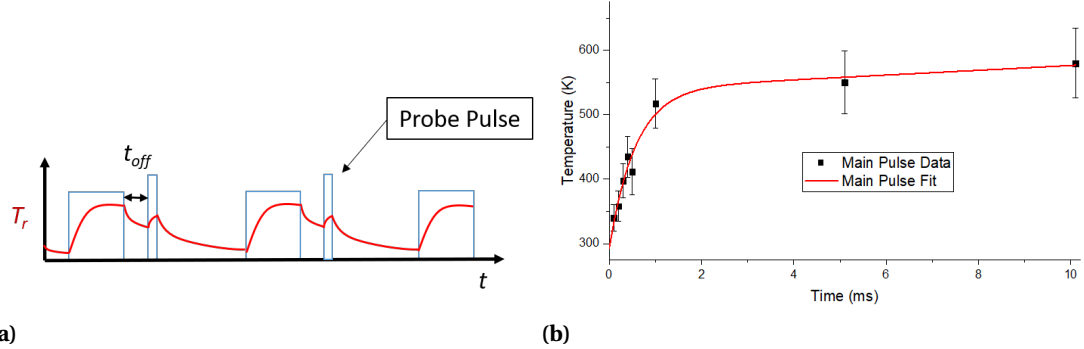


**Figure 3.9** a) Probing pulse scheme. Blue shows the voltage trigger, and was set to different levels to activate the spectrometer only while the generator always triggered. b) Rising saturation fit (red) and  $T_r(t)$  data for the main pulse.

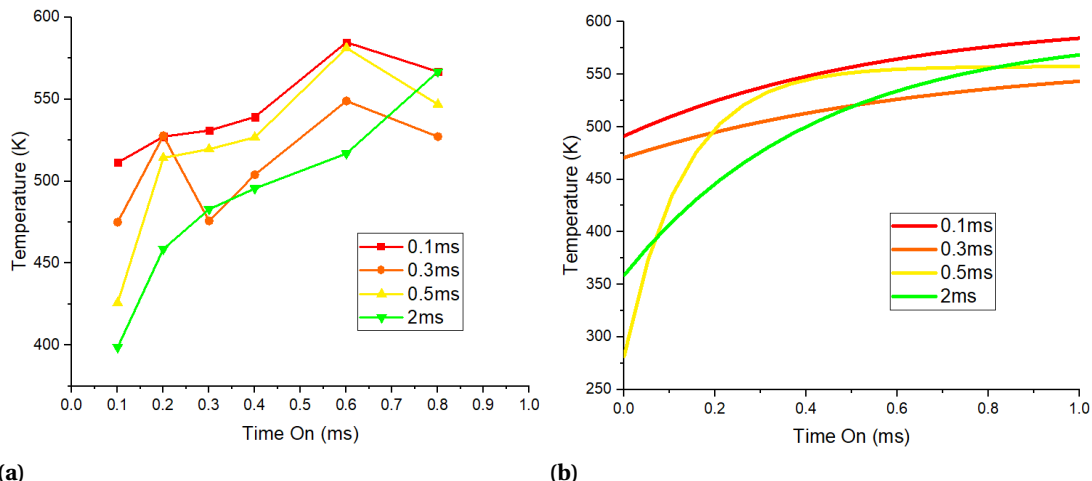


**Figure 3.10** a) Probing pulse  $T_r(t)$  data. Error bars not shown for clarity. Legend indicates time between the end of the main pulse and the start of the trigger for the probing pulse. b) Unique projection results for the probing pulse data shown on the left.

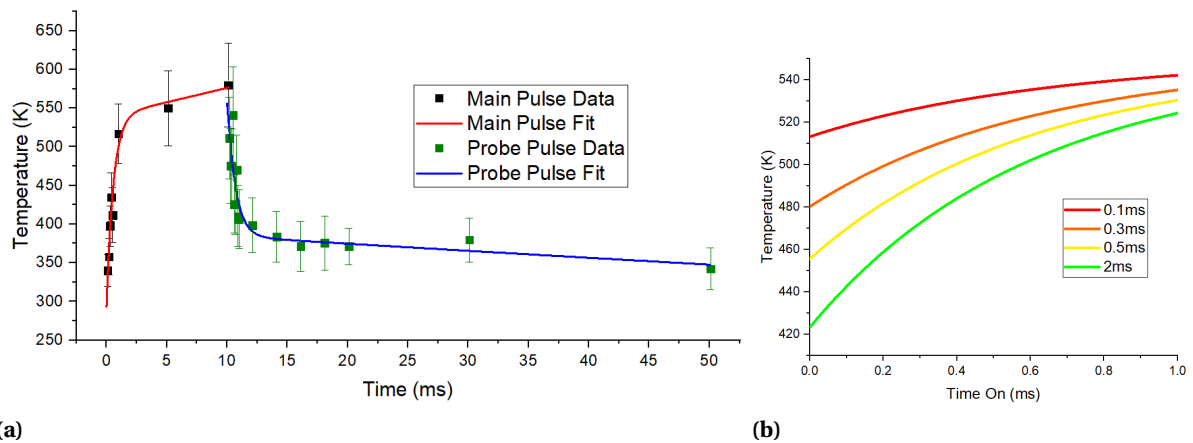


**Figure 3.11** a) Separate projections for the main pulse (red) and the starting point of each probing pulse (blue). b) Resulting transferred projections for selected probing pulse on-cycles.

## CHAPTER

# 4

# PULSE INDUCED FLUORESCENCE WITH SIMULTANEOUS GAS TEMPERATURE MEASUREMENTS

The Pulse Induced Fluorescence (PIF) technique is used for measuring the surface loss of neutral species on plasma-exposed materials. The method relies on accurately measuring the decaying emission intensity of neutrals in the afterglow of a pulsed plasma, when production terms fall to zero in the mass balance. The technique's history and theory was outlined in Chapter 1.4. In this chapter, the specific application to atomic oxygen recombination on quartz is described. Drawbacks to the method are explained and the improvements are described within the results.

To motivate the discussion, consider the effect that uncertainty in recombination coefficient ( $\gamma$ )

has on plasma engineering. The surface reactions are often the largest loss term, and by orders of magnitude compared to volumetric losses. Uncertainty in this parameter will lead to unpredictability in simulations, as was considered for a model of an etch tool [26]. The authors simulated the range of oxygen recombination coefficients found in the literature, which led to the results in Figure 4.3. A critical parameter to control the etch rate of a processing tool is the neutral to ion flux ratio, as both contribute synergistically to surface etch [40]. One can see that the predicted flux ratio varies by an order of magnitude when recombination coefficient is varied [26].

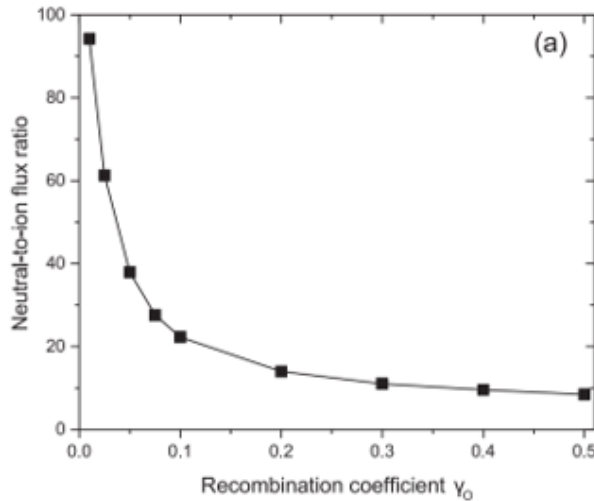


**Figure 4.1** Radical to ion flux ratio at the wafer surface of a planar ICP. The Hybrid Plasma Equipment Model simulated a 500 W and 10 mTorr O<sub>2</sub> plasma [26].

## 4.1 PIF Challenges

Temperature effects present the main challenges to the accuracy of PIF. To begin with, consider wall temperature. PIF measures the surface loss rate of free radicals. Mechanistically, these are lost through either Eley-Rideal or Langmuir-Hinshelwood reactions. Both types are illustrated in Figures 4.2a and 4.2b. The relative contributions of each mechanism to overall recombination rate is highly dependent on wall temperature,  $T_w$  [33, 59]. The reasoning is simple, a higher  $T_w$  will lead to faster

surface movement of physisorbed atoms, allowing them to diffuse across the surface and collide for recombination. On the other hand, as the surface temperature becomes too high, there is sufficient background energy to allow for spontaneous desorption. Then only chemisorption sites can retain the atoms on the surface for an Eley-Rideal recombination.

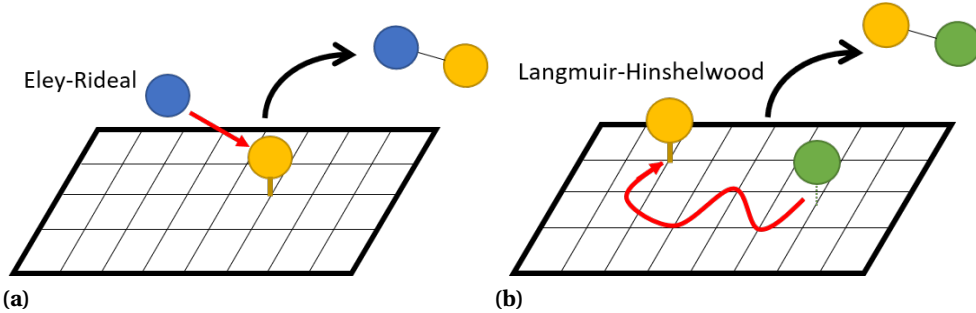


**Figure 4.2** a) Eley-Rideal reaction of gaseous atom (blue) with chemisorbed atom (orange). b) Langmuir-Hinshelwood reaction of chemisorbed and physisorbed (green) atoms. Red arrows represent atom motion.

The  $T_w$  effect becomes problematic during the pulse, when gas heating leads to chamber heating. Early PIF experiments would simply measure the average chamber wall temperature and assume it was equal to the interior temperature, either in a passive [8] or actively cooled wall experiment [57]. However, the power modulates far more than  $T_w$  alone. Ion flux, for example, would increase with power, leading to enhanced surface activity. The  $T_w$  effect is most easily remedied by using a probing pulse scheme, as in Figure 1.14, reproduced below. This keeps the overall deposited power constant from data point to data point. In the main pulse configuration, significant power changes occur as the duty cycle varies from 99% to 20% to get short ( $100\ \mu s$ ) and long (50 ms) off time data points. In the experience of the author, the experiment required at least an hour for the top surface of the chamber to reach a stable temperature, as measured by a IR thermometer. This makes the main pulse configuration impractical as well as inaccurate.

The neutral gas temperature plays a significant role in PIF uncertainty as well. The PIF technique utilizes the following equation for the final calculation, reproduced here from the derivation in

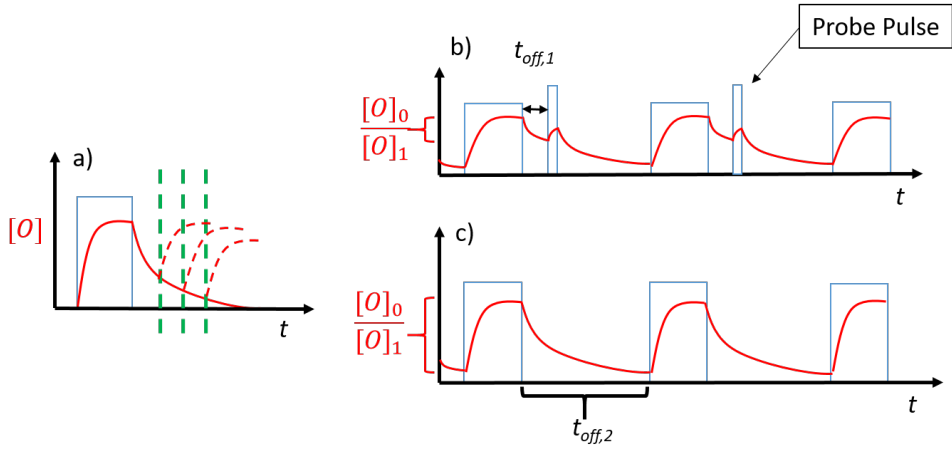


**Figure 4.3** a) Idealized representation of atomic oxygen density (red) in the afterglow of the RF pulse (blue). b) Probing pulse scheme to obtain snapshot in decay density. c) Fixed pulse scheme to determine  $[O]$  decay.

Chapter 1.4.

$$\frac{1}{k_{tot}} = \frac{\Lambda^2}{D} + \frac{V2(2-\beta)}{Sv_{th}\beta} \quad (4.1)$$

The total loss coefficient,  $k_{tot} = k_{wall} + k_{pump}$ , is the parameter measured from the experimental data. The diffusion length  $\Lambda$ , volume  $V$  and surface area  $S$  are all known. The thermal velocity,  $v_{th}$ , is calculated from standard gas kinetics, and the diffusion coefficient ( $D$ ) of atomic O through O<sub>2</sub> is found from the literature for the particular gas temperature and pressure of interest [66]. The  $v_{th}$  and  $D$  terms have a strong  $T_g$  dependence. Figure 4.4 illustrates the results for an initial dataset of oxygen loss coefficient on quartz. A range of  $T_g$  was used to perform the final calculation, which lead to a factor of two variation in loss coefficient.

Others have improved the situation by measuring  $T_r$  within the pulse, then using the average for the final calculation. An example is shown in Figure 4.5 for Cl recombination in a planar ICP [56]. There, the authors added N<sub>2</sub> by 10% gas composition in order to measure  $T_r$  during the on cycle. This approach is used here, but is improved upon by measuring the temperature in the off cycle as well, as discussed in Chapter 3. As will be made clear,  $T_g$  does not contribute to the calculation of  $\beta$  simply through the final calculation in Equation 4.1.

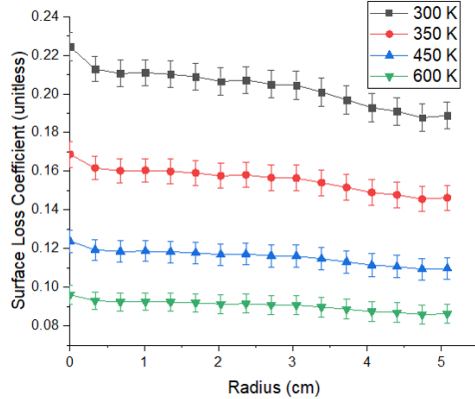


**Figure 4.4** PIF results for varied  $T_g$  assumptions. Error bars are determined by one standard deviation from the goodness of exponential fit. Conditions were 20 mTorr, 50 W power and pure O<sub>2</sub> plasma.

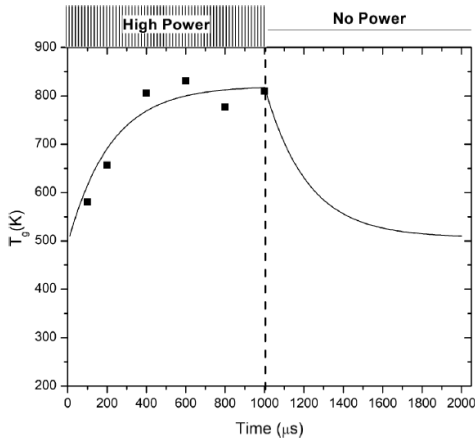


**Figure 4.5** Gas temperature from OES data and spectral fit of N<sub>2</sub> rotational temperature (points). An exponential fit was applied, shown as a solid line. Experiment was 320 W planar ICP with O<sub>2</sub>/Cl<sub>2</sub> gas mixture [56].

$T_g$  contributes to measurement uncertainty of  $k_{tot}$  as well, because the gas density changes within the pulse. Consider that the measured decay  $k_{tot}$  is diagnosing the relative change in emission intensity. The results are typically normalized to the pseudo steady state of the main pulse, when the plasma is the hottest. Therefore one can expect to underestimate the decay coefficient. The reference emission is lower because it is detected from a less dense gas than the  $I(t = 0)$  emission.

The effect is corrected for by also normalizing each data point to gas density.

$$\frac{I_i}{N_i} = \frac{I_{ss}}{N_{ss}} e^{-k_{tot} t} \quad (4.2)$$

where the subscripts  $i$  and  $ss$  refer to the probing pulse and steady state of the main pulse data, respectively. The gas densities  $N$  are substituted for the ideal gas law to obtain

$$\frac{I_i T_i}{I_{ss} T_{ss}} = e^{-k_{tot} t} \quad (4.3)$$

At the time of developing these experiments, another group independently published the same approach [10]. They used rotational temperature and Two-photon Absorption Laser Induced Fluorescence (TALIF) to determine the gas temperature within the pulse of a partially modulated DC plasma, and measured oxygen recombination on pyrex. The  $T_r(t)$  technique is used in this dissertation. Next, the temperature corrected PIF technique will be explained, followed by the results.

## 4.2 PIF Experiment

The oxygen emission data is acquired through a viewing window at the bottom of the Inductively Coupled ARgon Oxygen System (ICAROS), as shown below. An optical setup was mounted to a breadboard below the plasma in order to ensure that only collumnated light is acquired. The goal is to obtain spatially resolved emission data, and thus draw conclusions about the spatial dependence of the afterglow loss. The light is first focused through an off-axis parabolic mirror, and passes through a pinhole at the focal point to eliminate unwanted rays. The light is then collimated with an aspheric lens before passing into a wavelength filter. The tailored image is then sent into a PI-Max3 iCCD camera. The iCCD gates in increments of  $10\ \mu s$  until the end of the probing pulse, and acquires light specifically from the 844 nm line of atomic oxygen due to the wavelength filter.

An external signal generator acts as the trigger for the PI-Max, Echelle spectrometer, and the 13.56 MHz RF generator. The signal pathway is shown in blue, with the respective triggers displayed

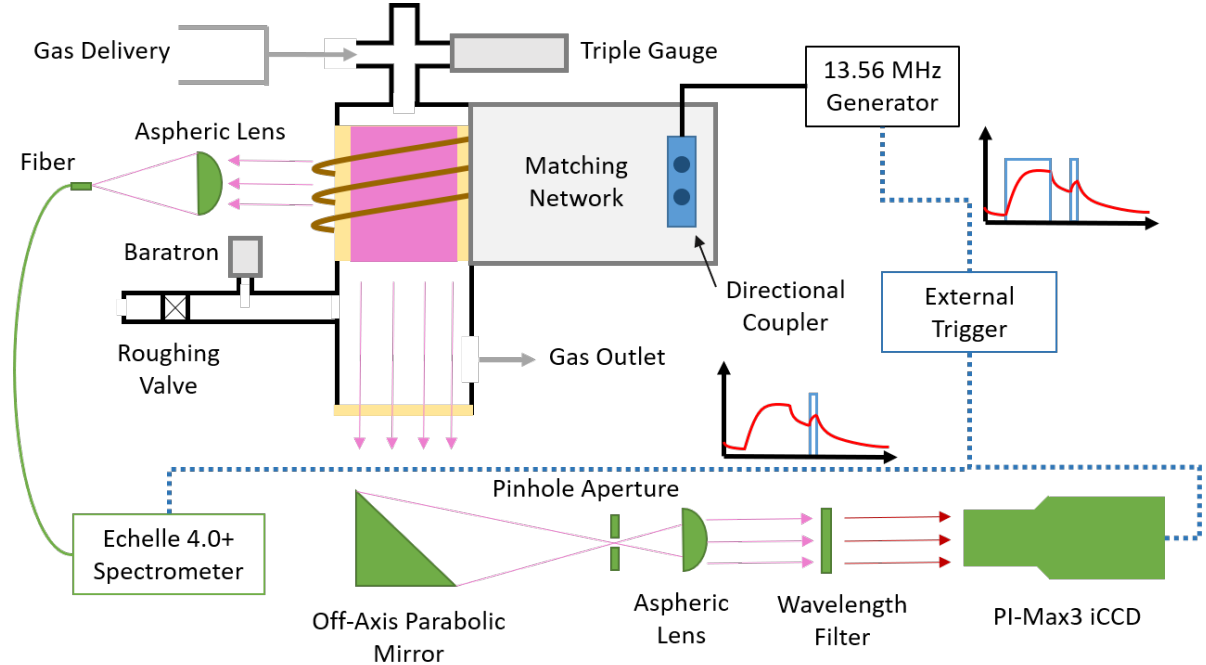


**Figure 4.6** PIF diagnostic setup on the ICAROS plasma source. An optical fiber delivers rovibrational spectra into the Echelle spectrometer. External pulse generation, in blue, provides the unique signals to the RF generator and diagnostic equipment (green). Inset graphs show idealized [O] traces in red together with the unique trigger signals in blue.

as graphs alongside. The main pulse is kept at 10 ms in order to ensure steady state is reached in the plasma during every trigger cycle, and the probing pulse lasts 1 ms. Data is taken from the main pulse once, in order to obtain a steady state oxygen intensity for normalization. An example image is shown below alongside the intensity as a function of time for one pixel. The resulting  $I(r, t)$  data is analyzed in MATLAB to obtain the total decay constant.

The Echelle obtains data through an optical fiber aligned with a collimating lens in order to increase the signal to noise ratio. Therefore the  $T_r(t)$  data represents the whole plasma rather than a spatial distribution, as the iCCD does. The gate width of the Echelle was 100  $\mu$ s in order to obtain sufficient light over 100 pulse accumulations. The plasma parameters were 200 W, 50 mTorr, and 10 sccm with 5% N<sub>2</sub> in order to increase the signal to noise ratio as much as possible.

An example of the raw PImax data is provided in Figure 4.7, which provides data for the (200,200) pixel near the center of the region of interest. The first feature of note is the rapid drop in the probing

pulse intensity at 11.5 ms. This represents the shutoff of the plasma pulse. In theory the trigger is set to last 1 ms, but jitter in the signal generator leads to a precipitous decrease. The same effect is why the first point of the intensity curves should not be taken as the  $I(t = 0)$  datapoint. Due to the strong curvature of the intensities, saturation curves were fit to the offset at  $t \approx 0$ . When normalizing the data, this value is 30%. Attempts were made to gate the iCCD sooner in the pulse and acquire an  $I \approx 0$  data point, but this offset persisted. It was seen for long off times of 100 ms as well, when any residual atomic oxygen will have been lost. The offset is the result of dissociative excitation, the reaction of which is given in Equation 1.21. In the initial on-cycle, a well-known temperature spike results from RF power being coupled into fewer electrons relative to the steady state [23, 72]. The  $T_e$  overshoot increases the reaction rate of dissociative excitation, and the result is an intensity "floor" which cannot be projected beyond to an emission intensity of zero. It is common practice to subtract this portion of the intensity from all the subsequent data so that the normalized intensities will trend towards zero with increasing off time [14]. Otherwise, the exponential decay fit provides unrealistic results.

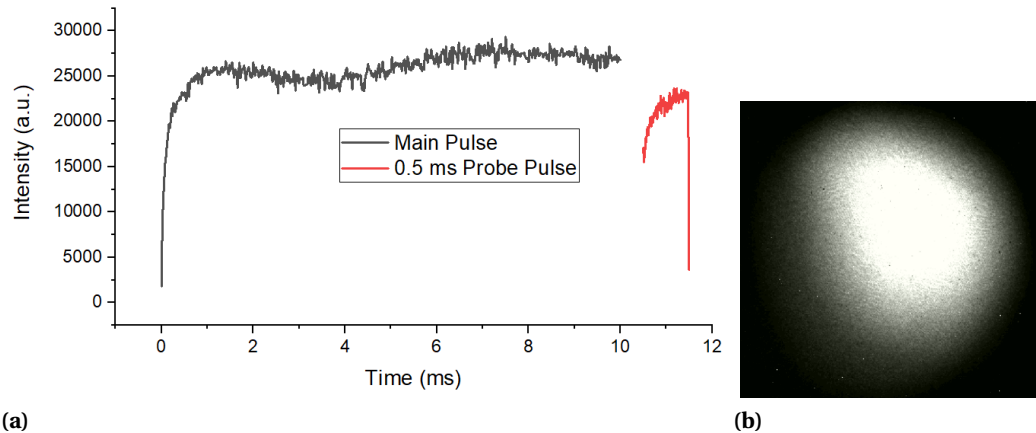


**Figure 4.7** a) Example iCCD output for one pixel. The main pulse begins at 0 ms, and the probing pulse at 10.5 ms for a time off data point of  $t = 500\mu\text{s}$ . b) Raw iCCD image at  $100\mu\text{s}$  into the probing pulse.

The excitation offset is found for each pixel for the longest off time, then the resulting offset

is subtracted from all the other data sets. The 2D data at each time is azimuthally averaged for equidistant radial rings. The procedure is shown in Figure 4.8. The annular data is then projected back in time to  $t = 0$  with a linear fit in order to find the values proportional to  $n_O(t_{off})$ . Ring by ring, these data points are fit to two-exponential decay curves and  $k_{tot}$  is obtained. The goodness of fit for the decay curve determines the error bars on  $\beta$ . These were larger than the individual uncertainties of the  $T_r(t)$  results and the PiMax variance, and so they were used to represent the overall, final uncertainty.

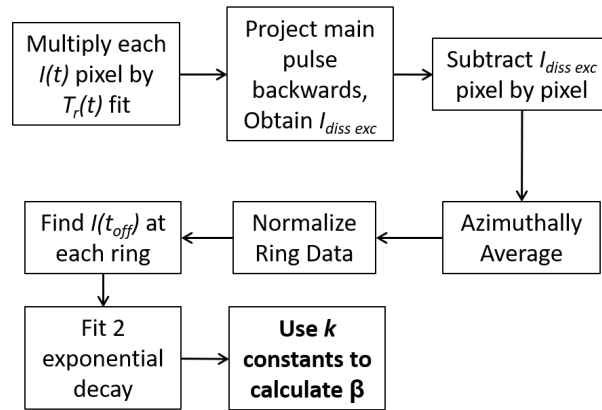


**Figure 4.8** Flow chart depicting Matlab data analysis algorithm. Probing pulses were also  $T_r(t)$  corrected.

The author acknowledges that the procedure could have been performed differently. For example, the data could be azimuthally averaged first before proceeding with the excitation offset, etc. It is the opinion here that corrections should be performed on a pixel by pixel basis first, however, much in the same way that background noise is typically subtracted pixel by pixel.

Other gases were added in trace amounts in order to facilitate the analysis. Argon was added in a 5% composition in order to perform actinometry; the analysis in Figure 4.8 was preceded by division of every  $I_O(x, y, t)$  by every  $I_{Ar}(x, y, t)$  pixel. The results showed good agreement with pure O<sub>2</sub> experiment, within the error bars of the exponential fit. Therefore to save on acquisition and analysis time, Argon was not added to subsequent experiments as further improvements were made.

The choice to forego an actinometer has been published in the literature as well [19]. Nitrogen was also added as 5% of the total gas composition to facilitate  $T_r(t)$  corrections in the final analysis.

### 4.3 PIF Results and Discussion

The temperature corrected PIF results are presented here. The correction contributes in both the raw intensity scaling and the final calculation of  $\beta$  from the exponential decay fit. Figure 4.9 shows the comparison of multiplying each  $I(t)$  by the corresponding  $T_r(t)$ . Both the main pulse and probing pulse are shown, with the time axes originating at the start of their respective on cycles. To consider the probing pulse first, it immediately becomes apparent why the temperature correction will play an important role. Without the correction, the decay in the off cycle will be underestimated. On the side of the main pulse, the dissociation excitation offset will be overestimated.

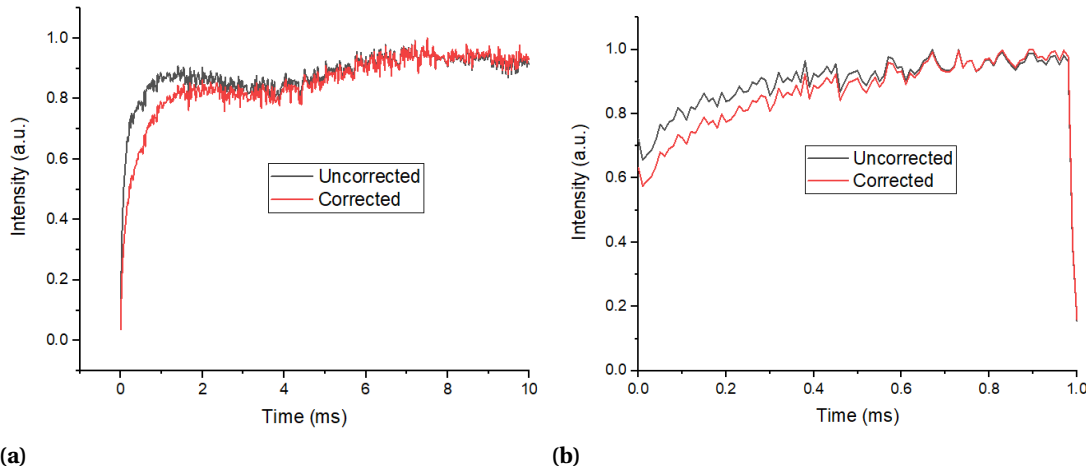


**Figure 4.9** Example iCCD output for one pixel (black) compared to the temperature corrected result (red) for the main pulse in a) and the probing pulse in b) which has a  $500 \mu\text{s}$  delay following the end of the main pulse. All values have been normalized to their relative maxima.

These results are normalized for illustrative purposes only. The temperature correction was performed for each data point and a fit performed for the non-normalized result, as in Figure 4.10.

The normalization of the probing data occurs by dividing each data point by the  $I(t = 10)$  ms fit of the main pulse, as this represents the maximum [O] prior to generator shutoff. A key feature of Figure 4.10a is the upwards trajectory; a pseudo-steady state is never reached. This reflects the fact that  $T_r$  will continue to rise as the main pulse is extended in time and the experimental chamber continues to heat. Although the main pulse could equilibrate with a long pulse of minutes or hours, the experiment becomes impractical. Reaching a true steady state is less important than having a main pulse that consistently regenerates a starting [O] for subsequent decay in the afterglow. This was achieved here, as the relative standard deviation (RSD) of the raw iCCD data was less than 5% in most cases. The iCCD data was acquired in triplicate to determine the variance. The other feature is that the beginning of the pulse exhibits a strong curvature, which has been zoomed in on for Figure 4.10b. Whereas others have effectively used a linear projection to accurately obtain  $I(t = 0)$  [14], an exponential rise is more accurate for this experiment.

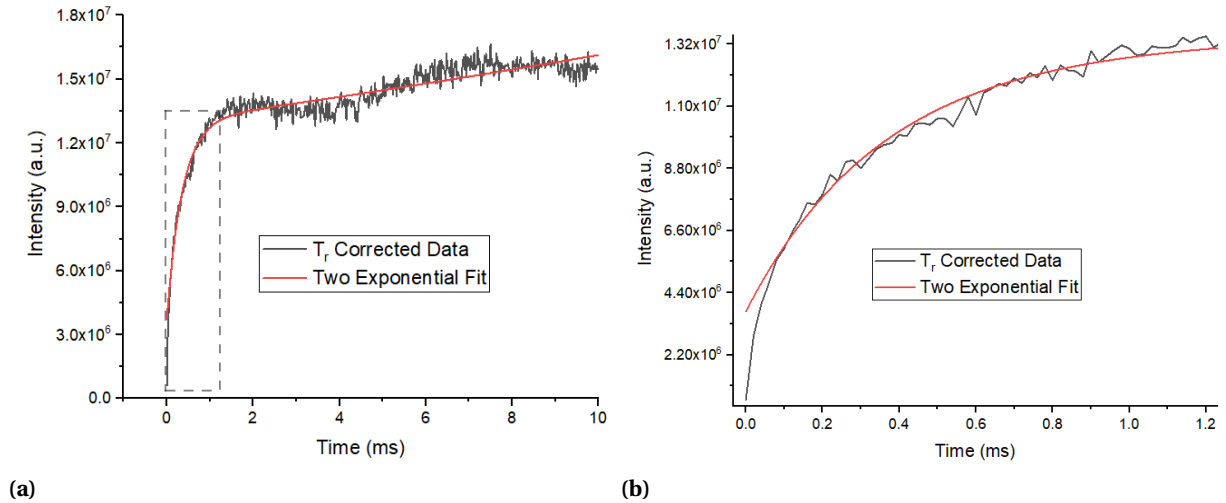


**Figure 4.10** Example iCCD output for one pixel with temperature correction (black). Exponential rise models were fit to accurately determine  $I(t = 0)$ , shown in red. b) provides the same figure but zoomed in for clarity.

The temperature corrected data is further processed through the steps outlined in Figure 4.8. To obtain  $k_{tot}$ , a two exponential decay is fit to the data for each annular ring of the PiMax region

of interest. Figure 4.11b shows the result of the fit. A clear two exponential decay is seen, as others have detected [14]. It provided an excellent R-squared value of 0.98, proving that two  $k_{tot}$  terms are necessary. They will be referred to as  $k_1$  and  $k_2$ . The  $k_1$  and  $k_2$  values were 1.66 and  $2.82 \times 10^{-4} \text{ ms}^{-1}$ , highlighting again the difference between *in situ* measurements and remote plasma species decay measurements. The near afterglow shows an orders of magnitude more rapid [O] loss because the quartz surface has become more active. This was the explanation offered by Cartry et al, who also studied oxygen loss on pyrex and performed a two decay fit [14]. The author agrees with this interpretation of the intensity data.

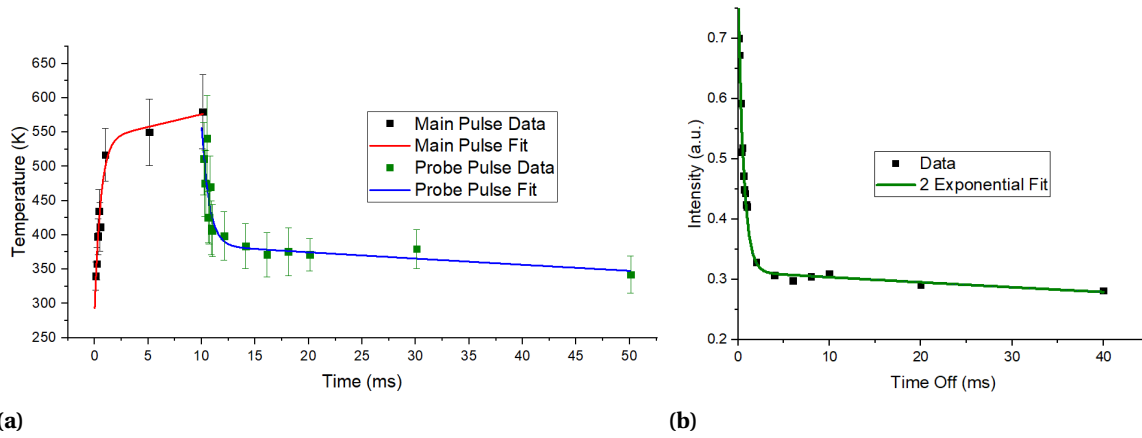


**Figure 4.11** a) Temperature curves for main pulse and probing pulse in the afterglow. b) Exponential fit (green) and final data (black) for the temperature corrected PIF. The outermost annular ring is shown, representing a disk extending 1 cm inwards from the quartz edge.

The final calculation of  $\beta$  requires a single  $T_g$  for the diffusion coefficient and thermal velocity terms of Equation 4.1. The exponential results in Figure 4.12 show the need for choosing a temperature in the first 1 ms of the off cycle. However, the  $T_r(t)$  results show a rapid drop from 520 to 400 K in the first ms of the afterglow. The temperature result is reproduced from Chapter 3 in Figure 4.11a. This should lead to a more complex decay function in the first ms of the off cycle. However, the separated decay constants show good fit and linearity in a semilogarithmic plot in Figure 4.12.

An argument could be made that there is an intermediate decay in the 1-2 ms region, but adding this additional decay to the fitting model lead to a worse R-squared value of 0.9. An attempt was made to fit a general model of

$$I = a e^{-k_1 t^b} \quad (4.4)$$

in order to uncover a stronger  $T_r(t)$  dependence, but these provided worse fits as well.

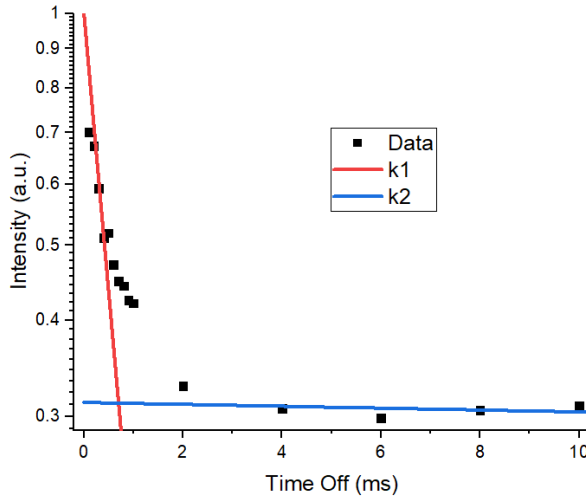


**Figure 4.12** Exponential fit (lines) and final data (black) for the temperature corrected PIF. The outermost annular ring is shown, representing a disk extending 1 cm inwards from the quartz edge. A starting value of 1 was used for the  $k_1$  fit, as the original fitting model provides separated coefficients.

An intermediate  $T_g$  of 450 K was chosen for the final calculation. The results for the surface loss coefficient are shown in Figure 4.13. An obvious question is what does  $\beta$  in the center of the discharge mean, if it is a *surface* loss coefficient. In the low pressure 50 mTorr condition here, there is no volumetric loss of [O] [10, 14]. The apparent loss away from the quartz surface at  $R = 5$  cm reflects the free diffusion of [O] towards the surface sink. A flat profile indicates that the experiment was well designed; [O] is not restricted by diffusion in order to be lost on the surface. In that case, an increasing distribution for  $\beta(r)$  would be found. That is the overall purpose of the PiMax iCCD data, to experimentally validate the assumption that the atoms can freely diffuse to the surface and so

the diffusion model can be applied [17]. The final result, then, is  $\beta_1 = 0.39 \pm 0.07$ .

Compare this to the alternative. The data was reprocessed without  $T_r(t)$  correction, and a range of 'educated guesses' for the final  $\beta$  calculation was evaluated. For temperatures of 400 to 500 K,  $\beta$  varied from 0.29 to 0.53. When adding the uncertainty from goodness of the decay fit, the range widens to  $0.23 < \beta < 0.79$ . Even evaluated at  $T_g = 450K$ , the surface loss coefficient result is 0.33, 15% lower than the improved PIF technique that has been developed here. The  $T_r(t)$  correction at each data point plays a smaller role than the final calculation in Equation 4.1, but both contribute to enhancing the accuracy of  $\beta$ .

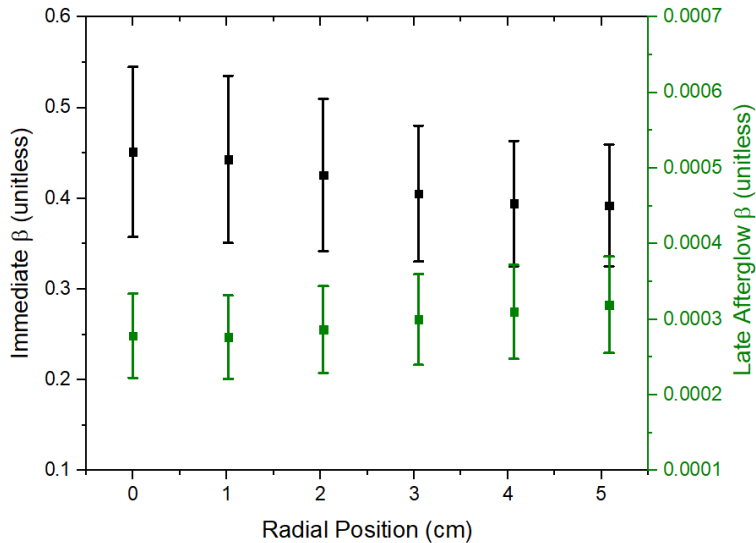


**Figure 4.13** Surface loss coefficient results from  $k_1$  (black) and  $k_2$  (green). The  $R = 0$  cm point represents the center of the discharge, and  $R = 5$  the plasma edge. Error bars were determined from the goodness of fit for  $\beta_1$ , and an estimated RSD of 20% for the secondary  $\beta_2$ .

The final result of 0.39 is significantly higher than that reported in the literature. These are summarized in Table 4.1. Note that the 1 and 2 subscripts refer to the activated and inactive surface, respectively. The range of values is for varying conditions of pressure, surface temperature, etc. The materials are either Pyrex or quartz. It is difficult to compare values directly, for most experiments were performed in the intermediate pressure range. In collisional regimes, it is expected that ion

energies will be reduced and therefore surface activation decreased. Booth et al. showed evidence of increasing  $\gamma_1$  with lower pressure, but did not go below 200 mTorr [10]. Their experiment was a DC discharge as well, which reduces ion bombardment energy compared to RF plasmas. RF discharges typically have higher plasma and floating potentials. The closest case in the literature is the work by Cartry et al, which measured surface loss in a microwave discharge with the probing pulse and actinometric method [14]. Their results were as high as 0.07 with the error bars for the 500 mTorr case, but they did not go below this pressure.

**Table 4.1** Literature Surface Loss Values

Parameter	Range	Plasma Type	Pressures (Torr)	Reference
$\beta_1$	[0.32,0.46]	RF ICP	0.05	This Work
$\beta_1$	[0.023,0.07]	Microwave	0.5-2	[14]
$\gamma_1$	[0.2,1.5]x10 <sup>-3</sup>	DC	0.2-10	[10]
$\gamma_1$	[1.2-9.1]x10 <sup>-3</sup>	RF ICP	100-200	[24]
$\beta_2$	[2.6,3.8]x10 <sup>-4</sup>	RF ICP	0.05	This Work
$\beta_2$	[1.9,5.0]x10 <sup>-4</sup>	Microwave	0.5-2	[14]
$\gamma_2$	[0.5,1.1]x10 <sup>-4</sup>	RF ICP	1 Torr	[92]

A promising trend is that the results for the secondary decay coefficient, and corresponding  $\beta_2$ , agree well with the literature. In those remote plasma experiments, the pressure and power source are not nearly as relevant, because ion bombardment does not reach the surface directly. The level of agreement lends confidence to the  $\beta_1$  result. The high range is likely caused by the enhanced ion flux in a low pressure RF discharge. To the author's knowledge, this is the first experimental result in the low pressure, RF regime that is relevant to the semiconductor processing community. When recalling the simulation study of ion to radical flux ratio at the beginning of this chapter (Figure 4.3), the conditions were 500 W of RF in a 10 mTorr oxygen ICP [26]. Between the previous value of 0.07 and the 0.39 result here, the ratio would vary by a factor of 2 in that particular ICP. Others have speculated that increased ion flux can lead to more rapid silanol removal and active site generation [10], though more could be done to refine the experiment and verify this claim. The future work that

this research points towards is discussed in the final chapter.

## CHAPTER

# 5

## CONCLUSIONS AND FUTURE WORK

### 5.1 Work to Date

This dissertation addressed key uncertainties in two plasma diagnostics: the microwave hairpin probe and pulse induced fluorescence. The error reduction was accomplished through the novel use of pulsed plasma as a diagnostic, a technique which uses power modulation to create transients that provide unique insights into plasma parameters. The technique's history is surveyed in Section 1.3, which builds upon the plasma dynamics provided in Section 1.2.

PIF is a method that relied on pulse plasma as a diagnostic before this work [14, 19]. Here, the technique was applied to atomic oxygen emission of 844 nm in order to determine surface loss probability on quartz. The diagnostic was improved upon by simultaneously measuring the 337 nm rotational band of trace N<sub>2</sub>. The rotational spectra provided  $T_r(t)$  results that are presented in Chapter 3, where the heating and cooling cycles of a PIF power pulsing scheme were independently

quantified. A high level of agreement between the on and off cycle temperatures was achieved; the start/end temperatures lie within each others' error bars. This lends support to the pulsed  $T_r(t)$  approach. The uncertainty was rigorously quantified for both experimental and simulation error, leading to overall relative standard deviations of  $< 9\%$  for all data points. The theory and procedure was fully detailed in Sections 1.5 and 3.1 so as to provide a one stop shop for those who want to reproduce the diagnostic.

The  $T_r(t)$  results were applied as a correction factor to the PIF signal in Chapter 4. The correction leads to a higher  $\beta$ ; one can see that this must be the case from the raw data comparison in Section 4.3. The improved PIF method led to a primary surface loss coefficient of  $0.32 < \beta_1 < 0.46$ , which is higher than the literature values [10, 14] for loss or recombination coefficients of oxygen on glass surfaces. To date, no one has performed PIF for atomic oxygen in an RF low pressure plasma that is similar to semiconductor processing conditions. The loss coefficient for the late afterglow,  $\beta_2$ , was  $3.2 \pm 0.6 \times 10^{-4}$ , in good agreement with previous microwave source work at moderate pressures [14]. The agreement lends support to the  $\beta_1$  result, which is expected to be higher for low pressure RF plasmas due to increased ion bombardment energy in the collisionless regime.

While PIF was an existing pulsed plasma as diagnostic, the pulse technique had never been applied to the HP diagnostic. Prior to this work, there was concern about the accuracy of HP density measurements [30]. The uncertainty primarily stemmed from sheath formation as a result of DC and RF potentials on the probe. By pulsing the plasma with full power modulation, both components of the potential fall within  $\mu\text{s}$ . The result is sheath collapse and expansion into the previously voided region around the HP tines, creating a rise in  $n_e$  termed the hairpin spike. The HS density provides a more accurate measurement than the pseudo steady state density measurement preceding it, as the perturbative effect of the sheath has been removed. In order to study the validity of the technique, the sheath correction factor developed by others [78] was modified in order to calculate the sheath width as a multiple of Debye lengths. Data was acquired for a range of densities for two HPs of varying widths, and both cases trended towards  $k = 1$ , as expected when the sheath size decreases with increasingly dense plasma. The results demonstrated the utility of the HS method; the relative

impact of the sheath perturbation was within the expected bounds of the analytical model.

## 5.2 Future Work

Further development can be made around floating HPs, which are DC isolated from ground. In principal, a floating sheath is less perturbative than a grounded sheath because the potential drop is smaller. The analysis is also simpler because an equivalent flux condition,  $\Gamma_i = \Gamma_e$ , is well defined in the floating sheath. HS data was taken for a floating probe, which led to the  $k$  values in Figure 5.1. The results were surprising in that  $k < 1$  for the full range of RF powers. This disagrees with modeling work done by others, which predicted  $3 < k < 6$  over most plasma conditions facing a floating surface [15].

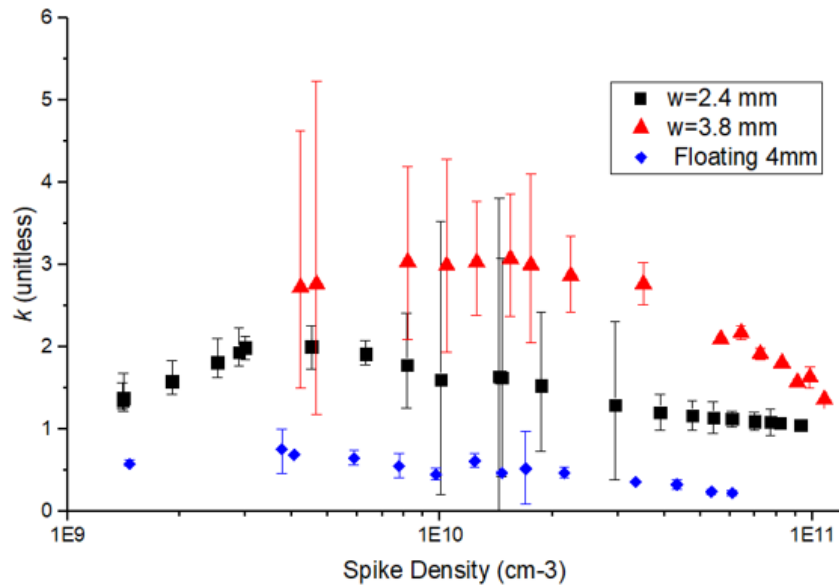


**Figure 5.1** Number of Debye lengths used to correct  $n_{e,ss}$  up to the HS density for two grounded HPs and one floating HP. Plasma conditions: 10 mTorr Ar, 3 sccm. Power pulsed at 500 Hz and 80% duty cycle.

The floating probe results can be tentatively attributed to the HP time response. A negative charge is built upon any floating surface, and this must discharge or neutralize in order for the

surface to allow the sheath to collapse. Conceptually, the negative surface charge inhibits the spread of electrons into the voided sheath region. This introduces a time lag, and once the sheath has stabilized the bulk  $n_e$  has already significantly fallen. In contrast, the grounded HP follows the plasma potential instantaneously as it drops to near zero in the immediate afterglow. It is interesting to note that the HS densities of the floating and grounded probes agree with each other to a much smaller relative error than the  $n_{e,ss}$  values. An example trace of both a floating probe and grounded HP is provided in Figure 5.2a. The two HS agree well, nearly within their error bars, yet the steady state data is more significantly offset. The floating probe density has been reported to be larger than the grounded probe in CW plasmas, as well [70].

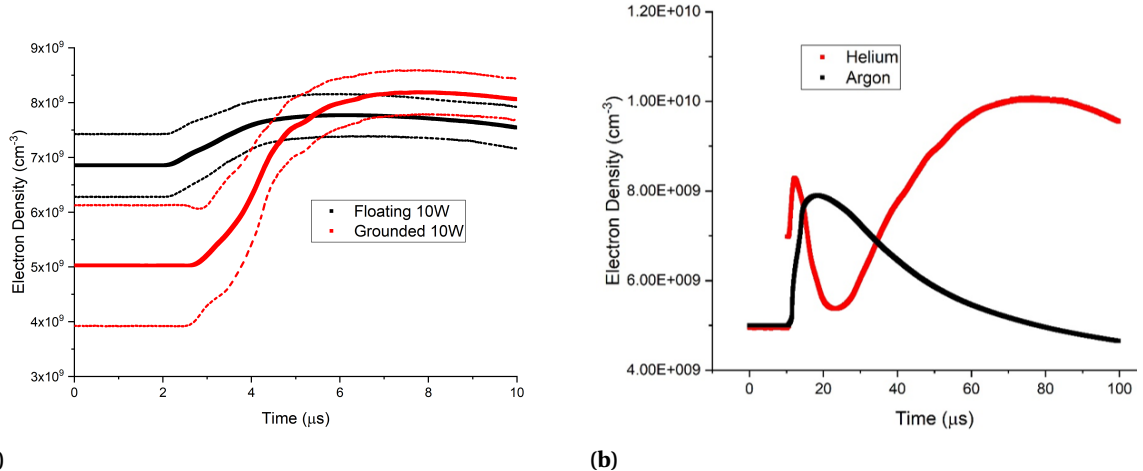


**Figure 5.2** a) HS of a 3.35 mm floating probe (red) and 4.05 mm grounded probe (black) at 10 W, 10 mTorr Ar pulsed with 500 Hz and 80% duty cycle. Error limits are shown as dashed ranges. b) 20 mTorr, 1 kHz pulsing plasma conditions compared between an Ar and He discharge. The power was increased from 10 to 16 W to sustain a similar steady state  $n_e$  in the latter case [25].

Up to this point, all of the data was analyzed with the magnitude of the steady state and HS densities. However, there may be additional information to gain from the *shape* of the HS as well. Figure 5.2b, which has been reproduced from Chapter 2, and one can see that the HS of He and Ar have similar magnitudes but the rise of the He trace is significantly faster. The result is expected for

He discharges, which usually have higher  $V_p$  and  $T_e$  due to the higher ionization energy of He, 24.6 eV as opposed to the 15.8 eV ionization energy of Ar. The approach could be similar to the work of Sirse et al., who studied the decay behavior of a HP in electronegative gases to qualitatively estimate negative ion temperature [80]. The concept relied on negatively biasing the probe to evacuate electrons and negative ions from the HP, then fitting an exponential to the relaxation as the bias was shut off.

For the  $T_r(t)$  diagnostic, an improvement has already been made with the help of Dr. Marcel Fiebrandt, who helped us align the Echelle spectrometer CCD so as to increase the signal to noise ratio significantly. This will help with relative uncertainties and data acquisition time in the future, which is greatly appreciated. From the results in Figure 3.11a, it was interesting that the heating and cooling time constants were so similar, within 20% relative difference. The two constants should be sensitive to gas pressure, as this determines the neutral-neutral collision frequency. A possible experiment would be to fix  $n_e$  by modifying power over a range of gas pressures. By using the same probing pulse scheme, one could obtain the heating and cooling constants again. It is expected that both rate constants would decrease with pressure. The heating coefficient may decrease at a more rapid rate, however, since it is sensitive to electron-neutral and neutral-neutral collision frequency. The cooling cycle is likely to be sensitive to only the latter collisions and the chamber surface, which acts like a heat sink but is fixed.

The  $T_r(t)$  measurements could be made more suitable for the oxygen PIF experiment as well. Others have used the atmospheric A-band of O<sub>2</sub> at 760 nm to determine  $T_r$  [86, 96]. That is the approach taken by Booth et al, who concurrently developed a  $T_r(t)$  correction factor for oxygen PIF on pyrex [10]. It was not employed here because the 760 nm region was outside the measurement range of the Echelle spectrometer. The removal of trace nitrogen would settle the question of  $\beta$  versus  $\gamma$ . One may question whether there was N-O combination on the surface. This would lead to a  $\beta$  diagnostic rather than the more specific recombination coefficient,  $\gamma$ . There was no detected NO emission in the 236 nm or 304 nm regions, however. The author chose to report the PIF results as  $\beta$  out of caution; it is difficult to prove a negative. For a pure oxygen experiment, though, one may

safely conclude that atomic oxygen recombination was the only surface reaction observed. The next step would be to increase the gas pressure up to 300 mTorr, bridging the pressure gap between this work and Booth et al [10]. They predicted that  $\gamma$  would decrease linearly with increasing pressure, and it would be interesting to expand upon their work.

To estimate the impact of the surface loss on plasma chemistry, we have begun collaboration with simulation experts at the University of Michigan. With their permission, the effect of varying  $\gamma$  on atomic oxygen concentration is reproduced in Figure 5.3. One can see that the density is significantly lower from this work than the results of the highest  $\gamma$  value of 0.07 from the previous literature. A further comparison could be between decay rates in the afterglow as a function of  $\gamma$ . This would test the level of agreement between simulation and experiment under conditions that reduce simulation uncertainty. The rate constants for atomic oxygen production each have an associated error, but these contributions to absolute density no longer play a role in the afterglow.

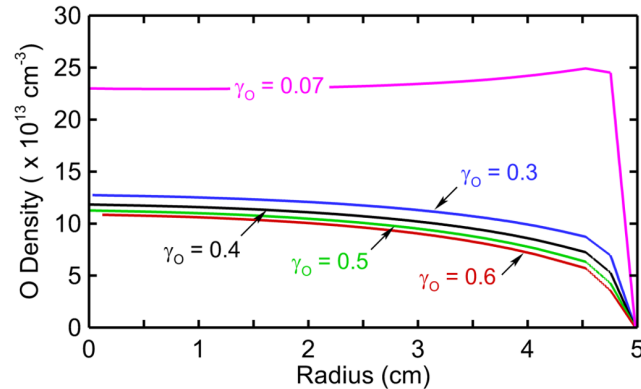


**Figure 5.3** Hybrid plasma equipment model of ICAROS experiment under steady state conditions: 200 W, 50 mTorr of O<sub>2</sub> with 10 sccm. Radius of zero refers to plasma center.

Pulsed plasma is a powerful technique for expanding diagnostic capabilities. It removes sheath perturbation around hairpin probes, leading to more accurate electron density measurements. Pulsed plasmas also allow for simplified analytical models; the PIF technique was developed from a simple mass balance in the afterglow, when the free radical density is modelled by straightforward

exponential decay. The probing pulse scheme led to heating and cooling cycle insights for neutral gas, as well. If electrons, free radicals, and background gas can all be studied through power modulation, then clearly there is ample opportunity for continued experiments with pulsed plasma as a diagnostic.

## BIBLIOGRAPHY

- [1] Ahn, T. et al. "Negative ion measurements and etching in a pulsed-power inductively coupled plasma in chlorine". *Plasma Sources Science and Technology* **5**.2 (1996), p. 139.
- [2] Bai, B. et al. "Neutral gas temperature measurements of high-power-density fluorocarbon plasmas by fitting swan bands of C<sub>2</sub> molecules". *Journal of applied physics* **99**.1 (2006), p. 013308.
- [3] Banna, S. et al. "Inductively coupled pulsed plasmas in the presence of synchronous pulsed substrate bias for robust, reliable, and fine conductor etching". *IEEE Transactions on Plasma Science* **37**.9 (2009), pp. 1730–1746.
- [4] Banna, S. et al. "Pulsed high-density plasmas for advanced dry etching processes". *Journal of Vacuum Science & Technology A: Vacuum, Surfaces, and Films* **30**.4 (2012), p. 040801.
- [5] Bell, A. T. & Kwong, K. "Dissociation of oxygen in a radiofrequency electrical discharge". *AIChE Journal* **18**.5 (1972), pp. 990–998.
- [6] Bodart, P et al. "Analysis of pulsed high-density HBr and Cl<sub>2</sub> plasmas: Impact of the pulsing parameters on the radical densities". *Journal of Applied Physics* **110**.11 (2011), p. 113302.
- [7] Booth, J.-P. et al. "Gas temperature measurements in oxygen plasmas by high-resolution Two-Photon Absorption Laser-induced Fluorescence". *Journal of Instrumentation* **10**.11 (2015), p. C11003.
- [8] Booth, J. & Sadeghi, N. "Oxygen and fluorine atom kinetics in electron cyclotron resonance plasmas by time-resolved actinometry". *Journal of applied physics* **70**.2 (1991), pp. 611–620.
- [9] Booth, J. et al. "Spatially and temporally resolved laser-induced fluorescence measurements of CF<sub>2</sub> and CF radicals in a CF<sub>4</sub> rf plasma". *Journal of Applied Physics* **66**.11 (1989), pp. 5251–5257.
- [10] Booth, J. et al. "Oxygen (3P) atom recombination on a Pyrex surface in an O<sub>2</sub> plasma". *Plasma Sources Science and Technology* **28**.5 (2019), p. 055005.
- [11] Brake, M et al. "Dissociation and recombination of oxygen atoms produced in a microwave discharge. Part I. Experiment". *Plasma Chemistry and Plasma Processing* **3**.1 (1983), pp. 63–78.
- [12] Bruggeman, P. et al. "Gas temperature determination from rotational lines in non-equilibrium plasmas: a review". *Plasma Sources Science and Technology* **23**.2 (2014), p. 023001.
- [13] Budó, A. "Über die Triplet-Bandentermformel für den allgemeinen intermediären Fall und Anwendung derselben auf die B 3Π-, C 3Π-Terme des N 2-Moleküls". *Zeitschrift für Physik* **96**.3-4 (1935), pp. 219–229.

- [14] Cartry, G. et al. "Atomic oxygen surface loss probability on silica in microwave plasmas studied by a pulsed induced fluorescence technique". *Plasma Sources Science and Technology* **15**.3 (2006), p. 479.
- [15] Chabert, P. "What is the size of a floating sheath?" *Plasma Sources Science and Technology* **23**.6 (2014), p. 065042.
- [16] Chabert, P. "What is the size of a floating sheath?" *Plasma Sources Science and Technology* **23**.6 (2014), p. 065042.
- [17] Chantry, P. "A simple formula for diffusion calculations involving wall reflection and low density". *Journal of applied physics* **62**.4 (1987), pp. 1141–1148.
- [18] Conway, G. et al. "Evolution of ion and electron energy distributions in pulsed helicon plasma discharges". *Plasma Sources Science and Technology* **7**.3 (1998), p. 337.
- [19] Curley, G. et al. "Surface loss rates of H and Cl radicals in an inductively coupled plasma etcher derived from time-resolved electron density and optical emission measurements". *Journal of Vacuum Science & Technology A: Vacuum, Surfaces, and Films* **28**.2 (2010), pp. 360–372.
- [20] Darnon, M. et al. "Time-resolved ion flux, electron temperature and plasma density measurements in a pulsed Ar plasma using a capacitively coupled planar probe". *Plasma Sources Science and Technology* **23**.2 (2014), p. 025002.
- [21] Donnelly, V. M. & Flamm, D. L. "Studies of chemiluminescence accompanying fluorine atom etching of silicon". *Journal of Applied Physics* **51**.10 (1980), pp. 5273–5276.
- [22] Donnelly, V. et al. "Critical review: Plasma-surface reactions and the spinning wall method". *Journal of Vacuum Science & Technology A: Vacuum, Surfaces, and Films* **29**.1 (2011), p. 010801.
- [23] Economou, D. J. "Pulsed plasma etching for semiconductor manufacturing". *Journal of Physics D: Applied Physics* **47**.30 (2014), p. 303001.
- [24] Fletcher, D. & Meyers, J. "Surface catalyzed reaction efficiencies in oxygen plasmas from laser-induced fluorescence measurements". *Journal of Thermophysics and Heat Transfer* **31**.2 (2016), pp. 410–420.
- [25] Ford, K. et al. "Measurement of localized plasma perturbation with hairpin resonator probes". *Physics of Plasmas* **26**.1 (2019), p. 013510.
- [26] Gibson, A. R. et al. "The role of thermal energy accommodation and atomic recombination probabilities in low pressure oxygen plasmas". *Plasma Physics and Controlled Fusion* **59**.2 (2017), p. 024004.
- [27] Godyak, V. & Piejak, R. "Abnormally low electron energy and heating-mode transition in a low-pressure argon rf discharge at 13.56 MHz". *Physical review letters* **65**.8 (1990), p. 996.

- [28] Godyak, V. et al. "Measurement of electron energy distribution in low-pressure RF discharges". *Plasma sources science and technology* **1**.1 (1992), p. 36.
- [29] Godyak, V. et al. "Electron energy distribution function measurements and plasma parameters in inductively coupled argon plasma". *Plasma Sources Science and Technology* **11**.4 (2002), p. 525.
- [30] Godyak, V. "Comments on plasma diagnostics with microwave probes". *Physics of Plasmas* **24**.6 (2017), p. 060702.
- [31] Greenberg, K. & Hebner, G. "Electron and metastable densities in parallel-plate radio-frequency discharges". *Journal of applied physics* **73**.12 (1993), pp. 8126–8133.
- [32] Greig, A. et al. "Neutral gas temperature estimates and metastable resonance energy transfer for argon-nitrogen discharges". *Physics of Plasmas* **23**.1 (2016), p. 013508.
- [33] Guerra, V. "Analytical model of heterogeneous atomic recombination on silicalike surfaces". *IEEE Transactions on plasma science* **35**.5 (2007), pp. 1397–1412.
- [34] Haas, F. et al. "Electron and ion sheath effects on a microwave hairpin probe". *Applied Physics Letters* **87**.20 (2005), p. 201503.
- [35] Hancock, G. et al. "Plasma kinetic measurements using time-resolved actinometry: comparisons with laser-induced fluorescence". *Journal of Physical Chemistry* **94**.8 (1990), pp. 3269–3272.
- [36] Hartmann, G & Johnson, P. "Measurements of relative transition probabilities and the variation of the electronic transition moment for N<sub>2</sub> C<sub>3</sub>Pu-B<sub>3</sub> Πg second positive system". *Journal of Physics B: Atomic and Molecular Physics* **11**.9 (1978), p. 1597.
- [37] Herzberg, G. *The spectra and structures of simple free radicals: an introduction to molecular spectroscopy*. Courier Corporation, 1988.
- [38] Herzberg, G. *Molecular spectra and molecular structure*. Vol. 1. Read Books Ltd, 2013.
- [39] Hey, J. et al. "Doppler broadening and magnetic field effects on the balmer lines emitted at the edge of a tokamak plasma". *Contributions to Plasma Physics* **36**.5 (1996), pp. 583–604.
- [40] Huard, C. M. et al. "Role of neutral transport in aspect ratio dependent plasma etching of three-dimensional features". *Journal of Vacuum Science & Technology A: Vacuum, Surfaces, and Films* **35**.5 (2017), p. 05C301.
- [41] Karkari, S. et al. "Direct measurement of spatial electron density oscillations in a dual frequency capacitive plasma". *Applied Physics Letters* **93**.7 (2008), p. 071501.

- [42] Kinoshita, T. et al. "Notching as an example of charging in uniform high density plasmas". *Journal of Vacuum Science & Technology B: Microelectronics and Nanometer Structures Processing, Measurement, and Phenomena* **14**.1 (1996), pp. 560–565.
- [43] Kiss, L. D. B. & Sawin, H. H. "Evaluation of CF 4 plasma chemistry by power modulation". *Plasma chemistry and plasma processing* **12**.4 (1992), pp. 523–549.
- [44] Kiss, L. D. B. & Sawin, H. H. "Power modulation study of chemical kinetics in rf discharges". *Plasma chemistry and plasma processing* **12**.4 (1992), pp. 495–522.
- [45] Koo, B.-W. et al. "Langmuir probe in low temperature, magnetized plasmas: Theory and experimental verification". *Journal of applied physics* **86**.3 (1999), pp. 1213–1220.
- [46] Kota, G. P. et al. "The recombination of chlorine atoms at surfaces". *Journal of Vacuum Science & Technology A: Vacuum, Surfaces, and Films* **16**.1 (1998), pp. 270–277.
- [47] Kota, G. P. et al. "Heteronuclear and homonuclear surface abstraction reactions of Cl, Br, and F". *Journal of applied physics* **85**.1 (1999), pp. 74–86.
- [48] Kovacs, I. "Formulae for rotational intensity distribution of triplet transitions in diatomic molecules". *The Astrophysical Journal* **145** (1966), p. 634.
- [49] Kovács, I. & Nemes, L. *Rotational structure in the spectra of diatomic molecules*. Hilger London, 1969.
- [50] Kramida, A. et al. NIST Atomic Spectra Database (ver. 5.5.2), [Online]. Available: <https://physics.nist.gov/asd> [2018, February 13]. National Institute of Standards and Technology, Gaithersburg, MD. 2018.
- [51] Küllig, C et al. "Detachment-induced electron production in the early afterglow of pulsed cc-rf oxygen plasmas". *Physics of Plasmas* **19**.7 (2012), p. 073517.
- [52] Laux, C. O. & Kruger, C. H. "Arrays of radiative transition probabilities for the N<sub>2</sub> first and second positive, NO beta and gamma, N+ 2 first negative, and O<sub>2</sub> Schumann-Runge band systems". *Journal of Quantitative Spectroscopy and Radiative Transfer* **48**.1 (1992), pp. 9–24.
- [53] Lieberman, M. A. & Ashida, S. "Global models of pulse-power-modulated high-density, low-pressure discharges". *Plasma Sources Science and Technology* **5**.2 (1996), p. 145.
- [54] Lieberman, M. A., Lichtenberg, A. J., et al. *Principles of plasma discharges and materials processing*. Vol. 2. Wiley Online Library, 2005.
- [55] Lobbia, R. B. & Gallimore, A. D. "Temporal limits of a rapidly swept Langmuir probe". *Physics of Plasmas* **17**.7 (2010), p. 073502.

- [56] Ma, T. et al. "Recombination coefficients for Cl on plasma-conditioned yttrium oxide chamber wall surfaces". *Journal of Applied Physics* **125**.2 (2019), p. 023301.
- [57] Macko, P et al. "Study of oxygen atom recombination on a Pyrex surface at different wall temperatures by means of time-resolved actinometry in a double pulse discharge technique". *Plasma Sources Science and Technology* **13**.2 (2004), p. 251.
- [58] Malyshev, M. et al. "Dynamics of pulsed-power chlorine plasmas". *Journal of applied physics* **86**.9 (1999), pp. 4813–4820.
- [59] Marinov, D. et al. "Deterministic and Monte Carlo methods for simulation of plasma-surface interactions". *Plasma Processes and Polymers* **14**.1-2 (2017), p. 1600175.
- [60] Miller, P. A. et al. "An inductively coupled plasma source for the gaseous electronics conference RF reference cell". *Journal of research of the National Institute of Standards and Technology* **100**.4 (1995), p. 427.
- [61] Mulliken, R. S. "Report on notation for spectra of diatomic molecules". *Physical Review* **36**.4 (1930), p. 611.
- [62] Olthoff, J. K. & Greenberg, K. "The gaseous electronics conference RF reference cellâĂŤAn introduction". *Journal of research of the National Institute of Standards and Technology* **100**.4 (1995), p. 327.
- [63] Ono, K. & Tuda, M. "Dynamics of plasma-surface interactions and feature profile evolution during pulsed plasma etching". *Thin Solid Films* **374**.2 (2000), pp. 208–216.
- [64] Overzet, L. J. "Microwave diagnostic results from the gaseous electronics conference RF reference cell". *Journal of research of the National Institute of Standards and Technology* **100**.4 (1995), p. 401.
- [65] Overzet, L. J. & Kleber, J. "Effect of metastable atom reactions on the electron energy probability functions in afterglows". *Plasma Sources Science and Technology* **7**.4 (1998), p. 512.
- [66] Panarese, A et al. "A Monte Carlo model for determination of binary diffusion coefficients in gases". *Journal of Computational Physics* **230**.14 (2011), pp. 5716–5721.
- [67] Peterson, D. J. et al. "Electron neutral collision frequency measurement with the hairpin resonator probe". *Plasma Sources Science and Technology* **26**.9 (2017), p. 095002.
- [68] Piejak, R. et al. "The hairpin resonator: A plasma density measuring technique revisited". *Journal of Applied Physics* **95**.7 (2004), pp. 3785–3791.
- [69] Piejak, R. et al. "Hairpin resonator probe measurements in RF plasmas". *Plasma Sources Science and Technology* **14**.4 (2005), p. 734.

- [70] Piejak, R. et al. "Hairpin resonator probe measurements in RF plasmas". *Plasma Sources Science and Technology* **14**.4 (2005), p. 734.
- [71] Press, W. H. et al. *Numerical recipes 3rd edition: The art of scientific computing*. Cambridge university press, 2007.
- [72] Ramamurthi, B. & Economou, D. J. "Two-dimensional pulsed-plasma simulation of a chlorine discharge". *Journal of Vacuum Science & Technology A: Vacuum, Surfaces, and Films* **20**.2 (2002), pp. 467–478.
- [73] Richards, A. D. & Sawin, H. H. "Atomic chlorine concentration measurements in a plasma etching reactor. II. A simple predictive model". *Journal of applied physics* **62**.3 (1987), pp. 799–807.
- [74] Riemann, K. "Plasma and sheath". *Plasma Sources Science and Technology* **18**.1 (2008), p. 014006.
- [75] Rousseau, A et al. "Surface recombination of hydrogen atoms studied by a pulsed plasma excitation technique". *Journal of Applied Physics* **89**.4 (2001), pp. 2074–2078.
- [76] Roux, F et al. "High-resolution Fourier spectrometry of  ${}^{14}\text{N}_2$ : analysis of the (0–0),(0–1),(0–2),(0–3) bands of the C  $3\text{P}u$ –B  $3\text{P}g$  system". *Canadian Journal of Physics* **67**.2-3 (1989), pp. 143–147.
- [77] Samukawa, S. et al. "Pulse-time-modulated electron cyclotron resonance plasma discharge for highly selective, highly anisotropic, and charge-free etching". *Journal of Vacuum Science & Technology A: Vacuum, Surfaces, and Films* **14**.6 (1996), pp. 3049–3058.
- [78] Sands, B. L. et al. "Design and measurement considerations of hairpin resonator probes for determining electron number density in collisional plasmas". *Plasma Sources Science and Technology* **16**.4 (2007), p. 716.
- [79] Schulze, J et al. "Phase resolved optical emission spectroscopy: a non-intrusive diagnostic to study electron dynamics in capacitive radio frequency discharges". *Journal of Physics D: Applied Physics* **43**.12 (2010), p. 124016.
- [80] Sirse, N et al. "Probing negative ion density and temperature using a resonance hairpin probe". *Plasma Sources Science and Technology* **24**.2 (2015), p. 022001.
- [81] Stenzel, R. "Microwave resonator probe for localized density measurements in weakly magnetized plasmas". *Review of Scientific Instruments* **47**.5 (1976), pp. 603–607.
- [82] Stenzel, R. "High-frequency instability of the sheath–plasma resonance". *Physics of Fluids B: Plasma Physics* **1**.11 (1989), pp. 2273–2282.

- [83] Takayama, K. et al. "Plasma Resonance in a Radio-Frequency Probe". *Phys. Rev. Lett.* **5** (6 1960), pp. 238–240.
- [84] Terman, F. E. "Radio engineers' handbook" (1943).
- [85] Tokashiki, K. et al. "Synchronous Pulse Plasma Operation upon Source and Bias Radio Frequencies for Inductively Coupled Plasma for Highly Reliable Gate Etching Technology". *Japanese Journal of Applied Physics* **48**.8S1 (2009), 08HD01.
- [86] Touzeau, M et al. "Spectroscopic temperature measurements in oxygen discharges". *Journal of Physics D: Applied Physics* **24**.1 (1991), p. 41.
- [87] Vempaire, D & Cunge, G. "Probing radical kinetics in the afterglow of pulsed discharges by absorption spectroscopy with light emitting diodes: Application to BCl radical". *Applied Physics Letters* **94**.2 (2009), p. 021504.
- [88] Walsh, J. L. & Kong, M. G. "Room-temperature atmospheric argon plasma jet sustained with submicrosecond high-voltage pulses". *Applied Physics Letters* **91**.22 (2007), p. 221502.
- [89] Wang, Q. et al. "Experimental and theoretical study of the effect of gas flow on gas temperature in an atmospheric pressure microplasma". *Journal of Physics D: Applied Physics* **40**.14 (2007), p. 4202.
- [90] Warne, L. K. et al. *Model for resonant plasma probe*. Tech. rep. Sandia National Laboratories, 2007.
- [91] Wickramanayaka, S. et al. "Variation of the recombination coefficient of atomic oxygen on Pyrex glass with applied RF power". *Japanese journal of applied physics* **30**.11R (1991), p. 2897.
- [92] Wickramanayaka, S. et al. "Variation of the recombination coefficient of atomic oxygen on Pyrex glass with applied RF power". *Japanese journal of applied physics* **30**.11R (1991), p. 2897.
- [93] Yuan, Q. et al. "Effect of low-frequency power on dual-frequency capacitively coupled plasmas". *Journal of Physics D: Applied Physics* **41**.20 (2008), p. 205209.
- [94] Zhang, Q. et al. "Determination of vibrational and rotational temperatures in highly constricted nitrogen plasmas by fitting the second positive system of N<sub>2</sub> molecules". *AIP Advances* **5**.5 (2015), p. 057158.
- [95] Zhao, T.-L. et al. "Determination of vibrational and rotational temperatures in a gliding arc discharge by using overlapped molecular emission spectra". *Journal of Physics D: Applied Physics* **46**.34 (2013), p. 345201.
- [96] Zyrjanov, S. & Lopaev, D. "Measurements of the gas temperature in an oxygen plasma by spectroscopy of the O 2 (b 1 Σ g+) → O 2 (X 3 Σ g-) transition". *Plasma Physics Reports* **33**.6 (2007), pp. 510–520.

## **APPENDICES**

## APPENDIX

A

# ROTATIONAL TEMPERATURE SIMULATION

```
1 %%%This code simulates the rovibrational bands of the second positive N2
2 %%%system, the v'-v" (0-0) transition
3 %%%Output is rotational temperatures with error bar
4
5 clear all
6 %Raw data to be read, 1st column is wavelength (nm), 2nd set of ...
    columns is
```

```

7 %intensity, 3rd set of columns is reference, and last column is ...
8 %is required that the data have a variable called 'alldata' which contains
9 %that format. an example would be 1000x10 for 1000 wavelength data points
10 mat_title = 'testdata.mat';
11 load(mat_title);
12
13 num_bootstrap=10; %number of times you want to re-simulate the T_r to ...
14 % get simulation error
15
16 % labeling the input data
17 [row col] = size(alldata);
18 expt_lam = alldata(:,1);
19 expt_int = alldata(:,2:(col-2)/2+1);
20 expt_ref = alldata(:,(col-2)/2+2:col-1);
21 sigma = alldata(:,col);
22 rel_expt_err = sigma./ (mean(expt_int,2)-mean(expt_ref,2));
23
24 % find the indices for truncating the data to the (0,0) v',v" transition
25 left = find(abs(expt_lam-335.7)<0.005);
26 right = find(abs(expt_lam-337.3)<0.005);
27 expt_lam = expt_lam(left:right,:);
28 expt_int = expt_int(left:right,:);
29 sigma = sigma(left:right,:);
30
31 %Total number of rotational lines for each PQR branch could change J's ...
32 %but recommend 40.
33 Jmax = 40;
34 %Rotational temperatures to attempt. The script will change the ...
35 %T-rotation limits if convergence isn't found
36 T_rotation = linspace(400,550,76);% in K

```

```

34
35 %% SCALING FACTORS %%
36 fwhm = 0.025; %fwhm on Echelle, nm
37 gauss_sig = fwhm/(2*(2*log(2))^0.5);
38
39 %% CONSTANTS %%
40 k_b = 1.38E-23; % Boltzman constant (J/K)
41 c = 3.0*10^8; % speed of light (m/s)
42 h = 6.626070*10^-34; % planks constant in (J*s)
43 q_franck = 0.4515; %Franck-Condon factor
44
45
46 %Rotational C3pi_u constants are in 1st column, B3pi_g in second
47 %These are from Roux 1988, https://doi.org/10.1139/p89-023
48 Bv = [1.8153 1.62872]; %(cm-1)
49 A = [39.134 42.234]; %(cm-1)
50 Y = A./Bv;
51 Dv = [0.595E-5 0.581E-5]; %(cm-1) called 'D' in Roux paper but Dv in ...
      textbooks
52 waveorigin = 29670.942; %the (0-0) transition origin from Roux 1988 (cm-1)
53
54 %Rotational wavenumber calculations from Budo 1933, reproduced in
55 %Herzberg's Spectra of Diatomic Molecules Vol.1 pg 235
56 for J=0:Jmax
57   for i=1:2
58     jay = J+1;
59     Z1 = Y(i)*(Y(i)-4)+4/3+4*J*(J+1);
60     Z2 = 1/3/Z1*(Y(i)*(Y(i)-1)-4/9-2*J*(J+1));
61     F1(jay,i)=Bv(i)*(J*(J+1)-Z1^0.5-2*Z2)-Dv(i)*(J-1/2)^4;
62     F2(jay,i)=Bv(i)*(J*(J+1)+4*Z2)-Dv(i)*(J+1/2)^4;
63     F3(jay,i)=Bv(i)*(J*(J+1)+Z1^0.5-2*Z2)-Dv(i)*(J+3/2)^4;

```

```

64      %F1,2,3 are now wavenumbers for the B state in column2, C in ...
65      %column1
66      %F(1,i) is F(J=0,i) and F(Jmax+1,i) is F(J=40)
67  end
68
69 jaymax=Jmax+1;
70 %Calculating difference in term values for the wavelength origins
71 wave_p1 = F1(3:jaymax-1,1)-F1(4:jaymax,2);
72 wave_p2 = F2(3:jaymax-1,1)-F2(4:jaymax,2);
73 wave_p3 = F3(3:jaymax-1,1)-F3(4:jaymax,2);
74 waveP = [wave_p1;wave_p2;wave_p3]+waveorigin; %waveorigin is the bandhead
75 lamP = waveP.^-1*10^7; %conversion to nm
76
77 wave_q1 = F2(3:jaymax,1)-F2(3:jaymax,2);
78 wave_q2 = F3(2:jaymax,1)-F3(2:jaymax,2);
79 waveQ = [wave_q1;wave_q2]+waveorigin;
80 lamQ = waveQ.^-1*10^7;
81
82 wave_r1 = F1(2:jaymax,1)-F1(1:jaymax-1,2);
83 wave_r2 = F2(3:jaymax,1)-F2(2:jaymax-1,2);
84 wave_r3 = F3(4:jaymax,1)-F3(3:jaymax-1,2);
85 waveR = [wave_r1;wave_r2;wave_r3]+waveorigin;
86 lamR = waveR.^-1*10^7;
87 %Combining the P,Q,R branches into one simulated lambda vector
88 lambda=[lamP;lamQ;lamR];
89
90
91 %Line Strength factors from Kovacs 1969 pg 132
92 %u and C expressions
93 Jvec = linspace(0,jaymax,Jmax+2)';

```

```

94 why = Y; %Making Y single valued so this is easier to debug
95 Y=Y(1);
96
97 %Calculating the C state constants
98 u1(:,1) = (Y*(Y-4)+4*Jvec.^2).^0.5;
99 u3(:,1) = (Y*(Y-4)+4*(Jvec+1).^2).^0.5;
100 C1(:,1) = Y*(Y-4)*Jvec.* (Jvec+1) + 2*(2*Jvec+1).* (Jvec-1).* Jvec.* (Jvec+1);
101 C2(:,1) = Y*(Y-4) + 4*Jvec.* (Jvec+1);
102 C3(:,1) = Y*(Y-4)*(Jvec-1).* (Jvec+2) + ...
              2*(2*Jvec+1).* Jvec.* (Jvec+1).* (Jvec+2);
103 u1_plus(:,1) = u1(:,1)+(Y-2);
104 u1_minus(:,1) = u1(:,1)-(Y-2);
105 u3_plus(:,1) = u3(:,1)+(Y-2);
106 u3_minus(:,1) = u3(:,1)-(Y-2);
107
108 %Switching Y to Y(B state) and calculating those constants
109 Y = why(2);
110 u1(:,2) = (Y*(Y-4)+4*Jvec.^2).^0.5;
111 u3(:,2) = (Y*(Y-4)+4*(Jvec+1).^2).^0.5;
112 C1(:,2) = Y*(Y-4)*Jvec.* (Jvec+1) + 2*(2*Jvec+1).* (Jvec-1).* Jvec.* (Jvec+1);
113 C2(:,2) = Y*(Y-4) + 4*Jvec.* (Jvec+1);
114 C3(:,2) = Y*(Y-4)*(Jvec-1).* (Jvec+2) + ...
              2*(2*Jvec+1).* Jvec.* (Jvec+1).* (Jvec+2);
115 u1_plus(:,2) = u1(:,1)+(Y-2);
116 u1_minus(:,2) = u1(:,1)-(Y-2);
117 u3_plus(:,2) = u3(:,1)+(Y-2);
118 u3_minus(:,2) = u3(:,1)-(Y-2);
119
120 %Kovacs expressions, easier to work from the 1966 Paper where Lambda=1
121 %rather than the textbook which gives formulation for any Lambda. Note ...
               that

```

```

122 %this is the intermediate hund's coupling expression for the main P,Q,R
123 %lines. ie. P_1, P_2, P_3. Don't use the P_Q_12 stuff
124 %Note that J refers to the upper level, J', and jay must be used as an ...
125   index
126
127 %in order to get a J=0 calculation later.
128
129 Y=why;
130
131 for J = 2:Jmax-1
132
133   jay = J+1;
134
135   S_P1(jay) = (J-1)*(J+1)/(16*J*C1(jay-1,1)*C1(jay,2)) * ...
136     (8*(J-2)*(J-1)*J*(J+1)+(J-2)*(J+2)*u1_minus(jay-1,1) * ...
137     u1_minus(jay,2)+J^2*u1_plus(jay-1,1)*u1_plus(jay,2))^2;
138
139   S_P2(jay) = (J-1)*(J+1)/(J*C2(jay-1,1)*C2(jay,2)) * ...
140     ((Y(1)-2)*(Y(2)-2)+2*((J-2)*(J+2)+J^2))^2;
141
142   S_P3(jay) = (J-1)*(J+1)/(16*J*C3(jay-1,1)*C3(jay,2)) * ...
143     (8*(J-1)*J*(J+1)*(J+2)+(J-2)*(J+2)*u3_plus(jay-1,1) * ...
144     u3_plus(jay,2)+J^2*u3_minus(jay-1,1)*u3_minus(jay,2))^2;
145
146 end
147
148
149 S_P1 = S_P1(3:jaymax-1);
150 S_P2 = S_P2(3:jaymax-1);
151 S_P3 = S_P3(3:jaymax-1);
152
153
154 for J=1:Jmax
155   jay=J+1;
156
157   S_Q1(jay) = (J-1)^2*(2*J+1)/(4*J*(J+1)*C1(jay,1)*C1(jay,2)) * ...
158     (4*(J-1)*(J+1)^2+(J+2)*u1_minus(jay)*u1_minus(jay,2))^2;
159
160   S_Q2(jay) = (2*J+1)/(J*(J+1)*C2(jay,1)*C2(jay,2)) * ...
161     ((Y(1)-2)*(Y(2)-2)+2*((J-2)*(J+2)+J^2))^2;
162
163 end

```

```

145 S_Q1 = S_Q1(3:jaymax);
146 S_Q2 = S_Q2(2:jaymax);
147
148 for J=1:Jmax
149     jay=J+1;
150     S_R1(jay) = J*(J+2)/(16*(J+1)*C1(jay+1,1)*C1(jay,2)) * ...
151                 (8*(J-1)*J*(J+1)*(J+2)+(J-1)*(J+3)*u1_minus(jay+1,1) * ...
152                 u1_minus(jay,2)+(J+1)^2*u1_plus(jay+1,1)*u1_plus(jay,2))^2;
153     S_R2(jay) = J*(J+2)/((J+1)*C2(jay+1,1)*C2(jay,2)) * ...
154                 ((Y(1)-2)*(Y(2)-2)+2*((J-1)*(J+3)+(J+1)^2))^2;
155     S_R3(jay) = J*(J+2)/(16*(J+1)*C3(jay+1,1)*C3(jay,2)) * ...
156                 (8*J*(J+1)*(J+2)*(J+3)+(J-1)*(J+3)*u3_plus(jay+1,1) * ...
157                 u3_plus(jay,2)+(J+1)^2*u3_minus(jay+1,1)*u3_minus(jay,2))^2;
158
159
160 S_R1 = S_R1(2:jaymax);
161 S_R2 = S_R2(3:jaymax);
162 S_R3 = S_R3(4:jaymax);
163
164
165 timestep = 1;
166
167 %randomly select intensity and reference sets then generate new spectra
168 %called 'signal'
169 int_resample = randi([1 (col-2)/2],1,num_bootstrap);
170 ref_resample = randi([1 (col-2)/2],1,num_bootstrap);

```

```

171 for i=1:num_bootstrap
172     signal(:,i)=expt_int(:,int_resample(i))-expt_ref(:,ref_resample(i));
173 end
174
175 for boot = 1:num_bootstrap
176
177     boot_int = signal(:,boot);
178
179     for iteration = 1:length(T_rotation)
180
181         %%% TEMPERATURES %%%
182         T_rot = T_rotation(iteration); % in K
183
184         %multiplication factor for F in exp(F/k_B/T_r) expression. ...
185
186         % Note that THIS
187         %is what is changing between iterations to fit T_r. 100 factor ...
188
189         %is to change
190
191         %from cm^-1 to m^-1 and work with the h,c constants
192         mult = -100*c*h/k_b/T_rot;
193
194
195         expP1 = exp(F1(3:jaymax-1,1)*mult);
196         expP2 = exp(F2(3:jaymax-1,1)*mult);
197         expP3 = exp(F3(3:jaymax-1,1)*mult);
198
199         expQ1 = exp(F2(3:jaymax,1)*mult);
200         expQ2 = exp(F3(2:jaymax,1)*mult);
201
202         expR1 = exp(F1(2:jaymax,1)*mult);
203         expR2 = exp(F2(3:jaymax,1)*mult);
204         expR3 = exp(F3(4:jaymax,1)*mult);

```

```

200     exponent = [expP1; expP2; expP3; expQ1; expQ2; expR1; expR2; ...
201         expR3];
202
202     Int_stems = 1./lambda.^4*q_franck.*S_all.*exponent;
203     dim = length(lambda); %size of the 'pure line' spectrum
204     data_size = length(boot_int);
205
206     %Fitting an oversampled simulation (higher resolution)
207     Int_10xfinal = zeros(data_size*10,1);
208     tenxlam = linspace(expt_lam(1),expt_lam(data_size),data_size*10)';
209
210     %Summing together all the Gaussians for every single line
211     for i = 1:data_size*10
212         for j = 1:dim-1
213             Int_10xfinal(i) = Int_10xfinal(i) + ...
214                 Int_stems(j)*normpdf(tenxlam(i),lambda(j),gauss_sig);
215         end
216     end
217     Int_10xfinal = Int_10xfinal/max(Int_10xfinal)*max(boot_int);
218
219
220     %shift the simulated data in the x-axis to get alignment at the
221     %intensity maxima for simulation and experiment
222     [discard, index] = max(Int_10xfinal);
223     [discard, expt_index] = max(boot_int);
224     shift= tenxlam(index)-expt_lam(expt_index); %shift in nm
225     % shift = 0; %testing out no shift
226     expt_lam_final = expt_lam+shift;
227
228     %Interpolate and find error for simulation

```

```

229     y_sim = interp1(tenxlam, Int_10xfinal, expt_lam_final);
230     y_sim(isnan(y_sim))=0; %remove NaN results from interpolation ...
231
232     function
233         chi_error(iteration) = sum(((y_sim-boot_int)./sigma)).^2;
234         relative_err(iteration) = sum(abs(y_sim-boot_int)./boot_int);
235         allshift(iteration) = shift;
236         all_expt_lam(:,iteration) = expt_lam_final;
237
238     end
239
240 %select best simulation and check if chi is minimized at the limit.
241 %If so, change T_rotation limits and rerun simulations to find min
242 [discard best_iteration] = min(chi_error);
243 if best_iteration == 1
244     T_rotation=T_rotation-150;
245     boot=boot-1;
246 elseif best_iteration == length(T_rotation)
247     T_rotation = T_rotation+150;
248     boot=boot-1;
249 else
250     bootstrap_temp(boot) = T_rotation(best_iteration);
251 end
252
253 if T_rotation(best_iteration) > 1000
254     temperature_limit_exceeded
255 end
256
257 end
258

```

```

259
260 %Average the bootstrap temperature results, find the simulation error
261 final_Tr = mean(bootstrap_temp(find(bootstrap_temp)));
262 rel_sim_err = std(bootstrap_temp(find(bootstrap_temp)))/final_Tr;
263 overallerr = sqrt(mean(rel_expt_err)^2+rel_sim_err^2)*final_Tr;
264 bestsimulation_int = all_int_final(:,best_iteration);
265
266 %Plot the chi-squared vs temperature for last run
267 figure();
268 plot(T_rotation,chi_error,'o')
269 title('Test Statistic vs. Simulation Temperature')
270 ylabel('\chi^2 (unitless)')
271 xlabel('T_r (K)')
272
273
274 %Plot the bootstrap results
275 figure();
276 plot(bootstrap_temp)
277 xlabel('Bootstrap Iteration Number')
278 ylabel('T_r Result')
279
280 % %Plot the relative error of the experimental data
281 % figure();
282 % plot(alldata(:,1),rel_expt_err,'ro')
283 % ylabel('Sigma/Avg_I (%)')
284 % xlabel('Wavelength (nm)')
285 % title('Experimental Error')
286
287 %Plot the shifted experimental data and the simulation lines
288 % figure()
289 % plot(expt_lam_final,expt_int,'r',sim_lam,Int_final,'b')

```

```

290 % title(strcat('T_r=', num2str(T_rot), ' FWHM=', num2str(fwhm)))
291 % legend('Experiment','Simulation')
292 % ylabel('Intensity (a.u.)')
293 % xlabel('Wavelength (nm)')
294 % xlim([334 337.5])
295
296 %plot unshifted data
297 % figure()
298 % plot(expt_lam,expt_int,'r',sim_lam,Int_final,'b')
299 % title(strcat('T_r=', num2str(T_rot), ' FWHM=', num2str(fwhm)))
300 % legend('Experiment','Simulation')
301 % ylabel('Intensity (a.u.)')
302 % xlabel('Wavelength (nm)')
303 % xlim([335.5 337.5])
304
305
306 % % Plot all the simulation lines
307 % figure()
308 % stem(lambda,Int_stems,'.')
309 % xlim([335.5 337.5])
310 % title(strcat('Pure Simulation Lines Tr=', num2str(T_rot)))
311 % ylabel('Intensity (a.u.)')
312 % xlabel('Wavelength (nm)')

```

## APPENDIX

B

# TIME RESOLVED HAIRPIN PROBE ANALYSIS

```
1 # -*- coding: utf-8 -*-
2 """
3 Created on Sat Mar 31 19:32:04 2018
4
5 @author: David Peterson, Kris Ford
6 """
7
8 #-----
```

```

9  #      Save data from a DPO5104 Tektronix oscilloscope using GPIB or USB
10 #      Determine vacuum resonant frequency, steady state resonant ...
11 #          frequency, and pulsed resonant frequency (time dependent)
12 #      Determine steady state and time dependent electron densit for a ...
13 #          hairpin resonator probe
14 #
15 #
16 #
17 #
18 #-----
19
20 import visa
21 import numpy as np
22 from struct import unpack
23 import matplotlib.pyplot as plt
24 from scipy.fftpack import fft
25 import pylab
26 #import peakutils
27 import pandas as pd
28 import sys, os
29 sys.path.append('C:\\\\Users\\\\lab-admin\\\\.spyder-py3')
30 import synth
31 from synth import synth
32 from scipy.optimize import curve_fit
33 from scipy import optimize
34 from scipy import stats
35 #####
36
37

```

```

38 ## Measure transmission line reference, save the reference data. You ...
39 # have to find your vacuum
40
41 ##### User defined Data
42 reference_title = "C:\\Users\\lab-admin\\Desktop\\Hairpin Spike ...
43 # Data\\1858MHz Full Sweep pt1MHZ steps.npy"
44 freqstart = 1840 #starting frequency in MHz for vacuum resonance
45 freqstopvac = 1875 #stopping frequency in MHz for vacuum resonance
46 freqstop = 4400 #Stopping frequency for reference sweep
47 freqstep = .1 #step in frequency in MHz
48 freqdelay = 2 #time delay for changing frequency in seconds
49
50 ##### End User defined Data
51
52 numsteps = int((freqstopvac-freqstart)/freqstep)
53 ref_sweep_offset = 0
54 frequency = np.linspace(freqstart,freqstopvac,numsteps,endpoint=False)
55
56 S1= synth("AH01SZGB")
57 S1.syn_cmd("clkint")
58 S1.syn_cmd("setpwr 10")
59 S1.syn_cmd("setfreqfrom" + " " + str(freqstart))
60 S1.syn_cmd("setfreqto" + " " + str(freqstopvac))
61 S1.syn_cmd("setfreqstep" + " " + str(freqstep))
62 S1.syn_cmd("setfreqdelay" + " " + str(freqdelay))
63 S1.syn_cmd("freqstep")
64
65 rm = visa.ResourceManager()
66 print(rm.list_resources())
67 ports = rm.list_resources()

```

```

66 #Replace this with code that determines if device is GPIB or USB ...
       connected and selects appropriate port name
67 scope = rm.open_resource('GPIB0::1::INSTR') #Currently assumes GPIB ...
       connection, will be made flexible to detect both GPIB and USB
68
69 scope.write('DATA:SOU CH4') #set channel to take data from
70 scope.write('DATA:START 0')
71 scope.write('DATA:STOP 1E5')
72 scope.write('DATA:WIDTH 1')
73 scope.write('DATA:ENC RPB')
74
75 ymult = float(scope.ask('WFMPRE:YMULT?'))
76 yzero = float(scope.ask('WFMPRE:YZERO?'))
77 yoff = float(scope.ask('WFMPRE:YOFF?'))
78 xincr = float(scope.ask('WFMPRE:XINCR?'))
79
80 #Take sample data set to get number of data points
81 scope.write('CURVE?')
82 data = scope.read_raw()
83 headerlen = 2 + int(data[1])
84 header = data[:headerlen]
85 ADC_wave = data[headerlen:-1]
86 ADC_wave = np.array(unpack('%sB' % len(ADC_wave), ADC_wave))
87 Volts = (ADC_wave - yoff) * ymult + yzero
88 Time = np.arange(0, xincr * len(Volts), xincr)
89
90 Raw_Reflected_Voltage = np.zeros((len(frequency), len(Volts)))
91
92 for i in range(0,len(frequency)):
93     scope.write('CURVE?')
94     data = scope.read_raw()

```

```

95     headerlen = 2 + int(data[1])
96     header = data[:headerlen]
97     ADC_wave = data[headerlen:-1]
98
99     ADC_wave = np.array(unpack('>%dB' % len(ADC_wave), ADC_wave))
100
101    Volts = (ADC_wave - yoff) * ymult + yzero
102
103    Raw_Reflected_Voltage[i] = Volts
104    S1.syn_cmd("freqstep")
105
106
107 S1.syn_cmd("stop")
108 S1.syn_close()
109
110
111 #Data Analysis
112 Reflected_Voltage_Averaged = np.average(Raw_Reflected_Voltage, axis=1)
113 Vacuum_Resonant_Frequency = ...
114     frequency[Reflected_Voltage_Averaged.argmin()] #determines vacuum ...
115     resonant frequency using minimum reflected voltage
116 pylab.plot(frequency, Reflected_Voltage_Averaged)
117 pylab.show()
118
119 def lorentz(x, *p):
120     I, gamma, x0, bg = p
121     return I * gamma**2 / ((x - x0)**2 + gamma**2) + bg
122
123 def fit(p, x, y):
124     return curve_fit(lorentz, x, y, p0 = p)

```

```

124 # coefficient of determination
125 def calc_r2(y, f):
126     avg_y = y.mean()
127     sstot = ((y - avg_y)**2).sum()
128     ssres = ((y - f)**2).sum()
129     return 1 - ssres/sstot
130
131 params = np.array([0.15, 1, Vacuum_Resonant_Frequency, 0.1], ...
132                     dtype=np.double)    #fit guess, hwhm in MHz
133 solp, ier = fit(params, frequency, Reflected_Voltage_Averaged)
134 Vacuum_Resonant_Frequency_Fit = solp[2]
135 Vacuum_fwhm = 2*abs(solp[1])
136 Vacuum_Fit = lorentz(frequency, *solp)
137
138 Q_Vacuum = Vacuum_Resonant_Frequency_Fit/Vacuum_fwhm
139
140 pylab.plot(frequency, Reflected_Voltage_Averaged, frequency, Vacuum_Fit)
141 pylab.show()
142
143 r2_vacuum = calc_r2(Reflected_Voltage_Averaged, Vacuum_Fit)
144
145 print("Q Vacuum = " + str(Q_Vacuum))
146 print("fv = " + str(Vacuum_Resonant_Frequency_Fit))
147
148 #Reference sweep (can also be a calibration sweep, but need to make ...
149 #           into separate cell)
150 freqstart = int(Vacuum_Resonant_Frequency) + ref_sweep_offset ...
151                     #starting frequency in MHz
152 numsteps = int((freqstop-freqstart)/freqstep)
153 frequency = np.linspace(freqstart,freqstop,numsteps,endpoint=False)
154
155
```

```

152 S1= synth("AH01SZGB")
153 S1.syn_cmd("clkint")
154 S1.syn_cmd("setpwr 10")
155 S1.syn_cmd("setfreqfrom" + " " + str(freqstart))
156 S1.syn_cmd("setfreqto" + " " + str(freqstop))
157 S1.syn_cmd("setfreqstep" + " " + str(freqstep))
158 S1.syn_cmd("setfreqdelay" + " " + str(freqdelay))
159 S1.syn_cmd("freqstep")
160
161 scope.write('CURVE?')
162 data = scope.read_raw()
163 headerlen = 2 + int(data[1])
164 header = data[:headerlen]
165 ADC_wave = data[headerlen:-1]
166 ADC_wave = np.array(unpack('%sB' % len(ADC_wave),ADC_wave))
167 Volts = (ADC_wave - yoff) * ymult + yzero
168 Time = np.arange(0, xincr * len(Volts), xincr)
169
170 Ref_Reflected_Voltage = np.zeros((len(frequency), len(Volts)))
171
172 for i in range(0,len(frequency)):
173     scope.write('CURVE?')
174     data = scope.read_raw()
175     headerlen = 2 + int(data[1])
176     header = data[:headerlen]
177     ADC_wave = data[headerlen:-1]
178
179     ADC_wave = np.array(unpack('%sB' % len(ADC_wave),ADC_wave))
180
181     Volts = (ADC_wave - yoff) * ymult + yzero
182

```

```

183     Ref_Reflected_Voltage[i] = Volts
184     S1.syn_cmd("freqstep")
185
186 S1.syn_cmd("stop")
187 S1.syn_close()
188
189 Ref_Reflected_Voltage_Averaged = np.average(Ref_Reflected_Voltage, ...
190     axis=1) #Reference reflected voltage to be used in steady state ...
191     electron density determinatoin
192 Ref_Reflected_Voltage_Averaged[0] = Ref_Reflected_Voltage_Averaged[1] ...
193     #avoids weird zero error
194
195 pylab.subplots()
196 pylab.plot(frequency, Ref_Reflected_Voltage_Averaged, 'ro')
197 pylab.xlabel('MHz')
198 pylab.ylabel('Voltage')
199 pylab.show()
200
201
202
203 #####
204 ## Determine vacuum resonant frequency, which might have shifted, and ...
205     choose which reference to load
206 ##The reference file MUST be a .npy to work, as the code manipulates ...
207     tuples later
208 #####
209

```

```

208 reference_load_title = "C:\\\\Users\\\\lab-admin\\\\Desktop\\\\Hairpin Spike ...  

209                                     Data\\\\1858MHz Full Sweep pt1MHZ steps.npy"  

210  

211 data_in = np.load(reference_load_title)  

212 freqstart = 1820      #starting frequency in MHz for vacuum resonance  

213 freqstop = 1900 #stopping frequency in MHz for vacuum resonance  

214 freqstep = 0.1 #step in frequency in MHz  

215 freqdelay = 2 #time delay for changing frequency in seconds  

216 numsteps = int((freqstop-freqstart)/freqstep)  

217  

218 frequency = np.linspace(freqstart,freqstop,numsteps,endpoint=False)  

219  

220 S1= synth("AH01SZGB")  

221 S1.syn_cmd("clkint")  

222 S1.syn_cmd("setpwr 10")  

223 S1.syn_cmd("setfreqfrom" + " " + str(freqstart))  

224 S1.syn_cmd("setfreqto" + " " + str(freqstop))  

225 S1.syn_cmd("setfreqstep" + " " + str(freqstep))  

226 S1.syn_cmd("setfreqdelay" + " " + str(freqdelay))  

227 S1.syn_cmd("freqstep")  

228  

229 rm = visa.ResourceManager()  

230 print(rm.list_resources())  

231 ports = rm.list_resources()  

232 #Replace this with code that determines if device is GPIB or USB ...  

233             connected and selects appropriate port name  

234 scope = rm.open_resource('GPIB0::1::INSTR') #Currently assumes GPIB ...  

235             connection, will be made flexible to detect both GPIB and USB  

236  

237 scope.write('DATA:SOU CH4') #set channel to take data from  

238 scope.write('DATA:START 0')

```

```

236 scope.write('DATA:STOP 1E5')
237 scope.write('DATA:WIDTH 1')
238 scope.write('DATA:ENC RPB')
239
240 ymult = float(scope.ask('WFMPRE:YMULT?'))
241 yzero = float(scope.ask('WFMPRE:YZERO?'))
242 yoff = float(scope.ask('WFMPRE:YOFF?'))
243 xincr = float(scope.ask('WFMPRE:XINCR?'))
244
245 #Take sample data set to get number of data points
246 scope.write('CURVE?')
247 data = scope.read_raw()
248 headerlen = 2 + int(data[1])
249 header = data[:headerlen]
250 ADC_wave = data[headerlen:-1]
251 ADC_wave = np.array(unpack('%sB' % len(ADC_wave), ADC_wave))
252 Volts = (ADC_wave - yoff) * ymult + yzero
253 Time = np.arange(0, xincr * len(Volts), xincr)
254
255 Raw_Reflected_Voltage = np.zeros((len(frequency), len(Volts)))
256
257 for i in range(0, len(frequency)):
258     scope.write('CURVE?')
259     data = scope.read_raw()
260     headerlen = 2 + int(data[1])
261     header = data[:headerlen]
262     ADC_wave = data[headerlen:-1]
263
264     ADC_wave = np.array(unpack('%sB' % len(ADC_wave), ADC_wave))
265
266     Volts = (ADC_wave - yoff) * ymult + yzero

```

```

267
268     Raw_Reflected_Voltage[i] = Volts
269     S1.syn_cmd("freqstep")
270
271
272 S1.syn_cmd("stop")
273 S1.syn_close()
274
275 #Data Analysis
276 pylab.subplots()
277 Reflected_Voltage_Averaged = np.average(Raw_Reflected_Voltage, axis=1)
278 Vacuum_Resonant_Frequency = ...
279     frequency[Reflected_Voltage_Averaged.argmin()] #determines vacuum ...
280     resonant frequency using minimum reflected voltage
281 pylab.plot(frequency, Reflected_Voltage_Averaged)
282 pylab.show()
283
284 def lorentz(x, *p):
285     I, gamma, x0, bg = p
286     return I * gamma**2 / ((x - x0)**2 + gamma**2) + bg
287
288 def fit(p, x, y):
289     return curve_fit(lorentz, x, y, p0 = p)
290
291 # coefficient of determination
292 def calc_r2(y, f):
293     avg_y = y.mean()
294     sstot = ((y - avg_y)**2).sum()
295     ssres = ((y - f)**2).sum()

```

```

296     return 1 - ssres/sstot
297
298 params = np.array([0.15, 1, Vacuum_Resonant_Frequency, 0.1], ...
299                 dtype=np.double)    #fit guess, hwhm in MHz
300 solp, ier = fit(params, frequency, Reflected_Voltage_Averaged)
301 Vacuum_Resonant_Frequency_Fit = solp[2]
302 Vacuum_fwhm = 2*abs(solp[1])
303 Vacuum_Fit = lorentz(frequency, *solp)
304
305
306 pylab.subplots()
307 pylab.plot(frequency, Reflected_Voltage_Averaged, frequency, Vacuum_Fit)
308 pylab.show()
309
310
311 r2_vacuum = calc_r2(Reflected_Voltage_Averaged, Vacuum_Fit)
312
313 print("Q Vacuum = " + str(Q_Vacuum))
314 print("R Squared = " + str(r2_vacuum))
315
316 #%%
317 ###
318 #This section measures the RF pickup on the cables to calibrate it out ...
319     and the RF waveform on the electrode
320
321 #####
322 scope.write('DATA:SOU CH4') #set channel to take data from
323 scope.write('DATA:START 0')
324 scope.write('DATA:STOP 1E5')

```

```

325 scope.write('DATA:WIDTH 1')
326 scope.write('DATA:ENC RPB')
327
328 ymult = float(scope.ask('WFMPRE:YMULT?'))
329 yzero = float(scope.ask('WFMPRE:YZERO?'))
330 yoff = float(scope.ask('WFMPRE:YOFF?'))
331 xincr = float(scope.ask('WFMPRE:XINCR?'))
332
333 scope.write('CURVE?')
334 data = scope.read_raw()
335 headerlen = 2 + int(data[1])
336 header = data[:headerlen]
337 ADC_wave = data[headerlen:-1]
338 ADC_wave = np.array(unpack('%sB' % len(ADC_wave), ADC_wave))
339 Volts = (ADC_wave - yoff) * ymult + yzero
340 RF_Pickup = Volts #Take 5 values and average
341 Time = np.arange(0, xincr * len(Volts), xincr)
342 while '1' in scope.ask("BUSY?"):
343     time.sleep(0.01)
344
345 ######
346 #This section measures the RF waveform on the electrode
347 #####
348
349 scope.write('DATA:SOU CH2') #set channel to take data from
350 scope.write('DATA:START 0')
351 scope.write('DATA:STOP 1E5')
352 scope.write('DATA:WIDTH 1')
353 scope.write('DATA:ENC RPB')
354
355 ymult = float(scope.ask('WFMPRE:YMULT?'))

```

```

356 yzero = float(scope.ask('WFMPRE:YZERO?'))
357 yoff = float(scope.ask('WFMPRE:YOFF?'))
358 xincr = float(scope.ask('WFMPRE:XINCR?'))
359
360
361 scope.write('CURVE?')
362 data = scope.read_raw()
363 headerlen = 2 + int(data[1])
364 header = data[:headerlen]
365 ADC_wave = data[headerlen:-1]
366 ADC_wave = np.array(unpack('%sB' % len(ADC_wave), ADC_wave))
367 Volts = (ADC_wave - yoff) * ymult + yzero
368 RF_Voltage = Volts
369 Time = np.arange(0, xincr * len(Volts), xincr)
370 while '1' in scope.ask("BUSY?"):
371     time.sleep(0.01)
372
373 #####
374 #Plot both measured quantities
375 #####
376 pylab.plot(Time, RF_Voltage, 'bo')
377 #pylab.axis([0, 0.2, -4, 4])
378 pylab.xlabel('Time [${\mu}s]$ ')
379 pylab.ylabel('Sample of RF Voltage on Electrode [V]')
380 #xticks(np.linspace(Time_micro[0],max(Time_micro),5))
381 pylab.show()
382
383 pylab.plot(Time, RF_Pickup, 'bo')
384 pylab.xlabel('Time [${\mu}s]$ ')
385 pylab.ylabel('RF Pickup from cables [V]')
386 #xticks(np.linspace(Time_micro[0],max(Time_micro),5))

```

```

387 pylab.show()

388

389

390 #%%

391

392

393 #####
394 ## Determine time resolved resonant frequency and electron density in ...
395      a pulsed plasma
396 #### note that the reference file should already be loaded in the ...
397      vacuum resonant section
398
399 #### User Defined Input
400 data_title = "C:\\\\Users\\\\lab-admin\\\\Desktop\\\\ExampleData.csv"
401
402 freqstart = 1865 #starting frequency in MHz
403 freqstop = 2090 #stopping frequency in MHz
404 reference_sweep_step = 0.1 #size of reference step
405 freqstep = 0.1 #Your frequency step MUST be a multiple of the ...
406      reference_sweep_step
407 #### End User Defined Input, unless you want to change power, synth ...
408      name, etc
409
410
411 numsteps = int((freqstop-freqstart)/freqstep)
412 frequency = np.linspace(freqstart,freqstop,numsteps, endpoint=False)
413 loading_jump_size = int(round(freqstep/reference_sweep_step)) #if this ...
414      equals 2, skip every other input from ref file, etc
415
416
417 #Build the reference data you need based on freqstart and freqstop,

```

```

413 full_ref_voltage = data_in[:,1]
414 full_ref_frequency = data_in[:,0]
415 start_index = np.where(full_ref_frequency==freqstart)
416 start_index = start_index[0][0] #If you get an "index 0 is out of ...
        bounds error'
417     #it's because you picked a frequency that isn't in the reference ...
        file, the search returned a blank tuple
418
419 Ref_Reflected_Voltage_Averaged = np.zeros(numsteps)
420 for i in range(0,numsteps):
421     Ref_Reflected_Voltage_Averaged[i] = ...
        full_ref_voltage[i*loading_jump_size+start_index]
422
423 #pylab.subplots()
424 #pylab.plot(frequency, Ref_Reflected_Voltage_Averaged, 'ro')
425 #pylab.xlabel('MHz')
426 #pylab.ylabel('Voltage')
427 #pylab.show()
428
429
430
431 S1= synth("AH01SZGB")
432 S1.syn_cmd("clkint")
433 S1.syn_cmd("setpwr 10")
434 S1.syn_cmd("setfreqfrom" + " " + str(freqstart))
435 S1.syn_cmd("setfreqto" + " " + str(freqstop))
436 S1.syn_cmd("setfreqstep" + " " + str(freqstep))
437 S1.syn_cmd("setfreqdelay" + " " + str(freqdelay))
438 S1.syn_cmd("freqstep")
439
440 rm = visa.ResourceManager()

```

```

441 print(rm.list_resources())
442 scope = rm.open_resource('GPIBO::1::INSTR')
443
444 scope.write('DATA:SOU CH4') #set channel to take data from
445 scope.write('DATA:START 0')
446 scope.write('DATA:STOP 1E5')
447 scope.write('DATA:WIDTH 1')
448 scope.write('DATA:ENC RPB')
449
450 ymult = float(scope.ask('WFMPRE:YMULT?'))
451 yzero = float(scope.ask('WFMPRE:YZERO?'))
452 yoff = float(scope.ask('WFMPRE:YOFF?'))
453 xincr = float(scope.ask('WFMPRE:XINCR?'))
454
455 #Take sample data set to get number of data points
456 #scope.write("ACQ:STOPA SEQ")
457 #scope.write("ACQ:STATE ON")
458
459
460 scope.write('CURVE?')
461 data = scope.read_raw()
462 headerlen = 2 + int(data[1])
463 header = data[:headerlen]
464 ADC_wave = data[headerlen:-1]
465 ADC_wave = np.array(unpack('%sB' % len(ADC_wave), ADC_wave))
466 Volts = (ADC_wave - yoff) * ymult + yzero
467 Time = np.arange(0, xincr * len(Volts), xincr)
468 while '1' in scope.ask("BUSY?"):
469     time.sleep(0.01)
470
471 Corrected_Reflected_Voltage = np.zeros((len(frequency), len(Volts)))

```

```

472 Raw_Reflected_Voltage_Pulsed = np.zeros( (len(frequency), len(Volts)) )
473
474 for i in range(0,len(frequency)):
475     #scope.write("ACQ:STOPA SEQ")
476     #scope.write("ACQ:STATE ON")
477
478     scope.write('CURVE?')
479     data = scope.read_raw()
480     headerlen = 2 + int(data[1])
481     header = data[:headerlen]
482     ADC_wave = data[headerlen:-1]
483
484     ADC_wave = np.array(unpack('>%sB' % len(ADC_wave),ADC_wave))
485
486     Volts = (ADC_wave - yoff) * ymult + yzero
487
488     Raw_Reflected_Voltage_Pulsed[i] = Volts
489     Corrected_Reflected_Voltage[i] = ...
490         Raw_Reflected_Voltage_Pulsed[i]-Ref_Reflected_Voltage_Averaged[i]
491
492 #corrects for vacuum transmission line
493
494
495 while '1' in scope.ask("BUSY?"):
496     time.sleep(0.1)
497     S1.syn_cmd("freqstep")
498
499 S1.syn_cmd("stop")
500 #####
501 #####Data Analysis

```

```

502 ######
503
504 # Eliminate data outliers
505 for j in range(0, len(Time)):
506     for i in range(0, len(frequency)):
507         if i>0 and abs(Raw_Reflected_Voltage_Pulsed[i-1,j]- ...
508             Raw_Reflected_Voltage_Pulsed[i,j]) > 0.01:
509             Corrected_Reflected_Voltage[i,j] = ...
510             Corrected_Reflected_Voltage[i-1,j]
511
512 Time_Resolved_Resonant_Frequency = ...
513     frequency[Corrected_Reflected_Voltage.argmax(axis=0)] #determines ...
514     vacuum resonant frequency using minimum reflected voltage
515
516 Uncorrected_Electron_Density = ...
517     1E10*(np.square(Time_Resolved_Resonant_Frequency/1000) - ...
518         np.square(Vacuum_Resonant_Frequency/1000))/0.81
519
520 # initial parameter guesses
521 # [height, HWHM, center, background]
522
523 # Get the fitting parameters for the best lorentzian
524 Plasma_Resonant_Frequency_Fit = np.zeros(len(Time))
525 plasma_fwhm = np.zeros(len(Time))
526 solution = np.zeros((len(frequency), len(Time)))
527
528 for i in range(0,len(Time)):
529     try:
530         params = np.array([0.12, 1, ...
531             Time_Resolved_Resonant_Frequency[i], 0.0], dtype=np.double) ...
532             #fit guess, hwhm in MHz
533         solp, ier = fit(params, frequency, ...
534             Corrected_Reflected_Voltage[:,i])
535         Plasma_Resonant_Frequency_Fit[i] = solp[2]

```

```

524         plasma_fwhm[i] = 2*abs(solp[1])
525         solution[:,i] = lorentz(frequency, *solp)
526     except:
527         continue
528
529 # calculate the errors
530 r2_pulsed = np.zeros(len(Time))
531 for i in range(0,len(Time)):
532     r2_pulsed[i] = calc_r2(Corrected_Reflected_Voltage[:,i], ...
533                             solution[:,i]) #r_squared for fit
534
535 Uncorrected_Electron_Density_Fit = ...
536     1E10*(np.square(Plasma_Resonant_Frequency_Fit/1000) - ...
537             np.square(Vacuum_Resonant_Frequency/1000))/0.81
538
539 Q_Measured = Plasma_Resonant_Frequency_Fit/plasma_fwhm
540 electron_density_fit_abs_error = ...
541     (1E9/9000*(2/Q_Measured)**0.5*Vacuum_Resonant_Frequency_Fit/1000)**2
542 #cm-3
543
544 Fit_Difference_Plasma_Resonant_Frequency = 100 * ...
545     (Time_Resolved_Resonant_Frequency-Plasma_Resonant_Frequency_Fit) ...
546     /Time_Resolved_Resonant_Frequency
547
548 Uncertainty_in_Density = ...
549     electron_density_fit_abs_error/Uncorrected_Electron_Density_Fit
550
551 #Q_Plasma = (1/((1/Q_Measured) - (1/Q_Vacuum)))
552
553
554 Time_micro = 1E6*Time

```

```

548
549 pylab.subplots()
550 pylab.plot(Time_micro, Uncorrected_Electron_Density, 'ro')
551 pylab.xlabel('Time [ $\mu$ s]')
552 pylab.ylabel('Electron Density [cm $^{-3}$ ]')
553 #xticks(np.linspace(Time_micro[0],max(Time_micro),5))
554 pylab.show()
555
556 spike_freq = max(Plasma_Resonant_Frequency_Fit)
557
558 spike_index = np.where(Plasma_Resonant_Frequency_Fit==spike_freq)
559 spike_index = spike_index[0][0]
560 print("spike frequency = " + str(spike_freq))
561 print("spike error % = " +str(100*Uncertainty_in_Density[spike_index]))
562
563 pylab.subplots()
564 pylab.plot(frequency, Corrected_Reflected_Voltage[:,spike_index], 'bo')
565 pylab.plot(frequency, solution[:,spike_index], 'ro')
566 #pylab.axis([0, 200, 0, 1.3E10])
567 pylab.xlabel('Frequency [MHz]')
568 pylab.ylabel('Reflected Voltage [V]')
569 #xticks(np.linspace(Time_micro[0],max(Time_micro),5))
570 pylab.show()
571
572 pylab.subplots()
573 pylab.plot(frequency, Corrected_Reflected_Voltage[:,20], 'bo')
574 pylab.plot(frequency, solution[:,20], 'ro')
575 #pylab.axis([0, 200, 0, 1.3E10])
576 pylab.xlabel('Frequency [MHz]')
577 pylab.ylabel('Reflected Voltage [V]')
578 #xticks(np.linspace(Time_micro[0],max(Time_micro),5))

```

```

579 pylab.show()
580
581 #Plot Electron Density and R^2 vs Time
582 fig,ax1 = plt.subplots()
583 ax2 = ax1.twinx()
584 ax1.plot(Time_micro, Uncorrected_Electron_Density_Fit, 'go', ...
            markersize=0.1)
585 ax2.plot(Time_micro, Uncertainty_in_Density*100, 'bo', markersize=0.1)
586 ax1.set_xlabel('Time [ $\mu$ s]')
587 ax1.set_ylabel('Electron Density using Fit [cm $^{-3}$ ]', color='g')
588 #ax1.axis([0, max(Time_micro), 0.5E8, 5.5E8])
589 #ax2.axis([0, max(Time_micro), 0, 1])
590 ax2.set_ylabel('% Error', color='b')
591 plt.show()
592
593 #Output the data
594 data_out = np.transpose([Time_micro, Uncorrected_Electron_Density, ...
            Uncorrected_Electron_Density_Fit, ...
            Fit_Difference_Plasma_Resonant_Frequency, Uncertainty_in_Density])
595 np.savetxt(data_title, data_out, delimiter=",")

```